Università degli Studi di Milano Bicocca

Department of Physics "G. Occhialini"
Corso di dottorato in Fisica e Astronomia

Cycle XXXVI

Optimization of negative muon experiments for elemental analysis at the RIKEN-RAL facility

Tutor:
Oliviero Cremonesi

Supervisor:
Massimiliano Clemenza
Adrian D. Hillier

Candidate:
Matteo Cataldo

ACADEMIC YEAR 2022/2023

Contents

List of Figures

List of Tables

Abstract

Muonic Atom X-ray Emission spectroscopy (μ-XES) is a novel technique in the field of Heritage Science. The method uses beams of negative muons to probe materials: the capture process leads to the formation of the so-called "muonic atom". In this bound state, the muon starts to travel down to the ground state of the atom with the emission of fingerprint high-energy X-rays that can be used for elemental identification. Thanks to its remarkable penetration depth, negligible self-absorption of the emitted radiation and sensitivity to all the elements of the periodic table, the technique represents a unique approach to the study of artefacts. At the ISIS Neutron and Muon Source (UK), μ-XES is performed at Port4 of the RIKEN-RAL muon facility. Here, the instrument setup is in continuous development and one of the primary aims of the project was to provide an upgrade to the detection system. Moreover, the project focused on the development of the data analysis of negative muon data. In both cases, the work was based on the use of a Monte Carlo simulation tool called GEANT4/ARBY, developed by the INFN section of Milano Bicocca. Firstly, the ARBY tool was used to model a future instrument concept. With two different scenarios, one for an immediate update and one for a future upgrade, the work focused on the development of an ultimate detector setup. Starting from a well-known detector configuration, the Euroball cluster, a detector array was modelled. The idea was to model a single crystal able to respond to the main necessities of the method: a good resolution in the very low energy part of the spectrum (from 10 to 100 keV) and a good efficiency in the high energy part ($<$ 1 MeV). From simulations, the best approach was represented by a detector array composed of segmented crystals, as reported in Chapter 3. The ARBY tool was not only used for modelling but also for replicating negative muon experiments. The results, reported in Chapter 4, show a tool that is not yet reliable for the generation of X-rays after the muon interaction with matter, due to missing transition in the generated spectra. A solution to this issue could be represented by a Dirac equation solver called MuDirac, developed by the UKRI scientific computing department and the ISIS muon group. The output of the MuDirac software was implemented in ARBY and the preliminary result of the approach showed an improvement of the simulated spectra. Finally, in Chapter 5 the ARBY tool was used for the assessment of thin gold layers in mockups and historic samples. To perform a characterization of the layers, ARBY was used along with the SRIM-TRIM software: by using the information on the number of muons stopped in a given layer, simulations

were compared to the data coming from real experiments. The results of the test on mockup samples, which were previously characterized by other methods, testified to the goodness of the approach. Therefore, the method was finally used for the characterization of the gilding of a piece of the Baptistery gate of Florence, a *formella* representing the Annunciation to Zachary. Differently from mockups, here the thickness of the layers of gold was unknown: by combining the results of the simulation with the experimental data, layers of about 16 μm were assessed for the two standing figures and an uneven layer for the altar, where the size of gold ranged from a few microns up to 50 μm.

Acknowledgements

The PhD was co-founded by the ISIS Neutron and Muon Source (STFC/UKRI) and the University of Milano Bicocca under the studentship agreement No. S2 2021 002 CN8647, via Commission V and Cultural Heritage Net of the National Institute of Nuclear Physics (INFN). The ISIS Neutron and Muon Source, the University of Milano Bicocca and the INFN are gratefully acknowledged for funding and collaborating on the research and development of the Muon spectroscopy techniques at the RIKEN-RAL muon facility. I would like to express my deepest gratitude to the PhD supervisor Dr Massimiliano Clemenza and Dr Adrian D. Hillier for their constant support and patience. My sincere thanks also to Dr Oliviero Cremonesi for his supervision and fundamental help with the GEANT/ARBY software. Furthermore, I'd like to acknowledge Dr. Katsu Ishida, for passing down his knowledge about negative muon science. Lastly, I would like to thank all the people whose contributions helped me with this project: Dr Davide Raspino, Dr Stefano Pozzi, Dr Antonella Scherillo, Dr Francesco Grazzi, Dr Simone Porcinai and Dr Arianna Meoli. Thank you.

Introduction

The use of negative muons for elemental analysis dates back to more than fifty years ago when applications of the mesonic particle for material characterization were first published [1–3]. Even if the method was limited by the technologies of the time, scientists already envisioned the capabilities of the technique and some pioneering experiments on materials were performed, with an early interest in cultural heritage artefacts [4, 5]. However, it is in the last two decades that elemental analysis with negative muons has seen a resurgence, with an increasing number of studies published every year. These included areas such as bio-materials, lithium batteries and solar cells, meteorites and cultural heritage. For the latter especially, the technique has been extensively used, with a renewed interest from the cultural heritage science community, which has always been keen to try new methods, particularly if they can get new and different insights, non-destructively, into the study of an artefact. The interest, is testified by the number of relevant studies published in high-impact journals through the last few years (Figure 1). The technique, indeed, which in this work will be called "Muonic atom X-ray Emission Spectroscopy" (with the acronym: μ-XES) is based on the collection of the radiative emission generated after the interaction of a negative muon with an atom. Conceptually, μ-XES is comparable to a fluorescence technique like XRF (or PIXE and SEM), but with a significant difference from these classical approaches: it can probe both the bulk and the surface of a material. This is due to the remarkable penetration depth of the muon (from tens of microns to the centimetres scale) and the high energies of the emitted X-rays, which can escape the surface with negligible self-absorption, thus providing reliable information from the inside of a sample in a non-destructive way. The method, moreover, is sensitive to all elements of the periodic table: the radiative emission is characteristic of the emitting atom, making elemental analysis feasible (despite this, measurements generally cover from lithium to uranium since the radiation energy emitted from lower elements is too low for being detected with standard detection systems). All these features make μ-XES a very powerful probe for non-destructive material characterization, especially for cultural heritage science, the focus of this thesis. From Roman and Japanese coins to bronze artefacts and organic materials, many different applications have demonstrated the capabilities of the method, as described in the following paragraphs [6].

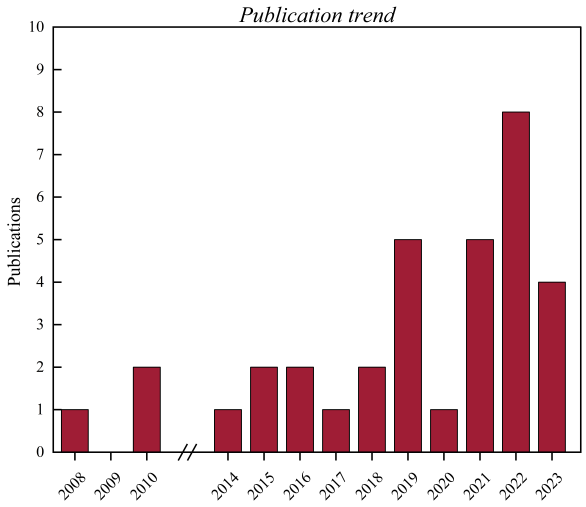

Figure 1: Negative muons for cultural heritage science: number of published works in the last two decades. Data on publications were extracted from Google Scholar.

μ-XES in Heritage Science - Recent highlights

Coinage debasement

Coins are among the best tools for historians to assess the fiscal health of the issuing state and key information can be provided by the evidence of debasement. Debasement is a reduction in the quality of the coin: the surface is enriched in a precious material, such as gold or silver, while the bulk is mainly composed of a less precious material such as copper [7]. In silver coins, this was done by treating the material with an organic acid that stripped the copper out of the alloy and left a silver-enriched surface. Lots of studies have been carried out on this matter, but most of them, when non-destructive, could only probe the surface of the sample. For example, with XRF, only the first few microns of material are probed, giving a result that is not representative of the whole sample. So, to have information from the bulk of coins, μ-XES can be performed. In Hampshire [8] a Julia Domna coin was analysed with a momentum scan: the beam was tuned so that muons could probe at different sites in the sample (as explained in Chapter 2, muon beams can be tuned to increase the penetration depth of the particle). The result from the low momenta spectra (surface or near-surface) shows the absence of copper, which instead is present at higher momentum values, as shown in Figure 2. This was then confirmed by elemental analysis, from which a surface enrichment of about 100 μm was estimated.

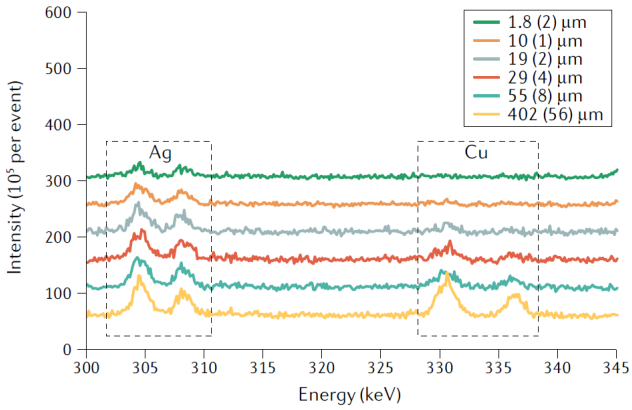

Figure 2: X-ray spectra at different momentum. Silver M_α double peaks are present in all the measurements, whereas copper L_α peaks appear at higher momentum, showing a surface enrichment. The figure was taken and adapted from [9](*reproduced with permission from Springer Nature*).

Similarly, gold coins could be affected by debasement. In Green, [10, 11] the results of an XRF analysis are compared with the one from muonic X-ray emission. From XRF, the three Roman coins showed a high concentration of gold, almost full purity for two out of three. To confirm or deny XRF results, a measurement with muons was carried out. In this case, only two momenta were selected: 40 MeV/c for investigating the core of the coin and 18 MeV/c for the near-surface. Here, as reported in table 1 the results from the muon analysis are in remarkable agreement with that of XRF and no surface enrichment was detected, testifying to the goodness of the technique and approach.

Table 1: Comparison of the XRF and µ-XES analysis. No relevant differences were detected between the two different momentum runs, confirming the absence of debasement. Data was taken and adapted from [10].

	XRF		µ-XES 40 MeV/c		µ-XES 18 MeV/c	
Coin	**Mean Au [wt%]**	**Mean Ag [wt%]**	**Mean Au [wt%]**	**Mean Ag [wt%]**	**Mean Au [wt%]**	**Mean Ag [wt%]**
Tiberius [AD 14-37]	99.73 (0.01)%	0.27 (0.01)%	>99%	<1%	>99%	<1%
Hadrian [AD 134-138]	99.55 (0.01)%	0.45 (0.01)%	>99%	<1%	>99%	<1%
Julian II [AD 361-363]	95.58 (0.03)%	4.15 (0.03)%	>96(1)%	<4(1)%	>96(1)%	<4(1)%

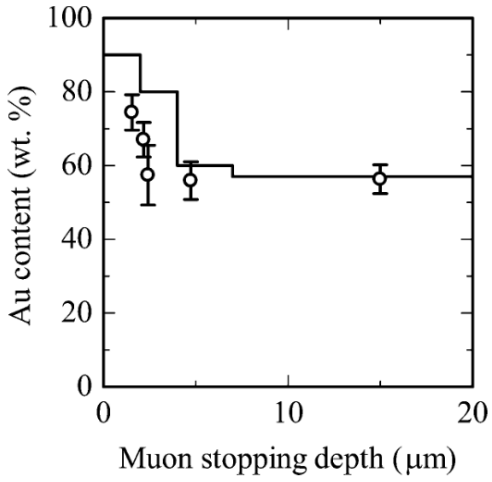

Figure 3: The gold composition against sample thickness demonstrates the surface enrichment. Reprinted with permission from Ref. [12] Copyright (2015) American Chemical Society

Coin debasement was not only mastered by the Romans: in Ninomiya et al. [12], a Japanese Tempo-koban gold coin (19^{th} Century) was analysed with a momentum scan from $\sim$6 MeV/c to $\sim$35 MeV/c. The coin was already known to have a gold enrichment on the surface from other analyses but with a strong composition bias. With a momentum scan, it was possible to determine a change in gold content from the surface to the core, as shown in Figure 3. This was determined by comparing the intensity ratio of Au/Ag. The results of the analysis clearly showed a higher amount of gold around the surface of the coin that then decreased in the core, in agreement with other measurement values (around 57%). As in the previous example, the results are consistent with those of the literature, using other analysis methods.

Copper alloys

Another rich historical archive investigated with muons is represented by copper and bronze artefacts. For this type of material, analyses are mostly devoted to understanding the elemental composition. However, quantitative analysis with negative muons is not yet fully reliable, since there isn't a well-defined procedure and different methods have been used. To now, what is certain is that calibration curves are fundamental tools for providing a trustworthy quantitative analysis. An improvement to the study of elemental composition could be provided by simulation software, as discussed in Chapter 4. A review of the method for quantitative analysis is reported in Biswas [13] along with the analysis of bronze Fibula coming from the Roman city of Augusta Raurica. One option, already pursued in Clemenza [14], where fragments of Nuragic "votive" ships were characterized, is to compare the relative intensity of an X-ray to the one of a reference material, whose composition is plotted in

a calibration curve. Another possibility, as reported in Ninomiya [15], in which a Chinese bronze mirror (Seiun-Kyo) was measured, is to use the ratio of the intensities of peaks, by comparing secondary elements to the principal component of the alloy (copper in this case). As a further validation of the method, it is also important to compare μ-XES results with other techniques. In Ninomiya [15], another example of an application is reported. Two Tempo-Tsuho coins, similar at the eye inspection but different in the making, were analysed. Elemental analysis with negative muons was used to reveal the differences between the real coin and the counterfeit. The result of the analysis clearly showed a different composition of the two coins, as reported in table 2. Here, the results are compared with XRF: even if the two bronze coins seemed to have the same appearance, they have significantly different elemental compositions.

Table 2: Elemental composition of the Tempo-Tsuho coins (expressed in wt%). The real coin is the Tempo-Tsuho (Edo), while the counterfeit is the Tempo-Tsuho (Mito). Data was taken and adapted from [15].

Sample	**Element**	**XRF [wt%]**	**μ-XES [wt%]**
Tempo-Tsuho(Edo)	Cu	77.7 ± 0.1	77.7 ± 1.6
	Sn	14.4 ± 0.5	12.5 ± 1.5
	Pb	7.8 ± 0.2	9.8 ± 1.5
Tempo-Tsuho(Mito)	Cu	73.6 ± 0.1	69.0 ± 1.6
	Sn	12.2 ± 0.4	9.9 ± 1.3
	Pb	14.2 ± 0.1	21.1 ± 2.6

Finally, in [13] the authors measured different copper alloys to produce two calibration curves, reported in Figure 4. The first (a) plots the intensity of the muonic X-rays of different elements versus the atomic percentage of the elements; the second (b) reports the ratio of the intensity of the muonic X-ray versus the ratio of the atomic percentage with respect to copper. To determine the composition of the Fibula, the second method was used. Results define an artefact that was manufactured in two different ways: casted bronze for the ”body” of the fibula (knob, bow and foot, all with a rather high lead content, more than 10 % and forged bronze for the spiral part.

Isotope analysis

Ancient copper alloys are generally characterised by the presence of a secondary element that can be further investigated with muons: lead. This element, indeed, has been widely utilised for provenance studies, since its isotopic composition can be used to retrieve the composition and location of the ore. However, all the classical provenance methods have a destructive approach, even if the required sample is very small [16, 17]. With, μ-XES, instead, lead could be investigated without damaging the sample: it has been observed that, especially for heavier elements, there is an isotopic shift in muonic K transition energies

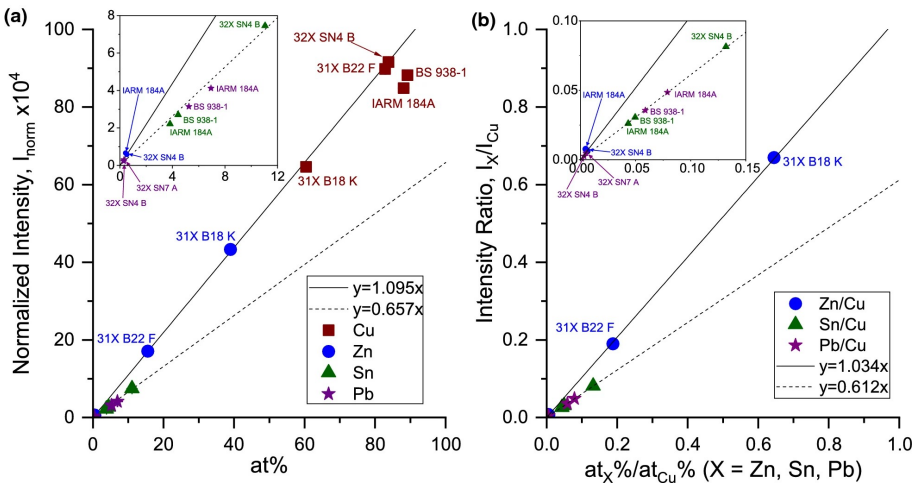

Figure 4: Calibration curve for copper-based alloys obtained by measuring a set of Certified Reference Materials. In (a) the intensity of the muon X-rays is plotted against the atomic percentage of the elements; while in (b), the ratio of the intensity of different elements to the one of copper is plotted against the ratio of the atomic percentage of the secondary elements to the one of copper. In both plots, box insertions show the Sn and Pb points.

[3, 18, 19]. In Ninomiya [20, 21], preliminary measurements were performed on lead and small but measurable shifts were observed in the K_α transitions, as shown in Figure 5.

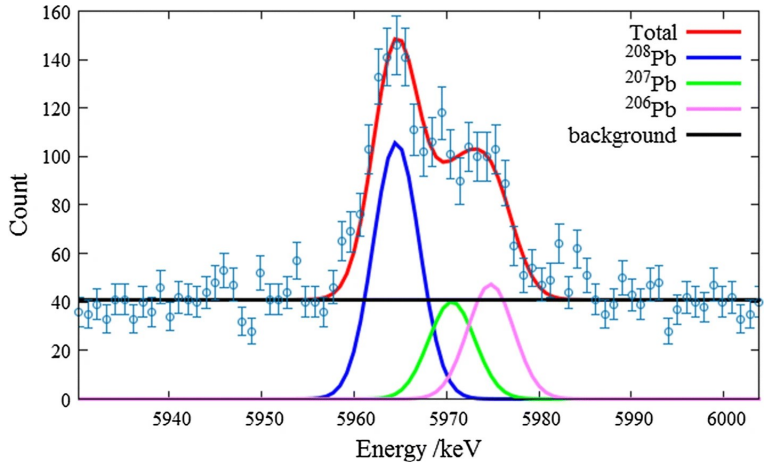

Figure 5: Isotope energy shift in lead K_α emission. Since resolution in the high energy range is very low, the peak had to be deconvoluted. Figure was taken from [20].

However, the energy of this emitted radiation is particularly high, in a region where detection efficiency and resolution are quite poor (E $>$ 5 MeV). Therefore, instead of focusing on the shift of high-energy peaks, another way of assessing the isotope composition is provided by the prompt γ-rays emitted during a negative muon experiment. As described in the

following Chapter, once the muon comes to the 1s level of the atom it could be absorbed by the nucleus. In this excited state, the following rearrangement of the structure of the nuclei may lead to the emission of γ-rays. Depending on the sample, the intensity of the γ-ray will vary, making it possible to determine the isotope content, as reported in a feasibility study by Ninomiya [22]. As shown in Figure 6, in lead, the emission of these γ-rays occur in the 100-400 keV energy range, where the radiation can be easily detected. In this energy range, detectors perform well and the characterization of isotope content is more accessible than using high-energy muonic X-rays. This topic is going to be further investigated by a ChNET project called "MAXI", a collaboration of different INFN sections for the development of isotope identification with μ-XES.

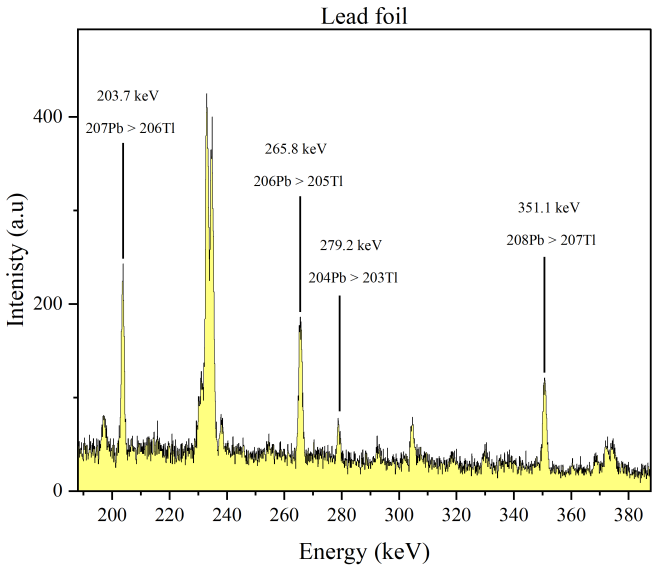

Figure 6: Energy region of the lead spectra where γ-ray emission is detected. The energy of the peaks agrees with the excitation energies of the lead daughter nucleus (thallium) generated after the muon capture by the nucleus. Data were extracted from the IAEA live chart of nuclides.

Organic Materials

Finally, as mentioned before, since the technique is sensible even to low Z elements, the analysis of organic materials is feasible [2, 23, 24]. In Shimada-Takaura [25], the authors analysed some precious glass bottles belonging to the OGATA Koan medicine chests. OGATA Koan (1810–1863) was a physician in the late Edo period and the bottle contained formulated medicines. Due to the preciousness of the material and the impossibility of opening some of the containers, a non-destructive approach was mandatory. Therefore, muonic X-ray analysis was performed on two bottles, with two different momenta: 40 MeV/c and 55 MeV/c. The two selected momenta were stopped in differing parts of the sample; at 40 MeV/c, information came from the container (glass), while at 55 MeV/c, information came

from the material in the container. The results show that the medicine is mainly composed of mercury, chlorine, sodium and oxygen, in agreement with the documents that regulated the properties of drugs (mercury and chlorine are assigned to $HgCl_2$, while sodium and oxygen to NaCl and H_2O, probably added as additives).

Research topics

In this thesis, I will report on the development of the μ-XES technique performed at the ISIS Neutron and Muons Source. After a brief introduction to muon physics in Chapter 1, the experimental technique and the characteristics of the RIKEN facility as ISIS will be described in Chapter 2. Then, the work will focus on the improvement of the detection and DAQ system and the data analysis and interpretation. The common ground in both topics will be the use of Monte Carlo simulation software. In Chapter 3 simulations will be used to characterize and model a new detector setup for the instrument. In Chapter 4, the improvement of the simulation software GEANT4 for the muon interaction process will be discussed, with examples of application and validation. Finally, in Chapter 5, simulation software will be used for the assessment of thin gold layers in mockups and historical objects.

Bibliography

[1] Y Eisenberg and D Kessler. "On the *mu*-Mesonic Atoms". In: *Il Nuovo Cimento* XIX (6 1961).

[2] James J. Reidy et al. "Use of Muonic X Rays for Nondestructive Analysis of Bulk Samples for Low Z Constituents". In: *Analytical Chemistry* 50 (1 1978), pp. 40–44. DOI: 10.1021/ac50023a015.

[3] D Kessler et al. "Munonic x rays in lead isotopes". In: 11 (5 1975).

[4] "Application of muonic X-ray techniques to the elemental analysis of archeological objects". In: *Nuclear Instruments and Methods* 187 (2-3 1981), pp. 563–568. DOI: 10.1016/0029-554X(81)90389-X.

[5] H Daniel. "Application of X-rays from negative muons". In: *Nuclear Instruments and Methods in Physics Research* 3 (1984), pp. 65–70.

[6] Matteo Cataldo et al. "A Novel Non-Destructive Technique for Cultural Heritage: Depth Profiling and Elemental Analysis Underneath the Surface with Negative Muons". In: *Applied Sciences (Switzerland)* 12 (9 May 2022). DOI: 10.3390/app12094237.

[7] A.I. Moreno-Suárez et al. "First attempt to obtain the bulk composition of ancient silver–copper coins by using XRF and GRT". In: *Nuclear Instruments and Methods in Physics Research Section B: Beam Interactions with Materials and Atoms* 358 (2015), pp. 93–97. ISSN: 0168-583X. DOI: https://doi.org/10.1016/j.nimb.2015.05.038.

[8] Bethany Hampshire et al. "Using Negative Muons as a Probe for Depth Profiling Silver Roman Coinage". In: *Heritage* 2 (1 Jan. 2019), pp. 400–407. DOI: 10.3390/heritage2010028.

[9] Adrian D Hillier et al. "Muon spin spectroscopy". In: *Nature Reviews Methods Primers* 2 (1 2022), p. 4. DOI: 10.1038/s43586-021-00089-0.

[10] George Alexander Green et al. "Understanding Roman Gold Coinage Inside Out". In: *Journal of Archaeological Science* 134 (Oct. 2021). DOI: 10.1016/j.jas.2021.105470.

[11] G A Green et al. “Negative muons reveal the economic chaos of Rome’s AD 68/9 Civil Wars”. In: *Archaeological and Anthropological Sciences* 14 (9 2022), p. 165. DOI: 10.1007/s12520-022-01631-1.

[12] Kazuhiko Ninomiya et al. “Nondestructive Elemental Depth-Profiling Analysis by Muonic X-ray Measurement”. In: *Analytical Chemistry* 87 (9 May 2015), pp. 4597–4600. DOI: 10.1021/acs.analchem.5b01169.

[13] Sayani Biswas et al. “The non-destructive investigation of a late antique knob bow fibula (Bügelknopffibel) from Kaiseraugst/CH using Muon Induced X-ray Emission (MIXE)”. In: *Heritage Science* 11 (1 Dec. 2023). DOI: 10.1186/s40494-023-00880-0.

[14] Massimiliano Clemenza et al. “Muonic atom X-ray spectroscopy for non-destructive analysis of archeological samples”. In: *Journal of Radioanalytical and Nuclear Chemistry* 322 (3 2019), pp. 1357–1363. DOI: 10.1007/s10967-019-06927-6.

[15] Kazuhiko Ninomiya et al. “Elemental Analysis of Bronze Artifacts by Muonic X-ray Spectroscopy”. In: Physical Society of Japan, Sept. 2015. DOI: 10.7566/jpscp.8.033005.

[16] J Baker, S Stos, and T Waight. “Lead isotope analysis of archaeological metals by multiple-collector inudctively coupled plasma mass spectrometry”. In: *Archaeometry* 48 (1 2006), pp. 45–56. DOI: https://doi.org/10.1111/j.1475-4754.2006.00242.x.

[17] José A. Cuchí-Oterino et al. “Mineral provenance of Roman lead objects from the Cinca River basin (Huesca, Spain)”. In: *Journal of Archaeological Science: Reports* 37 (2021). DOI: 10.1016/j.jasrep.2021.102979.

[18] H L Anderson et al. “Precise Measurement of the Muonic X Rays in the Lead Isotopes”. In: *Phys. Rev.* 187 (4 Nov. 1969), pp. 1565–1596. DOI: 10.1103/PhysRev.187.1565.

[19] Derrick Kessler et al. “Muonic X rays and capture γ rays in 89Y”. In: *Canadian Journal of Physics* 48 (2011), pp. 3029–3037. DOI: 10.1139/p70-376.

[20] Kazuhiko Ninomiya et al. “Development of non-destructive isotopic analysis methods using muon beams and their application to the analysis of lead”. In: *Journal of Radioanalytical and Nuclear Chemistry* 320 (3 2019), pp. 801–805. DOI: 10.1007/s10967-019-06506-9.

[21] Kazuhiko Ninomiya et al. “Isotope Identification of Lead by Muon Induced X-ray and Gamma-ray Measurements”. In: 011043 (2018), pp. 1–4. DOI: 10.7566/jpscp.21.011043.

[22] Kazuhiko Ninomiya et al. “Isotope Identification of Lead by Muon Induced X-ray and Gamma-ray Measurements”. In: *Proceedings of the 14th International Conference on Muon Spin Rotation, Relaxation and Resonance (μSR2017)*. DOI: 10.7566/JPSCP.21.011043.

[23] Richard L Hutson et al. “Tissue Chemical Analysis with Muonic X Rays”. In: *Radiology* 120 (1 July 1976). doi: 10.1148/120.1.193, pp. 193–198. DOI: 10.1148/120.1.193.

[24] Y Hosoi et al. “Non-destructive elemental analysis of vertebral body trabecular bone using muonic X-rays”. In: *The British Journal of Radiology* 68 (816 Dec. 1995). doi: 10.1259/0007-1285-68-816-1325, pp. 1325–1331. DOI: 10.1259/0007-1285-68-816-1325.

[25] Kayoko Shimada-Takaura et al. “A novel challenge of nondestructive analysis on OGATA Koan’s sealed medicine by muonic X-ray analysis”. In: *Journal of Natural Medicines* 75 (3 2021), pp. 532–539. DOI: 10.1007/s11418-021-01487-0.

Part I

Theoretical background

Chapter 1

The Muon

In this chapter, a description of the main features of muon physics directly related to the aim of this work will be given.

1.1 Properties

Identified by the Greek letter μ, the muon is an elementary particle of the leptons family discovered in 1936 by Carl David Anderson and Seth Neddermeyer [1, 2]. Since its discovery, the muon has been widely studied and its properties are well known: it can be positively or negatively charged, it has a mass of 105.66 MeV/c^2 and a ½ spin (table 1.1).

Table 1.1: Principal Muon properties. Data were taken from NIST database for recommended values of fundamental physical constants [3].

	μ^+	μ^-
Mass (MeV/c^2)	105.6583755 (23)	
Charge	+1	-1
Spin	1/2	
Muon-electron mass ratio	206.79	
Lifetime (ns)	2197.03 ± 0.04	< 2197.03
Location	Interstitial or chemically bonded	captured by atom

In nature, muons are produced by the interaction of primary cosmic rays with the particles present in the upper atmosphere. Here, showers of highly energetic protons collide with light nuclei to produce charged pions via the following reactions:

$$\begin{aligned} p^+ + p^+ &\rightarrow p^+ + n^+ + \pi^+ \\ p^+ + n &\rightarrow p^+ + p^+ + \pi^- \end{aligned} \tag{1.1}$$

$$\begin{aligned} p^+ + p^+ &\rightarrow p^+ + p^+ + \pi^- + \pi^+ \\ p^+ + n &\rightarrow p^+ + n + \pi^- + \pi^+ \end{aligned} \tag{1.2}$$

Where single pion production has a proton energy threshold > 280 MeV (1.1), while for double pion production, this edge increases to proton energies > 600 MeV (1.2) [4, 5]. Pions are unstable particles and decay after a mean lifetime of 26 *ns* into muons:

$$\pi^+ \rightarrow \mu^+ + \nu_\mu \tag{1.3}$$

$$\pi^- \rightarrow \mu^- + \overline{\nu}_\mu \tag{1.4}$$

The produced muons are quite energetic, with a mean energy at sea level of about 4 GeV and a typical flux of 1 muon/cm^2/min [6]. The muon is an unstable particle and decays with the emission of a positron or an electron and two neutrinos:

$$\mu^+ \rightarrow e^+ + \overline{\nu}_e + \nu_\mu \tag{1.5}$$

$$\mu^- \rightarrow e^- + \nu_e + \overline{\nu}_\mu \tag{1.6}$$

For the positive muon, the average lifetime is 2197.03 ± 0.04 ns, the longest among unstable elementary particles [7]. For the negative muon, instead, the average lifetime is influenced by capture: given their negative charge, muons interact with the material in which are stopped. The interaction process occurs in a very short time (femtosecond scale) and depending on the capturing specimen, this will reduce the lifetime from that of the positive muon [8]. This parameter has been measured for different materials and is reported in Figure 1.1.

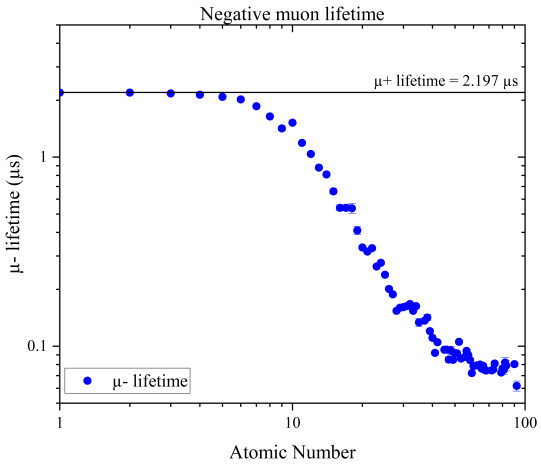

Figure 1.1: Variation of negative muon lifetime with the atomic number Z. Data were taken and adapted from [8].

1.2 Interaction with matter

Muon-based techniques are implantation methods. Implantation means that muons penetrate into samples and then come to rest somewhere inside the material. That is the basis of the entire muon spectroscopy field: muons are used as a local probe for getting information from where they are stopped in materials [4, 9]. Depending on the charge, they interact differently and they are used for different purposes: positive muons, which behave like a light proton, are mostly used in material science for muon spin rotation, relaxation and resonance techniques (μSR); while negative muons, often referred as "heavy electrons" are used to study the chemical aspect of materials. When implanted, the positive muons can form three different states:

- Mu^+: a state in which the muon exits on its own as μ^+
- Mu^0: the muon will be linked to a free electron to form a hydrogen-like system called "Muonium"(Mu)
- Mu^-: eventually, the muon can pick up 2 electrons to form H^- like system

The negative muon, instead, when implanted in matter will undergo capture to form a muonic atom, which will be described extensively in the following paragraph. If the capturing specimen is hydrogen, "Muonic hydrogen" is formed, a proton-muon system that is widely used to address the proton radius puzzle (this has been added for completeness and will not be discussed any further) [10–13].

1.3 Muonic atoms

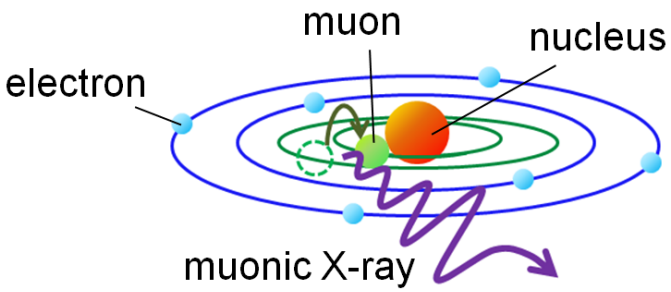

Figure 1.2: Capture of a negative muon by an atom: the movement of the muon along the muonic orbitals generates the emission of muonic X-rays.

A muonic atom is a bound state of a muon and a nucleus along with bound electrons (Figure 1.2). This state is formed when the muon is slowed down by the interaction with the

outer atomic electrons of the atom until it is captured by the Coulomb field of the nucleus. Due to the mass of the muon, it will orbit 207 times closer to the nucleus, thus experiencing 207 times higher binding energies. Capture occurs in orbitals with a high principal quantum number, above n = 20: from here, the muon starts to cascade down towards the nucleus. The first dominant process of the cascade is muon-induced Auger decay: the energy is transferred to bound electrons, which are expelled from the atom. When the muon gets closer to the nucleus, around $n \approx 6$, radiative decay becomes dominant, with the emission of high-energy muonic X-rays (Figure 1.3). The entire cascade process is very fast, typically in the femtosecond scale [14]. In addition, prompt electronic X-rays can be detected during a cascade: during the process, electronic holes can be refilled by outer electrons, leading to the emission of characteristic electronic X-rays (moreover, if the muon does not entirely screen the nuclear charge, electronic X-rays with energy closer to the Z-1 species can be emitted [14]). Finally, the deexcitation terminates at *1s* level, where the muon can either decay or be captured by the nuclei. Capture, except for light nuclei (lower than magnesium) is more likely to occur via the following reaction:

$$\mu^- + p \rightarrow n + v \tag{1.7}$$

Hence, the muon is captured by a proton to form a neutron and a neutrino to form a Z-1 system. If the proton is not strongly bounded, the neutron will be emitted with an energy of 5.2 MeV (the remaining energy goes to the neutrino); otherwise, if the proton is strongly bonded, the daughter nucleus, Z-1, will be in a highly excited state, from which it will return to the ground state via the emission of neutrons and γ-rays. At the end of this process, delayed electronic X-rays belonging to the Z-1 system can be emitted and recorded into a spectrum.

1.3.1 Cascade calculations

The muonic transition energies have been measured experimentally for multiple elements and reported in the literature and in open source databases [15, 16]. Furthermore, energy levels can be calculated using a point nucleus approximation via the following equation:

$$E_n, j = -\frac{m_\mu c^2}{1 + m_\mu / M} \cdot \frac{(Z\alpha)^2}{2n^2} \cdot \left[1 + \left(\frac{Z\alpha}{n}\right)^2 \cdot \left(\frac{n}{j + 1/2} - \frac{3}{4}\right)\right] \tag{1.8}$$

where n is the principal quantum number, j is the quantum number for the total angular momentum, m_μ is the muon mass, M the mass of the nucleus, Z the atomic number and α is the fine structure constant [4]. The equation shows that the energy of the transition is proportional to the muon mass, so the emitted X-ray will be around 207 times more than the energy of an electronic X-ray, even for low Z atoms (from 0.01 MeV to 8 MeV). Another effective way to calculate muon energy levels can be provided by the solution of the radial Dirac equation, which leads to the quantized energy eigenvalue equation:

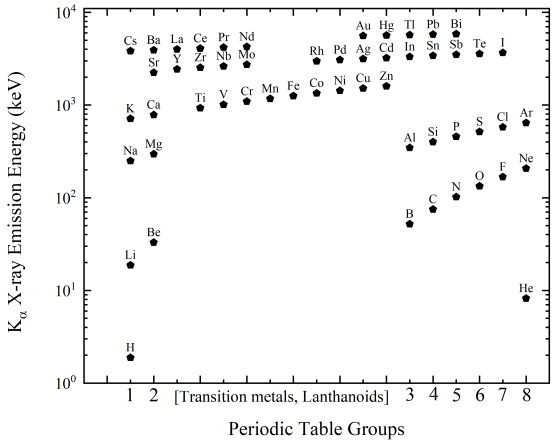

Figure 1.3: Kα transition energies for atoms from hydrogen to bismuth. Data were taken and adapted from [15].

$$E_n, j = m/\sqrt{1+\frac{Z\alpha}{n-|k|+\sqrt{k^2-Z^2\alpha^2}}} \tag{1.9}$$

where m is the mass of the muon, α is the fine structure constant and k is a quantum number specific to each eigenstate (positive or negative integer). This equation is solved by a Dirac equation solver called MuDirac, developed by the ISIS computational team [17]. A more detailed description of the software will be given in Chapter 4.

1.4 Atomic Capture probability

The first estimation of muon capture rate by atoms was given by Fermi and Teller: their model estimated that the probability of a muon being captured was proportional to the total number of electrons in an atom, so dependent on atomic number Z [18]. For example, for a material with two elements like an oxide, the capture rate was defined by:

$$A\left(\frac{Z}{O}\right) = \frac{nN_\mu(Z)}{mN_\mu(O)} \tag{1.10}$$

where $N_\mu(Z)$ is the proportion of muons captured by the metal. Capture rate as a function of Z, however, was found to have some inconsistencies by later studies. As shown in Figure 1.4, compared to other methods developed, the Fermi-Teller model provided a description that didn't take into account the effects of the atomic structure. A development was introduced by von Egidy and Scheuwly that assumed that the capture probability was

proportional to the number of loose-bound electrons [19, 20]. They introduced a correction factor :

$$\alpha = \left(1 - \frac{E_b}{E_0}\right)^2 \tag{1.11}$$

where E_b is an electron binding energy and E_0 is a cutoff of about 80 eV. This factor has been added to a more complete equation that takes into account also valence electrons, that works well for oxides, chlorides and fluorides:

$$A\left(\frac{Z_1}{Z_2}\right) = 0.6\rho(1+\alpha\rho)\left(\frac{Z_1}{Z_2}\right)^{\frac{1}{8}}(1+5.53V^{5.45}\cdot 10^{-5}) \tag{1.12}$$

where ρ is the density and V the valency. α depends on materials and for oxides, when Z_1=<18, α = -0.164 otherwise is 0. For chlorides, when Z_1=<18, α = -0.222 [21].

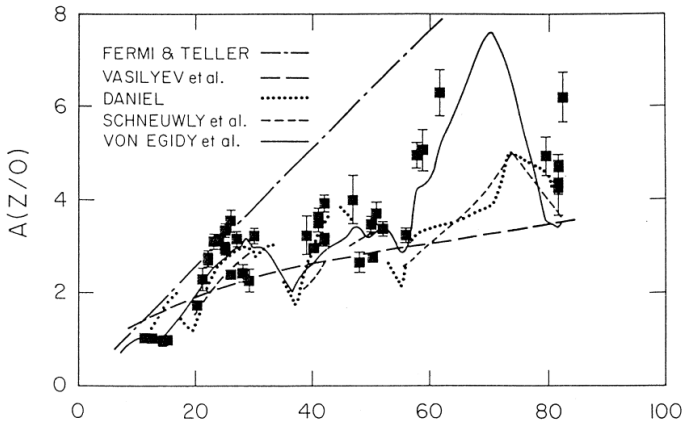

Figure 1.4: The different models developed to describe the capture rate in oxides are here compared to the experimental data. The models of Schneuwly and von Egidy are the ones with the best fit [7]. Experimentally, the capture ratio in oxides consists in detecting the K_α emission of the element in which the muon is captured and the one of oxygen and comparing them, as described in [22].

1.5 Stopping muons in matter

For heavy charged particles like muons, the mean stopping power can be described by the following equation:

$$-\frac{dE}{dx} = a(E) + b(E)E \tag{1.13}$$

where E is the total energy and *a(E)* is the electronic stopping power and *b(E)* is the energy loss due to radiative processes like bremsstrahlung, pair production and photonuclear

interactions [23]. For low-momentum muons ($E < 100$ GeV/c), the energy loss is mainly due to ionization and excitation of atoms, resulting in a remarkable penetration depth (yet, material density plays an important role), while at higher momentum radiative loss becomes dominant, as shown in Figure 1.5. A more comprehensive description of the behaviour of the stopping power is expressed by the Bethe-Bloch equation for muons:

$$-\frac{dE}{dx} = \frac{4\pi}{m_e c^2} \cdot \frac{nz^2}{\beta^2} \cdot (\frac{e^2}{4\pi\varepsilon_0})^2 \cdot \left[ln(\frac{2m_e c^2 \beta^2}{I(1-\beta^2)}) - \beta^2 \right] \tag{1.14}$$

The formula describes the energy loss dE along a dx path of a charged particle of speed v into a target of electron density n and mean excitation potential I (c is the speed of light and ε_0 the vacuum permitivity, $\beta = v/c$ and m_e the electron charge and rest mass). dE/dx is defined as the mass stopping power and values for materials can be found in literature [24]. Besides mathematical formulas, the stopping range in matter is also provided by simulation software like SRIM-TRIM [25]. It follows that if the momentum is increased, the muon will be able to travel more into a material before being stopped. So, depending on the material density and the momentum, the technique can probe at different depths, thus becoming depth-selective. This is an invaluable tool, especially when working with materials that have an external crust or sample with gildings and external layers. Here, density plays an important role: in metals, the penetration depth can reach up to about 10 mm (copper, silver, iron) while in less dense materials like carbon or water, it can extend to tens of millimetres ($\sim$ 30 mm in carbon and $\sim$ 60 mm in water - in both examples, momentum depends on the experimental setup and the type of sample) [26, 27].

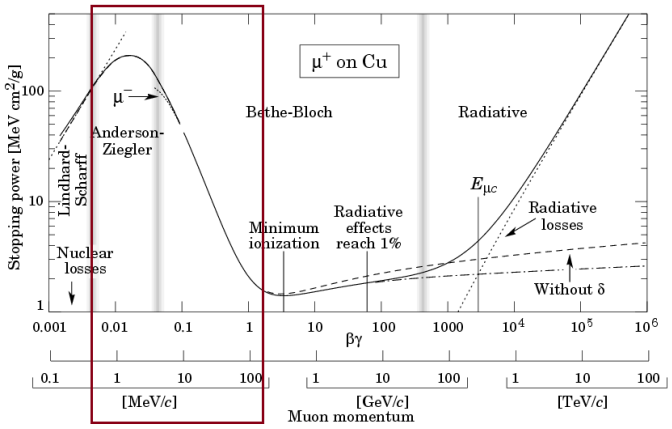

Figure 1.5: Mass stopping power in copper as a function of energy. Highlighted by the box is the range of momentum used in negative muon analysis. The figure was taken and adapted from [24].

Bibliography

[1] Carl D. Anderson and Seth H. Neddermeyer. “Cloud Chamber Observations of Cosmic Rays at 4300 Meters Elevation and Near Sea-Level”. In: *Phys. Rev.* 50 (4 1936), pp. 263–271. DOI: 10.1103/PhysRev.50.263.

[2] S. H. Neddermeyer and C. D. Anderson. “Note on the Nature of Cosmic Ray Particles”. In: *Phys. Rev.* 51 (1937), pp. 884–886. DOI: 10.1103/PhysRev.51.884.

[3] Eite Tiesinga et al. “CODATA recommended values of the fundamental physical constants: 2018”. In: *Rev. Mod. Phys.* 93 (2 2021), p. 025010. DOI: 10.1103/RevModPhys.93.025010.

[4] S. Blundell et al. *Muon Spectroscopy: an introduction*. Oxford, UK: Oxford University Press, 201.

[5] S.M. Vogiatzi A. Knecht A. Skawran. “Study of nuclear properties with muonic atoms”. In: *The European Physical Journal Plus* 135.777 (2020). DOI: 10.1140/epjp/s13360-020-00777-y.

[6] J.L. Autran et al. “Characterization of atmospheric muons at sea level using a cosmic ray telescope”. In: *Nuclear Instruments and Methods in Physics Research Section A: Accelerators, Spectrometers, Detectors and Associated Equipment* 903 (2018), pp. 77–84. DOI: https://doi.org/10.1016/j.nima.2018.06.038.

[7] D.F. Measday. “The nuclear physics of muon capture”. In: *Physics Reports* 354.4 (2001), pp. 243–409. DOI: https://doi.org/10.1016/S0370-1573(01)00012-6.

[8] T. Suzuki, D.F. Measday, and J.P Roalsvig. “Total nuclear capture rates for negative muons”. In: *Physical review C* 35.6 (1987), pp. 2212–2224.

[9] A. D. Hillier, K. Ishida, and B. Hampshire. *Depth-Dependent Bulk Elemental Analysis Using Negative Muons*. Ed. by Valentina D’Amico Sebastiano and Venuti. 2022. DOI: 10.1007/978-3-030-60016-7_3.

[10] Randolf Pohl et al. “Muonic Hydrogen and the Proton Radius Puzzle”. In: *Annual Review of Nuclear and Particle Science* 63.1 (2013), pp. 175–204. DOI: 10.1146/annurev-nucl-102212-170627.

[11] Jean-Philippe Karr and Dominique Marchand. "Progress on the proton-radius puzzle". In: (). DOI: 10.1101/162784.

[12] Clara Peset, Antonio Pineda, and Oleksandr Tomalak. "The proton radius (puzzle?) and its relatives". In: *Progress in Particle and Nuclear Physics* 121 (2021), p. 103901. DOI: https://doi.org/10.1016/j.ppnp.2021.103901.

[13] Carl E. Carlson. "The proton radius puzzle". In: *Progress in Particle and Nuclear Physics* 82 (2015), pp. 59–77. DOI: https://doi.org/10.1016/j.ppnp.2015.01.002.

[14] T. Okumura et al. "Deexcitation Dynamics of Muonic Atoms Revealed by High-Precision Spectroscopy of Electronic *K* X Rays". In: *Phys. Rev. Lett.* 127 (5 2021), p. 053001. DOI: 10.1103/PhysRevLett.127.053001.

[15] R. Engfer et al. "Charge-distribution parameters, isotope shifts, isomer shifts, and magnetic hyperfine constanst from muonic atoms". In: *Atomic Data and Nuclear Data Tables* 14 (1974), pp. 509–597.

[16] D. R. Zinatulina. "Electronic Catalogue of Mesoroentgen Spectra". In: *Physics of Atomic Nuclei* 82 (3 2019). DOI: 10.1134/S1063778819030165.

[17] Simone Sturniolo and Adrian Hillier. "Mudirac: A Dirac equation solver for elemental analysis with muonic X-rays". In: *X-Ray Spectrometry* (June 2020), pp. 1–17. ISSN: 10974539. DOI: 10.1002/xrs.3212.

[18] E. Fermi and E. Teller. "The Capture of Negative Mesotrons in Matter". In: *Phys. Rev.* 72 (5 1947), pp. 399–408. DOI: 10.1103/PhysRev.72.399.

[19] T. von Egidy, D. H. Jakubassa-Amundsen, and F. J. Hartmann. "Calculation of muonic Coulomb-capture probabilities from electron binding energies". In: *Phys. Rev. A* 29 (2 1984), pp. 455–461. DOI: 10.1103/PhysRevA.29.455.

[20] H. Schneuwly, V.I. Pokrovsky, and L.I. Ponomarev. "On coulomb capture ratios of negative mesons in chemical compounds". In: *Nuclear Physics A* 312.3 (1978), pp. 419–426. DOI: https://doi.org/10.1016/0375-9474(78)90601-2.

[21] S. Stanislaus, F. Entezami, and D.F. Measday. "Atomic capture of muons and density". In: *Nuclear Physics A* 475.4 (1987), pp. 642–656. DOI: https://doi.org/10.1016/0375-9474(87)90230-2.

[22] H. Daniel. "Coulomb capture of muons and atomic radius". In: *Zeitschrift für Physik A Atoms and Nuclei* 291 (1979). DOI: 10.1007/BF01415811.

[23] S.I Striganov D.E Groom N.V. Mokhov. "Muon stopping power and range tables 10MeV-100TeV". In: *Atomic Data and Nuclear Tables* 76.2 (2001).

[24] M. Tanabashi et al. "Passage of particle through matter". In: *Phys. Rev. D* 98 (3 2018), p. 030001. DOI: 10.1103/PhysRevD.98.030001.

[25] James F. Ziegler, M. D. Ziegler, and J. P. Biersack. "SRIM – The stopping and range of ions in matter (2010)". In: *Nuclear Instruments and Methods in Physics Research Section B: Beam Interactions with Materials and Atoms* 268 (11-12 June 2010), pp. 1818–1823. DOI: 10.1016/J.NIMB.2010.02.091.

[26] A. D. Hillier, D. M. Paul, and K. Ishida. "Probing beneath the surface without a scratch - Bulk non-destructive elemental analysis using negative muons". In: *Microchemical Journal* 125 (2016), pp. 203–207. DOI: 10.1016/j.microc.2015.11.031.

[27] M. K. Kubo et al. "Non-destructive elemental depth-profiling with muonic X-rays". In: *Journal of Radioanalytical and Nuclear Chemistry* 278 (3 2008), pp. 777–781. DOI: 10.1007/s10967-008-1610-x.

Chapter 2

Experimental technique

In this chapter, the production of muons in large-scale facilities will be discussed, with a focus on the RIKEN-RAL muon facility at the ISIS Neutron and Muon source.

2.1 Muon facilities

The reaction taking place in the upper atmosphere (Eq. 1.1, 1.2) is reproduced in all the five muon facilities that are currently operating around the world: ISIS, J-PARC, PSI, TRIUMF and MuSIC (with more planned in the US, China and South Korea) [1–5]. Here, high-energy proton beams interact with targets generally made of a low Z material (like graphite) to generate pions. These facilities are classified by the acceleration process used to produce muons: they are quasi-continuous and pulsed muon sources. Quasi-continuous beams are produced by cyclotrons (operated at tens of MHz) in facilities like PSI, TRIUMF and MuSIC, where the time between pulses is comparable to the pion lifetime and the time structure of the beam is smoothed to a quasi-continuous beam [6]. In pulsed facilities, like ISIS and J-PARC, protons are accelerated to the graphite target by synchrotrons (operated at 50 or 25 Hz). Here, the pulse gap is higher so that the muons are delivered in bunches. The main characteristics of both sources are reported in table 2.1. Both configurations can then deliver muons to the instruments with two types of beamlines: surface and decay. Surface beamlines transport the muons produced close to the surface of the target. These types of beamlines typically work with positive muons, at a maximum momentum and flux of 29 MeV/c. Decay beamlines, instead, collect and transport pions through superconducting solenoids, in which they decay to produce muons, that are delivered to the instruments.

Table 2.1: Continuous vs pulsed sources

	Continuous	**Pulsed**
Accelerator type	Cyclotron	Synchroton
Count system	Muon trigger	Accelerator trigger
Rate limit	Single muon in sample	Detector dead time
Time resolution	Detectors-electronics ($\geq 80ps$)	Muon pulse width ($\approx 55ns$)
Background	Undetected second muon/ cosmic rays	Negligible

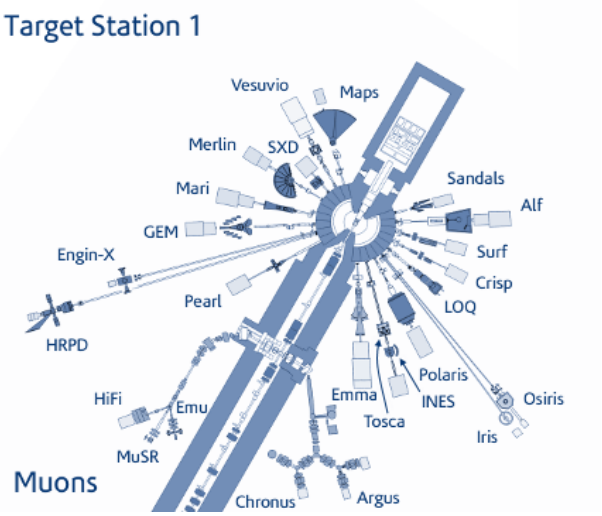

Figure 2.1: ISIS target station 1: A total of seven experimental areas are dedicated to muon science.

2.2 Muons at ISIS

The ISIS pulsed neutron and muon source is an 800 MeV, 220 μA and 50 Hz spallation facility located in Rutherford Appleton Laboratory, Oxfordshire [7, 8]. At ISIS, protons are accelerated to 84% of the speed of light and delivered to two target stations, where more than 30 instruments perform neutron and muon experiments. The muon target is located along the beam path before the neutron target in TS1. It is a 10 mm thick graphite target (along the path of the proton beam), set at 45° and cooled by a water circuit, taking approximately 5% of the proton beam. Muons are delivered to two beamlines: the European Commission Muon (EC - surface beamline) and the RIKEN-RAL facilities (decay beamline) (Figure 2.1). The latter has been used for th experiments reported in this work and will be described in detail il the next paragraph. For a more detailed description of the EC beamline, see Ref. [9].

2.2.1 The RIKEN-RAL Facility

Born from an international collaboration between the Japan research institute RIKEN and the Rutherford Appleton Laboratory, the RIKEN-RAL facility was established in 1990 to promote muon science [1, 10]. The facility was designed to provide a high-intensity negative and positive muon beam and the first muon beam was delivered in 1994. The muon momentum can be tuned from 15 MeV/c to 120 MeV/c, and it is possible to deliver both positive and negative muons to the four experimental ports (Fig. 2.2):

- Port1: now devoted to the FAMU experiment, was originally developed for muon-catalyzed fusion [11, 12];
- Port2: for condensed matter studies with the ARGUS μSR spectrometer [13];
- Port3: a development beamline;
- Port4: beamline that host both the elemental analysis setup and the CHRONUS spectrometer [14, 15].

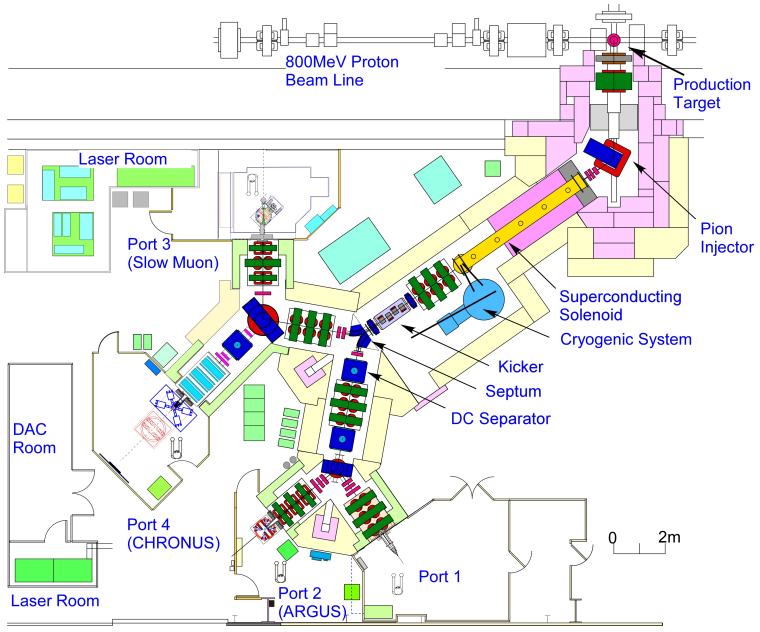

Figure 2.2: Decay beamline at the RIKEN-RAL Facility at ISIS. The beam is focused and bent by quadrupoles (green) and dipoles (blue) and delivered to multiple instruments. Elemental analysis experiments are performed in Port4.

Pion transportation

Due to the characteristic structure of the ISIS proton beam, which produces a double-pulsed beam with a 55 ns width and a 320 ns separation, the facility is able to provide single and doubled pulsed beams to each experimental port, thus enabling independent experiments. The transportation of the beam to the experimental ports starts with the pion injection system, as shown in Figure 2.2. This system is able to accept up to 220 MeV/c pions and consists of two radiation-hard quadrupoles (green), placed close to the target to increase the solid angle acceptance, a dipole magnet to bend the pion beam and vacuum equipment. The dipole magnet has a bending angle of 55° and delivers pion to the decay section. To prevent direct radiation from coming off the production target, the pion injection system is heavily shielded by a total of 250 tons of iron block and concrete [10]. In the decay section, a superconducting solenoid magnet, pions decay in flight into muons. The solenoid is a 5.5 m magnet formed by eleven coils of 50 cm each and has a magnetic field that ranges from 0 to 5 T. Then the beam is delivered to the muon extraction system, from which the decay muon beam is delivered to the experimental ports.

Figure 2.3: For the recent refurbishment, the concrete shielding was removed, showing all the components of the facility. In yellow, on the left, the end of the superconducting solenoid. Quadrupole magnets, in green, are used to focus the beam, while bending magnets, in blue, to bend.

Muon extraction

The extraction system consists of a triplet of quadrupole magnets followed by a kicker magnet. As mentioned the proton beam structure is double-pulsed: for experiments that require a beam momentum of less than 65 MeV/c, the double bunch can be separated by the kicker and the septum magnet to a single pulsed beam. When separation is required, the

kicker magnet generates a magnetic field that is longer than the pulse width but shorter than the 320 ns gap between each pulse to deflect the first or the second muon pulse. The kicked beam, deflected by another 7°, is then delivered to the septum magnet, which can act either as a bending or a septum magnet. In the first case, for momentum higher than 65 MeV/c, it will deflect the double-pulsed beam to a single experimental port. In the second case, it will produce an opposite magnetic field to deflect the two single pulses by 41° and deliver it to two different experimental ports.

Momentum selection

For experiments that require a well-defined momentum scan, the momentum selection is performed by tuning the magnetic field of the bending magnets, as stated by the following relation:

$$p = 0.2998Br \tag{2.1}$$

where B is the magnetic field and r the bending radius of the beam, defined by its geometry [16]. It follows that by changing the magnetic field it is possible to select the particle flying with a well-defined momentum. At ISIS, in addition to the tuning of the bending magnets, also the solenoid coil current is changed. This is done to focus even more the beam and to increase the efficiency of the pion-to-muon decay. Since the process of momentum selection could be contaminated by other particles travelling within the beam, like positrons or electrons, DC separators (or Wien filters) are placed just after bending magnets (not used for elemental analysis). This entire system provides an intense muon beam to be delivered to each port, as shown in Figure 2.4, where intensity is plotted as a function of the beam momentum. Nominally, the typical negative muon beam intensity at 60 MeV/c is 7 x 10^4/s [10].

2.2.2 Port4: setup for negative muon experiments

As mentioned, the Port4 setup can be adjusted both for μSR experiments and elemental analysis. By removing the CHRONUS spectrometer, it is possible to mount a table that can host the μ-XES setup, as shown in Figure 2.5. The current setup for the technique consists of 4 High-Purity Germanium detectors that cover an energy range that goes from a few keV up to 8 MeV and have a solid angle coverage of 0.37 sr (3% of 4π). Table 2.2 reports the main detector characteristic.

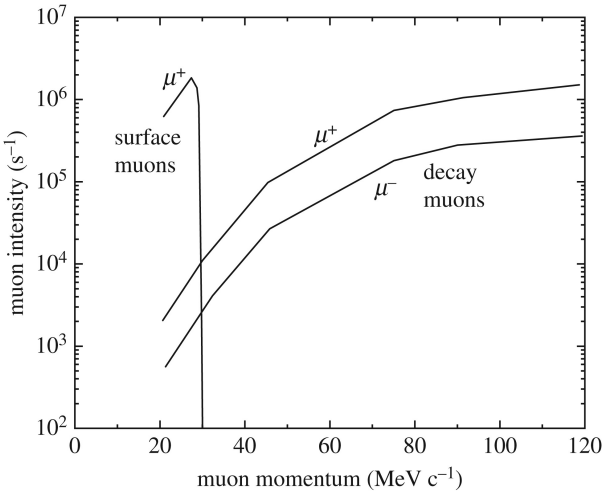

Figure 2.4: Muon beam intensity as a function of momentum. The production rate for high-energy decay muons is generally lower than surface-energy muons. In addition, as the proton beam interacts mostly with positively charged particles, positive muon production is favoured. The figure was taken and adapted from [10].

Table 2.2: Detectors characteristic (from ORTEC datasheets)

	GE1	**GE2**	**GE3**	**GE4**
Model	GMX20P4	GEM20P4-70-PL	GEM-S5020P4-B	GEM-S5020P4-B
Doping	n-type	p-type	p-type	p-type
Energy Range (MeV)	0.05 - 8	0.05 - 8	0.02 - 1	0.02 - 1
Crystal size (mm)	54.8x49.8	56.7x39.7	49.6x22.8	49.5x22.3
Endcap window	Be	Al	Be	Be

Setting up this default configuration requires at least two days, including the cooling of the detectors with liquid nitrogen. Cooling is done beforehand, following a well-defined procedure that minimizes the risk of damaging detectors. Before filling with liquid nitrogen, the dewars are flushed with N_2 gas to eliminate any air or moist residual that could freeze when LN_2 is pumped. Before an experiment, filling is done at least two days before the start of the measurement to allow the crystal to cool down properly. Due to the size of the dewars, detectors have to be refilled every 24 hours. The second step involves mounting the metal frame that supports the detector's table. Finally, the detectors are put in place and aligned thanks to markings on the table at a working position which is generally around 15 cm from the sample position, placed in the centre of the table (distance that can be modified depending on the investigated material). The two detectors with better resolution and efficiency are placed upstream (beside the beam exit), the other two downstream. Each detector has a high-voltage and bias shutdown cable, two output cables and the preamplifier

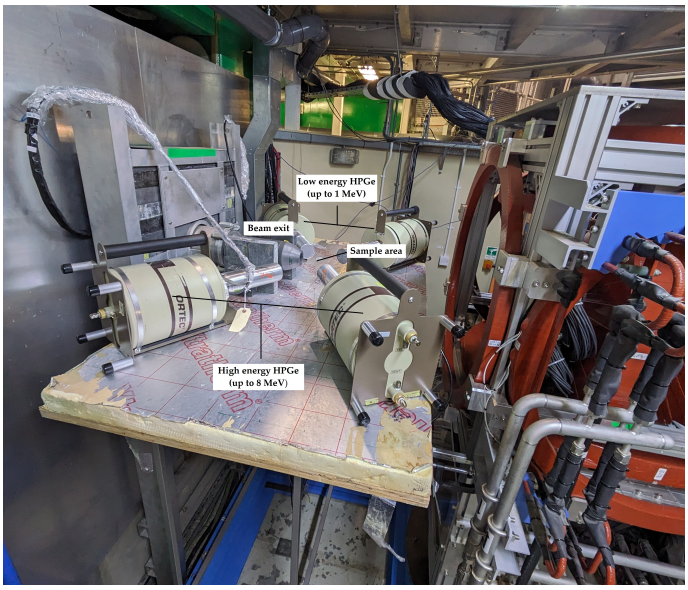

Figure 2.5: Port4: the CHRONUS spectrometer can be moved backwards to leave a space in front of the beam exit, where the elemental analysis setup is mounted.

cable. The firsts are connected to an ORTEC bias supplier which provides high voltage and bias shutdown to prevent damage to the crystals. The preamplifier power supply is directly provided by the amplifier, placed in the DAQ system just above Port4. The acquisition system is divided into two areas, with the ADC placed in the RIKEN control room. The detector signals, in detail, are delivered to a four-channel signal divider, from which the pre-amplified signal is delivered to an energy amplifier (shaping time for each detector is set to 4 and 8 µs). Then, the amplified signal is delivered to the ADC crate. From that, the acquired signal is converted into a spectrum by a dedicated machine. At RIKEN, the signal is triggered with the proton beam pulse thanks to a Cherenkov counter connected to ADC. The final step of the setup is the calibration of the detectors, to convert the spectrum x-axis from channel to energy units. Calibration is performed by acquiring a spectrum with some radionuclides with known energies that cover the low and high energy range of the spectrum. Given that the relationship between the energy of an incident γ or X-ray and the ADC channel number is approximately linear with a two-point calibration it is possible to convert the spectrum x-axis to energy units. From the spectrum, the channel number and the associated energy are used to calculate the slope and the intercept of the linear relationship. Finally, the parameter is fed into the software on the acquisition machine which performs the calibration. The final result, as shown in Figure 2.6, is an energy-calibrated X-ray spectrum for each detector. Figure 2.6, in particular, reports the spectra of a silver standard. Here it is possible to see how the detectors characteristics influence the collection of the data. Figure 2.6a,b show the spectra of the two high energy detectors, which cover up to 8 MeV. Dimensions of the two crystals are roughly the same, but the achievable resolution is

different, especially at high energies: in the upstream detector (a), the Ag fingerprint double peaks are well resolved (from literature, 3141-3148 keV and 3178-3185 keV), whereas, in the downstream one, the resolution is not enough to distinguish the peaks. Moreover, the difference in the endcap material influences the detection of the low-energy peaks (< 100 keV), which in the downstream detectors can be attenuated by the aluminium endcap. The two low-energy detectors (Figure 2.6c,d), instead, have the same characteristics and provide very similar X-ray spectra, with small discrepancies that can be adjusted by tuning the DAQ parameters.

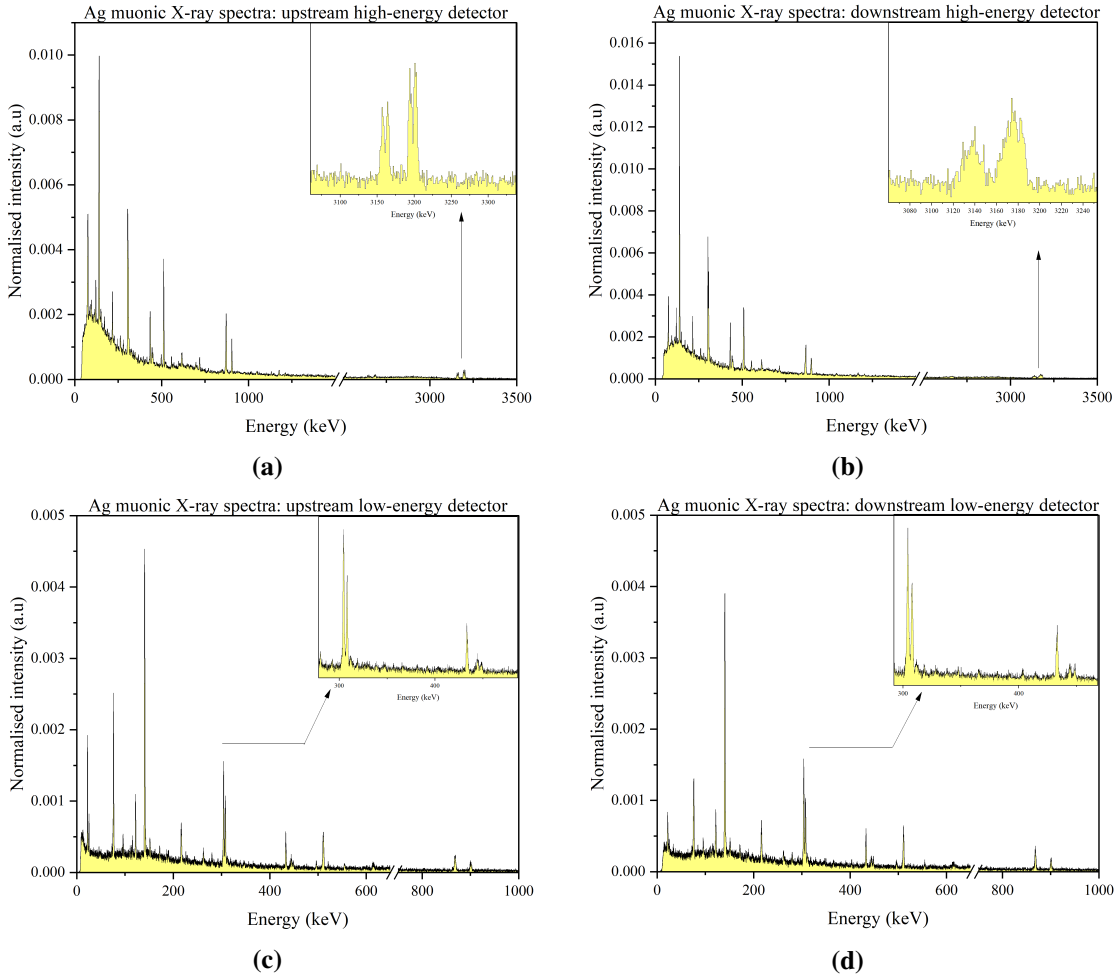

Figure 2.6: Muonic X-ray spectra of an Ag standard sample. Highlighted in (a) and (b) is the difference in resolution of the two high-energy detectors: the Ag K_α and K_β double peaks are not resolved in the downstream detector (peak positions 3141-3148 keV and 3178-3185 keV). In (c) and (d) the spectra of the low-energy detectors, which produce very similar results (Ag M_α and M_β position at 304.7 and 308.3 keV)

Bibliography

[1] A.D Hillier et al. “Muons at ISIS”. In: *Philos Trans A Math Phys Eng Sci.* 377 (2018). DOI: 10.1098/rsta.2018.0064.

[2] Satoshi Mihara. “Muon physics programs at J-PARC”. In: *Physics Procedia* 17 (2011), pp. 153–158. DOI: https://doi.org/10.1016/j.phpro.2011.06.031.

[3] H.K Walter. “Muon Physics at the Paul Scherrer Institut (psi) and at Triumf”. In: *High Intensity Muon Sources - Kek International Workshop*. 2001, pp. 279–290. DOI: 10.1142/9789812791849_0026.

[4] G. M. Marshall. “Muon beams and facilities at TRIUMF”. In: *The Future of Muon Physics*. Ed. by Klaus Jungmann, Vernon W. Hughes, and Gisbert zu Putlitz. Berlin, Heidelberg: Springer Berlin Heidelberg, 1992, pp. 226–231.

[5] S. Cook et al. “Delivering the world’s most intense muon beam”. In: *Physical Review Accelerators and Beams* 20.3 (2017). DOI: arXiv:1610.07850.

[6] S. Blundell et al. *Muon Spectroscopy: an introduction*. Oxford, UK: Oxford University Press, 201.

[7] J.W.G. Thomason. “The ISIS Spallation Neutron and Muon Source—The first thirty-three years”. In: *Nuclear Instruments and Methods in Physics Research Section A: Accelerators, Spectrometers, Detectors and Associated Equipment* 917 (2019), pp. 61–67. ISSN: 0168-9002. DOI: https://doi.org/10.1016/j.nima.2018.11.129.

[8] A. D. Hillier et al. “Muons at ISIS”. In: *Philosophical Transactions of the Royal Society A: Mathematical, Physical and Engineering Sciences* 377 (2137 2019), pp. 1–7. ISSN: 1364503X. DOI: 10.1098/rsta.2018.0064.

[9] Adrian D Hillier et al. “Muon spin spectroscopy”. In: *Nature Reviews Methods Primers* 2 (1 2022), p. 4. DOI: 10.1038/s43586-021-00089-0.

[10] T Matsuzaki et al. *The RIKEN-RAL pulsed Muon Facility*. 2001, pp. 365–383.

[11] C Pizzolotto et al. “The FAMU experiment: muonic hydrogen high precision spectroscopy studies”. In: *The European Physical Journal A* 56 (7 2020), p. 185. ISSN: 1434-601X. DOI: 10.1140/epja/s10050-020-00195-9.

[12] Katsuhiko Ishida et al. *X-ray and neutron studies on the muon to alpha sticking in D-T muon catalyzed fusion*. 1999.

[13] URL: https://www.isis.stfc.ac.uk/Pages/Argus-technical-information.aspx.

[14] Adrian Hillier et al. "Developing the Muon Facilities at ISIS". In: Mar. 2018. DOI: 10.7566/JPSCP.21.011055.

[15] URL: https://www.isis.stfc.ac.uk/Pages/CHRONUS-Technical-Information.aspx.

[16] M. Glaser and M. Kochsiek. *Handbook of Metrology*. Wiliey-VCH, 2010.

Part II

Technique Development

Chapter 3

A new instrument concept for μ-XES at ISIS

The ISIS facility is in continuous development and the refurbishment of some instruments is expected in the future as part of the Endeavour program. At the RIKEN-RAL muon facility, a great effort has already been put into the improvement of muon beam transportation. The next logical step could be the development of a new instrument setup for the elemental analysis. In this chapter, the Monte Carlo software GEANT4/ARBY has been used for the modelling and characterization of a new detector array.

3.1 Different scenarios for an instrument development

The setup described in the previous chapter has proved to be a valid instrument for all the experiments performed in the last few years. However, detectors are subject to ageing and failure, especially if they are not used and kept refrigerated constantly. From late 2021 to early 2023, indeed, due to the pandemic and facility refurbishment, the four HPGe detectors haven't been used or kept cool. This resulted in some failures that were detected during one of the first cycles back after refurbishment in May 2023. In particular, two out of four detectors had to be sent back to ORTEC because of not being able anymore to keep the vacuum. And if for the GMX detector, the solution was the changing of the molecular sieve, for the downstream high energy detector, the problem required the crystal to be sent to the USA factory. Therefore, at the moment of writing the current setup is composed of just three detectors, as shown in Figure 3.1.

In addition to this, during the October 2023 cycle, some failures were experienced with the acquisition. Currently, the data acquisition is provided by NIM crates containing ORTEC, Canberra and TechnoAP boards that are almost 30 years old. These boards, as the detectors, are subject to ageing and failure and spare parts are not always available with short notice. During the cycle, some of them experienced some failure and had to be substi-

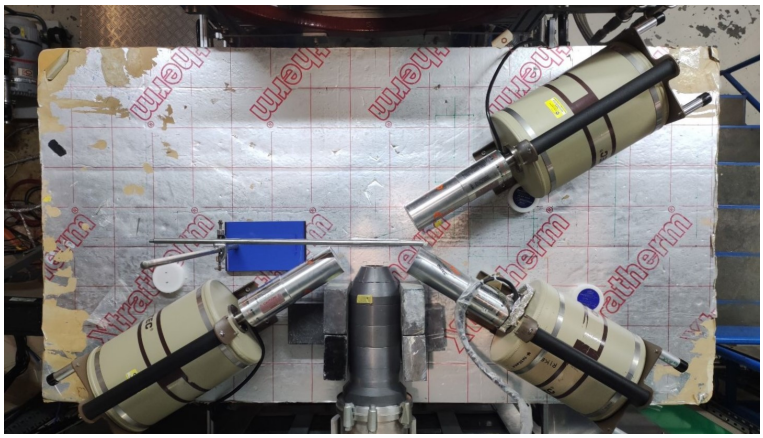

Figure 3.1: The current setup at Port4 (October 2023). The downstream high energy detector was missing due to some failure in the vacuum system.

tuted. Finally, the acquisition system is only based on a Windows 98 old workstation, which represents a problem in case of unexpected faults. These issues, added to the poor solid angle coverage of the setup, the low sensitivity and the long measurement time represent the main downside of the method. Nevertheless, despite relying on an obsolete, yet working, system, the technique has performed continuously and with excellent results in the past few years. It appears clear, in the end, that an improvement of the method in terms of acquisition and detection system is recommended, especially with the recent increase in user demand. An improvement, will not only enhance the capabilities of the technique but will provide users with a more reliable and accessible tool, thus enhancing the science program. At the facility, the upgrade, especially in terms of detector and signal acquisition, is pursued with two possible scenarios:

- Scenario 1: an immediate update of the method, with ready-to-use detectors in place;
- Scenario 2: a future upgrade, based on the development of a germanium array;

The work carried on during the PhD was focused on providing new steps towards the improvement of both scenarios but with particular attention to the second scenario two, which will be described extensively in the following paragraphs.

3.1.1 Scenario 1: the immediate update

The first scenario aims to provide an immediate improvement to the Port4 setup by adding additional HPGe detectors and by coupling the current acquisition with a new desktop digitizer. This approach requires a small investment from the facility and will improve the technique both in terms of detection efficiency and in reducing measurement time, aligning the Port4 setup to the ones present in other facilities like J-PARC or PSI. The first step was

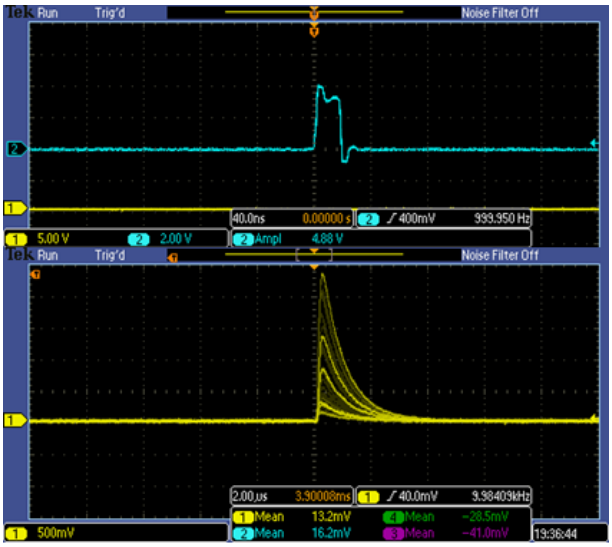

Figure 3.2: The signals simulated with the waveform generator were connected to the oscilloscope for a double check, especially for the accelerator-type one, here in blue (with 50 Hz frequency). The yellow curve is the simulated signal of a radioactive source

done in 2021 when two CAEN Hexagon digitizers were acquired. Hexagon is a stand-alone digital 2-channel MCA that integrates signal conditioning, fast ADC, digital pulse processing and HV and preamplifier power supply in a single compact desktop configuration. In addition, time-stamped list mode allows time and energy events to be saved for offline analysis and post-processing. This desktop digitizer, ideally, would be able to perform all the processing done by the current acquisition. However, after some initial investigation, it was found the hexagon firmware system required significant development. In particular, the main issue regarded the information stored in the list mode. The improvement of the data acquisition system passed from the possibility of storing the trigger timestamp, which at Port4 is given by the ISIS pulse. By storing the trigger information and the successive events, it would be possible to collect all the events following the muon interaction with the sample, providing different types of analysis (i.e, prompt and delayed spectra acquisition or the elimination of background noise). From preliminary measurements performed during the PhD, it was found that this type of information was not saved. Tests were performed by using a CAEN waveform generator to simulate an accelerator-type signal (a positive NIM in this case) and the signal of a radioactive source, as shown in Figure 3.2.

The collection of the Hexagon signal was done with MC2 Analyser, an open software provided by CAEN that enables list mode saving. After going back and forth with the manufacturer, who is responsible for the firmware upgrade, the first progress was made in early 2022, when the time stamp information was finally saved by the list mode. However, when performing additional tests, it was found that whenever no events occurred in the 20 ms window (so when the radioactive source was off) the time stamp information was not

saved. Given that in a real experiment, this can happen quite often, especially if the beam goes off, this was something that required some fixing, so a new firmware update was asked to CAEN. Finally, in early 2023, an updated firmware was provided and during the October cycle, the digitizer was tested again with the waveform generator and with the signal coming from the Port4 detectors. Both tests finally provided the required output, as shown in table 3.1, where a few lines of the list file are reported. Unfortunately, the time for testing during the cycle was relatively short, so further evaluation will be done in February 2024.

Table 3.1: Example of the list file output of the hexagon. In the first column the timetag information: each consecutive trigger reset, flagged as 0x00000008 is separated by 20 ms. Physical events are the ones flagged as 0x00020000, to which an ADC channel is associated. Upon calibration, the ADC channel can be converted to energy. Finally, the 0x00020004 flags 4 are events generated by the firmware and can be eliminated.

Timetag (ps)	ADC Channel	Flags
305631670000	0	0x00000008
323121990000	1206	0x00020004
325631500000	0	0x00000008
327745890000	1000	0x00020004
331205800000	720	0x00020000
332733080000	1370	0x00020000
345631720000	0	0x00000008

The second step of this first scenario was done in July 2023, when four new ORTEC HPGe detectors were purchased. These detectors, similar to the ones already in place at Port4 will be available from March 2024. The acquisition of these HPGe is the logical step for an immediate update: in this way, the setup will increase its solid angle and with spectrum summing, improve its sensitivity and reduce the measuring time. This addition will require the development of a new detector holder for the arrangement around the sample position. Moreover, with eight detectors, a decision about the acquisition will have to be made. The available Hexagons can support only four detectors and the cost of two new boards is not so reasonable. The idea, at the moment of writing, is to set up a DT5560, an open FPGA multi-channel CAEN digitizer. Open FPGA allows the staff to develop a specific firmware for the acquisition that will tailored to the request of the instrument scientist. An intermediate solution, moreover, will be provided by the CHNetMAXI project of INFN. MAXI aims to develop a facility to improve the data collection of negative muon experiments, especially for what regards isotope analysis. In the framework of this project, an 8-channel fast digitizer will be provided with a dedicated acquisition setup.

3.1.2 Scenario 2: the future upgrade

Scenario 1 gives a quick and reasonable solution to the limitations of the method and to the increased demands in beamtime. But to make the method a unique technique in the scientific community, a much more important effort has to be made. The fundamental idea of the second scenario is to surround the sample position with a germanium array, to maximize the solid angle coverage, as shown in Figure 3.3. Similar to what has already been done in many experiments of nuclear physics, like for AGATA and ISOLDE at CERN, Eurica at RIKEN, and RISING at GSI, the implementation of a germanium cluster will provide an exceptional detection setup [1–5]. For these experiments, the array used is the Euroball cluster, an array of 7 hexagonally shaped clover HPGe detectors placed in a packed composition. With this solution, the incremented solid angle coverage, along with bigger detectors, will guarantee shorter measuring time and and an increased sensitivity. This scenario was deeply investigated during the PhD project. Starting from the experiences found in the literature, an HPGe array for the RIKEN-RAL muon facility was designed. Simulations were performed with the ultimate goal of having a single crystal with a good resolution, good efficiency and a fast resolving time. Parameters like length, radius, dead layers and segmentation were modified to find the best compromise. In the end, the modelled configuration was discussed in meetings with the manufacturers, from which two main possibilities for the implementation of the setup emerged.

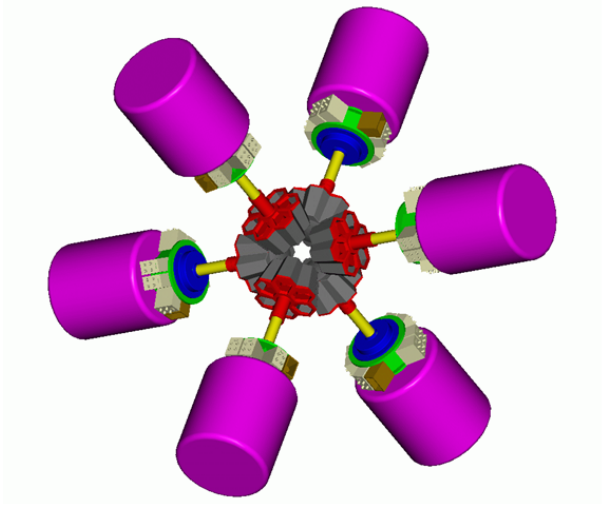

Figure 3.3: Example of a setup with a set of Euroball array developed for the RISING experiment. Figure was taken and adapted from [6].

The Euroball array

Euroball detectors were developed in the early nineties in response to the demand for large γ-ray spectroscopy. Resulting from the collective contributions of multiple European countries, these detectors set new technological limits, marking a significant advancement in γ-ray applications due to their very high sensitivity [7–9]. The starting point of the Euroball arrays were clover detectors. Clover detectors are devices characterized by a minimized crystal holder that reduces the material surrounding the crystal, in a packed configuration that enhances solid angle coverage by incorporating as many HPGe as possible [10, 11]. Basically, the final goal was to enhance resolving power by ensuring high photopeak efficiency and to achieve this, larger detectors were developed. The result of the research led to the development of a closely packed configuration of seven coaxial high-purity Germanium (HPGe) crystals, tapered in hexagonal shape. Each crystal, in addition, was encapsulated in aluminium cups that are singularly kept under vacuum, facilitating replacements in case of failures, as shown in Figure 3.4. Euroball detectors, with their large volumes, were specifically tailored for nuclear structure spectroscopy, with the possibility to measure up to 20 MeV of energy. This PhD is focused on the characterization of the Euroball array with Montecarlo simulations, which will be described in detail in the following paragraphs. However, it is important to answer a question: why the Euroball array? An answer is provided by a recent study published by PSI researchers. In Biswas et al. [12] researchers had the opportunity to perform measurements with an ultimate detector setup, composed of 26 HPGe, out of which 24 were MINIBALL detectors, a cluster of the EUROBALL family composed of 3/4 crystal [3]. By comparing the results of this set of measurements with other previous analyses, with this system, the detection limit went from 0.81 wt% with 10 hours of measurement to 0.4 wt% with 1.5 hours of measurement time. The results, especially in terms of measurement time are remarkable: this means that a measurement that would require an entire day of beamtime, could be performed in around 4 hours. This aspect alone can justify an investment, which for this kind of system is in the order of hundreds of thousands of euros. The configuration, with its enlarged solid angle, will contribute to overcoming the current limitation in terms of sensitivity and measuring time, opening the possibility of new types of applications, from isotope analysis to corrosion studies. Quick and more reliable measurements will be performed, thus responding to the increased demand from the user community. For sure, a setup like this will be highly demanding, especially for what regard funding, expertise and acquisition setup. Even so, it represents the right compromise for improving the technique and making the method more attractive to the user community.

3.2 Characterization of Euroball with GEANT4/ARBY

The main tool used in this work is a Monte Carlo simulation software called GEANT4-ARBY, developed by Professor Oliviero Cremonesi and his collaborators of the INFN division of Milano Bicocca. ARBY is a multipurpose simulation software that incorporates

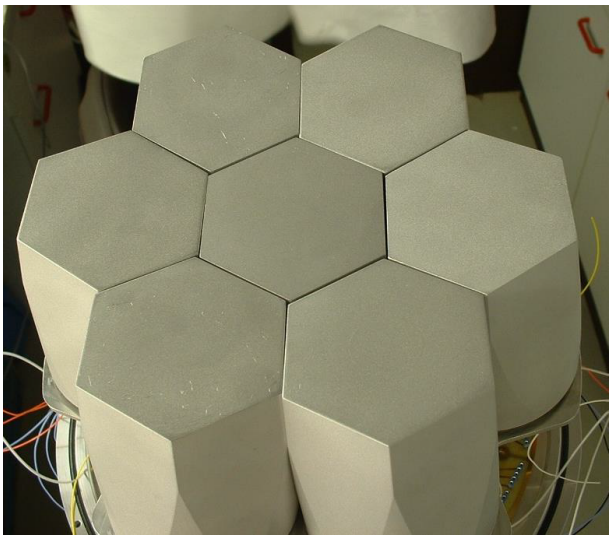

Figure 3.4: Euroball cluster. The hexagonally shaped caps contain HPGe crystals of about 300 cm^3.

all the GEANT4 tools in a user-friendly interface, including the propagation of photons, electrons, muons and many others. The software has been used for many different applications, for example in the efficiency evaluation of HPGe detectors for γ spectroscopy or for bolometric measurements for physics of rare events [13–16]. In ARBY, the simulations do not require a written application as in GEANT4, but a configuration file that stores all the information about the experimental setup (detectors and samples). Parameters such as particle type, direction, and the number of events can be easily accessed through simple command-line instructions, from which the simulation is launched. The output (either text or root file) is processed with dedicated software to obtain a detector response function. Finally, the ARBY tool and all other related software are continuously developed by INFN. These characteristics make ARBY a source for precisely implementing the instrument setup of Port4 and the physical processes involved in the muon irradiation. As described in Chapter 4, the latter still requires some more development, but the particle transportation and the interaction with HPGe detectors have been widely validated, especially for γ and X-rays. Therefore, the software represents a valid tool for the characterization of the Euroball array, which will be described in the following paragraphs.

3.2.1 Modelling of the array

The characterization of the cluster started from the standard array produced by Mirion. An N-type single Euroball crystal is characterised by:

- Dimensions: 70 (diameter) x 78 (height) mm
- FWHM resolution: $<$ 2.36 keV @ 1.33 MeV

- Aluminium wall thickness: 0.7 mm
- Cap-to-Ge distance: 0.7 mm
- Relative efficiency: 55%
- Electrical cooling

In addition, a datasheet was provided by the manufacturer: from that, the single crystal and then the 7 HPGe array were modelled into ARBY. The modelling required some extra effort due to the shape of the crystal and the endcap, but the array shown in Figure 3.5 is a satisfactory model of the real array. The work consisted of different steps, with calculations and simulations performed to evaluate:

- Source-to-detector distance
- Comparison with the current setup
- Detection efficiency
- Add-back efficiency

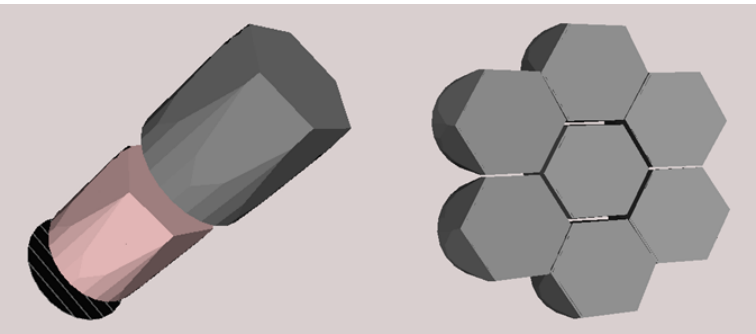

Figure 3.5: Single detector and array. The active volume, in pink, is hexagonally shaped as the aluminium endcap.

Source to detector distance

Prior to the modelling of the array, considerations have been made about the best working distance of the array. Pulsed sources like ISIS, where all the muons are coming in short bunches, experience very high rates that require high segmentation or small solid angles to avoid saturation of the counting system. In particular, at the RIKEN facility, the beam consists of two pulses of 55 ns FWHM, separated by 320 ns with a 20 ms separation between each pulse (for a 50 Hz operation frequency). This means that at the reference

rate of $7x10^4$ muons per second at 60 MeV/c, each muon spill delivers around 700 muons in 55 ns, which are impossible to resolve (see Figure 2.4) [17]. In addition, considering that the duration of the entire process can be averaged to a 1-microsecond, as shown in Figure 3.6, the result is an instant rate of about $1.7x10^9$ muons per second at 60 MeV/c. By making some approximations, one can conservatively assume that this rate is the one seen by detectors (placed close to the source) after the interaction with a sample. It follows that such a high rate will mostly saturate the counting system. Therefore, it is extremely useful to evaluate the source-to-detector distance.

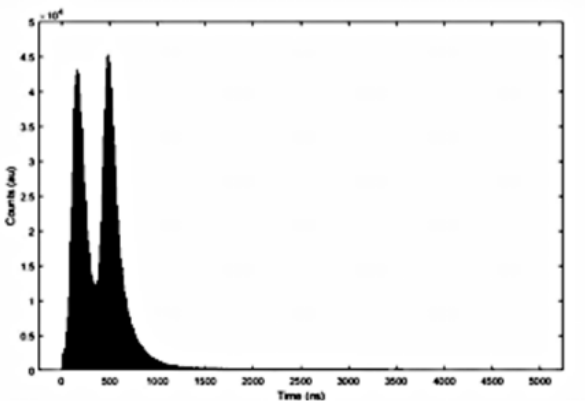

Figure 3.6: The typical double bunch muon pulse: the overall duration of the process can be approximated to around 1 μs.

An important parameter that will discriminate between collection and saturation is the detector dead time. Dead time is the minimum amount of time that has to separate two events so that they can be recorded as separate events [18]. With high count rates, where events can be close in time, losses in counts can be quite an issue, so it becomes important to understand the dead time behaviour. For radiation detectors, there are two principal models for describing dead time behaviour: paralyzable and nonparalyzable. The first describes a system in which if a true event is detected during a dead time window, this event will contribute to dead time by extending its duration. The second, instead, is a system in which during a dead time window, no event is either detected or recorded. These two models predict the behaviour of idealised systems, which are generally a hybrid between the two [19]. From the paralyzable and nonparalyzable expression, one can take into account dead time losses and obtain a relation between the true and recorded count rates. In the case of a pulsed source, the relation states that if the dead time is larger than the pulse but shorter than the separation between pulses, the maximum observable counting rate is just the pulse repetition frequency. At Port4, considering a detection system with 10 μs dead time (, the maximum rate will be 40 Hz since the detector will be able to count just one event per pulse. Therefore, to avoid the overloading of the system, it is important to work at the right source-to-detector distance. With the current setup, the usual working distance ranges from 8 to

20 cm depending on the sample and the momentum. Since flux increases with momentum, the detectors can be moved depending on the experimental settings. As a general rule of thumb, the acquisition of the current setup is counting properly when the recorded counts are about one-third of the incoming events (where the incoming events are the beam pulses, counted with Cherenkov counters). The current working range will have to be modified with the Euroball cluster, given the bigger surface of the germanium crystal. By using the assumption just made, the rate seen by a single Euroball crystal can be easily calculated and is reported in table 3.2. Assuming that the ideal situation, with a 10 μs germanium dead time will be to have a muon for each bunch, the ideal distance is given by an instant rate of about 10^6 muons per second. The table shows that this value sits between 5 and 10 cm for a single crystal. These approximations, help in understanding the most suitable working distance, but many factors can contribute to the calculation, especially for what regards the counting system. Here, the case considered a 10 μs dead time, which is a typical value for HPGe. However, a new digital counting system coupled with fast ADC can improve the detection of radiation. With DAQ, the detector output signals are sampled directly from the charge-sensitive preamplifiers and directly fed into fast digitizers for processing. In this way, it is possible to handle the high instant rates while conserving a good spectroscopic performance. With this acquisition, considering that some systems have a charge collection time in the order of several tens of nanoseconds (80-200 ns depending on the detector parameters), the dead time can be drastically decreased, thus improving the detection capabilities.

Table 3.2: Source to detector distance for a single Euroball crystal at Port4. According to the inverse square law, the intensity decreases as a function of distance, thus reducing the actual rate seen by the detector surface, which for a single crystal is about 30 cm^2

Distance(cm)	Instant rate(μ/s)	Instant rate at detector surface (μ/s)
5	$2.8x10^7$	$2.7x10^6$
10	$7.0x10^6$	$1.7x10^5$
15	$3.1x10^6$	$3.4x10^4$
20	$1.7x10^6$	$1.1x10^4$

Comparison with the current setup

The best source-to-detector distance will influence one of the key parameter improvements of the Port4 setup, the solid angle coverage. Table 3.3 reports a comparison of the solid angle coverage of the Euroball and the current setup. When close to the sample position, due to the use of four different crystals, the current setup is not far from the solid angle coverage. However, this is a distance that, as mentioned, will most likely saturate the acquisition. Thus, the detectors have to be backed up and, considering a reference working distance of 15 cm, there is a factor 3 increase in solid angle coverage with the array. If one considers the

possibility of surrounding the sample position with more than one cluster, the percentage of solid angle covered will increase drastically.

Table 3.3: Comparison between Euroball and the current setup. A single array will provide an increase in the solid angle coverage, especially when the source-to-detector distance increases

	Euroball array		Current setup	
Distance(cm)	Solid angle (sr)	% of 4π	Solid angle (sr)	% of 4π
5	3.58	28.50	2.89	23.06
10	1.95	15.52	0.82	6.61
15	1.14	9.04	0.37	3.02
20	0.72	5.73	0.22	1.71
30	0.35	2.81	0.09	0.77
50	0.13	1.07	0.04	0.27

To better visualize what would be the enhancement in detection efficiency with an array of seven detectors, the current setup was modelled in ARBY and simulations were performed. The modelling of the 4 HPGe in place at ISIS required the information provided in the technical data sheets. A more detailed description of the process will be reported in Chapter 4. The results of this preliminary characterization are reported in Figure 3.7. Here, both setups were placed at 20 cm from a point-like source and the calculated efficiency, the sum of each detector, was plotted. As for the solid angle coverage, a general factor 3 improvement is given by the implementation of the array. From this work, some considerations were made. In the low energy range, efficiency could be increased by using a less attenuating material than aluminium, while in the high energy range, an increase in the length of the crystal could provide a more efficient detection. In addition, a decrease in the radius could allow the placement of more detectors in the same array and reduce the rate seen by the single crystal. And finally, could segmentation provide a better solution? Therefore, modifications to the reference array were done to answer these considerations.

3.2.2 Performance of the array with modified parameters

Among the cited applications of the Euroball array, the crystal sizes are generally fixed, but manufacturers are always keen to listen to requests from buyers. For the AGATA array, for example, the crystal length is 9 cm, whereas the bottom radius diameter is 8 cm. Therefore, it is important to have a clear idea of the ideal setup. The main parameters that affect purely the detection capabilities of the crystal are volume and dead layers. In this case, since dead layer information was not available, the simulations concentrated on the volume changes, in terms of modification of the length and radius size. The latter was mostly investigated because a smaller surface would experience less radiation flux, thus preventing saturation and allowing to fit more crystals in the same working area.

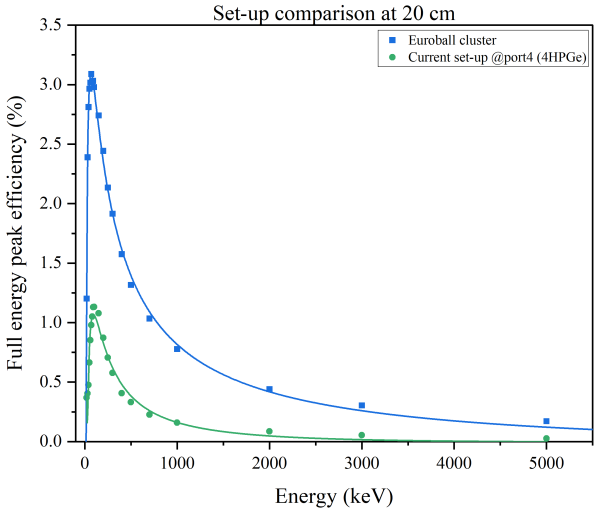

Figure 3.7: Detection efficiency of the Euroball array (blue) and the current setup (green) at 20 cm from sample position.

Simulations with modified lenght

An increase in the crystal length aims to improve the efficiency in the high energy range. As shown in Figure 3.8, a 1 MeV γ-ray is almost entirely stopped by 7.77 cm of germanium, but for 5 MeV, the crystal is more transparent. Thus, an increase in size allows for a better detection efficiency of high-energy radiations. Maximizing this energy range, as mentioned would help in applications like isotopic analysis.

To evaluate the contribution of the length parameter to the detection efficiency, simulations were performed by decreasing and increasing it. Length was changed with 1 cm step, up until 11.77 cm and down to 5.77 cm. In particular, to evaluate the efficiency variation, a point-like source was placed on the top of the aluminium cap of a single Euroball crystal and single γ-ray energies (from 20 keV to 5 MeV) were simulated. The simulation output was fed into software that produces the detector response function and the spectra were analysed by fitting peaks with a Gaussian function. From that, the full energy peak efficiency was calculated for each radiation and compared to the Euroball reference crystal. Results are reported in Figure 3.9. A reduction in length (and indeed volume) does not affect the efficiency at low energies up to 300 keV, as shown in Figure 3.9a. This is mainly because the radius of the two crystals is the same and at low energies, γ-rays are fully absorbed. After that, as one would expect, the difference between the modified crystal and the reference one increases, with discrepancies that are up to 10% at 5 MeV, especially for a reduction of 2 cm. On the other hand, the increase in size does not produce significantly different results, as shown in Figure 3.9b. Only in the very high energy range, an increased efficiency is observed, but discrepancies in the calculated efficiency are generally no more than 3%. It has to be mentioned that there are small discrepancies that could be due to geometric effects,

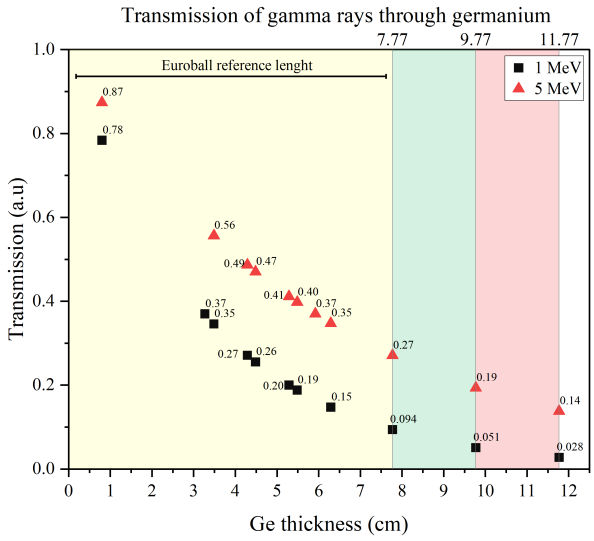

Figure 3.8: Transmission of a 1 and 5 MeV γ-ray through germanium. Mass attenuation coefficients were taken from [20].

like small variations in the source-to-detector distances. Anyway, as shown in figure 3.8, differences in the 1 MeV range are minimal when increasing size.

Simulations with modified radius

As one would expect, by reducing the radius more significant effects are observed. Here, the radius was decreased by 1 cm (from 3.5 to 2.5 cm) and simulations with reference length (7.77 cm) and increased length (8.77) cm were performed. Results are reported in Figure 3.9 c and d. In both cases, the detection efficiency remains constant up until 100 keV. As energy increases, given the smaller volume of the crystal, the discrepancy with the reference crystal becomes more evident. A change in the volume radius would be a trade-off between losing efficiency and decreasing the rate seen by the crystal. However, the array configuration allows to the minimisation of energy losses, thanks to the proximity of the detectors and the addback function that will be described in the following paragraphs. In addition, the combination of a reduced radius and an increased length would provide a good compromise.

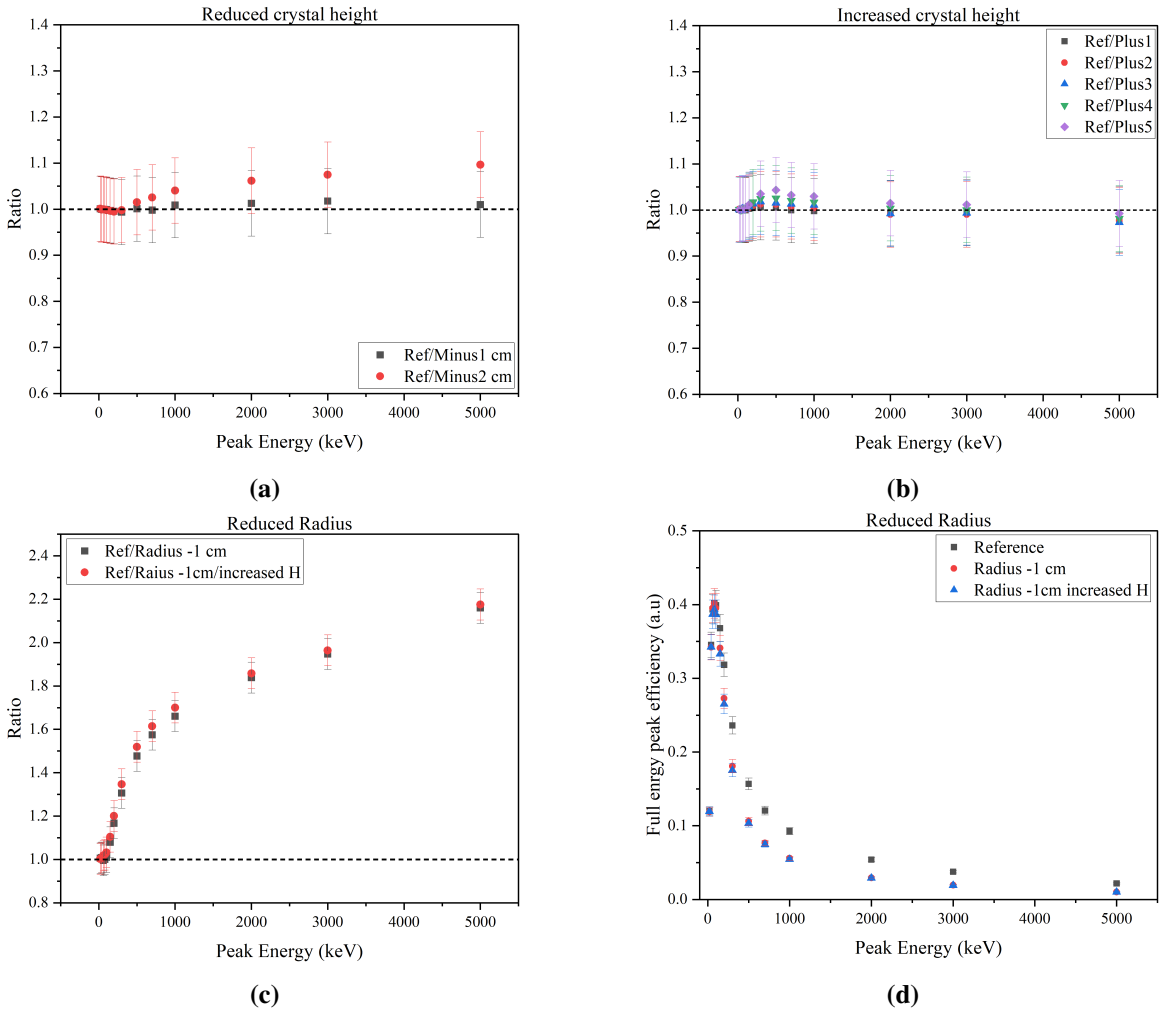

Figure 3.9: a) length decrease: for a reduction of only 1 cm, the difference between the calculated efficiency is minimal even at high energies, whereas for the 2 cm reduction, the effect is more evident. b) length increase: the effect of the efficiency increase is minimal, especially at low energies (where the main discrepancies are mostly due to geometric effects). c,d) effect of a decreased radius: while until 100 keV the FEP is not changed, the increase in energy provides a big discrepancy with the reference crystal. With a reduced surface area and an isotropic source, more high energy γ-rays are escaping the active volume or not even interacting with it, thus reducing the detection efficiency.

Simulation with modified endcaps

The encapsulated crystals of the Euroball array are contained in an additional aluminium container. For low-energy applications like the one that can be performed with μ-XES, these extra layers can prevent the acquisition of low-energy X-rays. Aluminium is commonly used as a crystal holder, but for classic HPGe, beryllium or carbon-fibre windows in the front of the endcap allow the detection of low-energy radiation. As shown in Figure 3.10a

beryllium is the best material for windows, but it is fragile and toxic, so carbon fibre would be preferable.

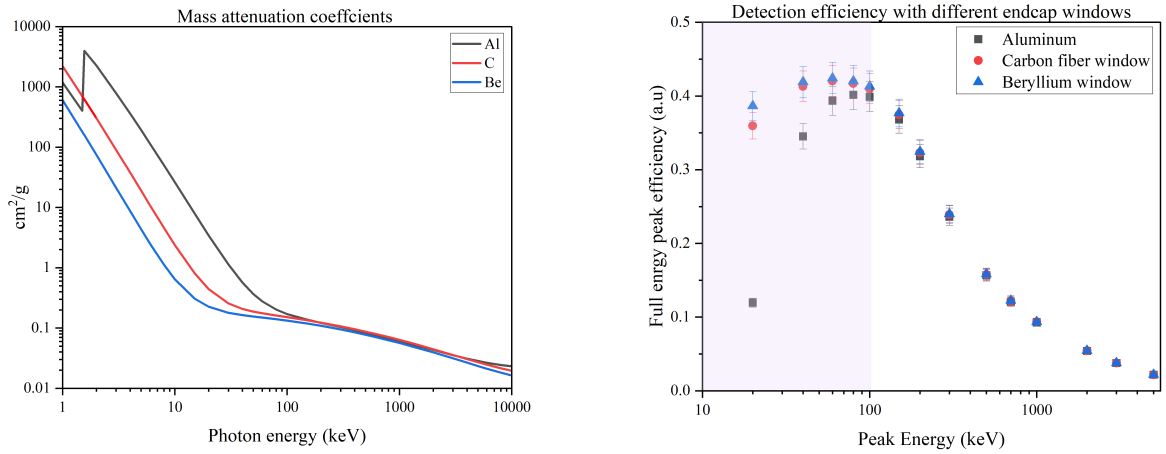

(a) **(b)**

Figure 3.10: a) Mass attenuation coefficients of the most common endcap window materials. A 10 keV photon is attenuated of its 84% by Al, 4% by Be and 15% by carbon fibre. Data were taken and adapted from NIST database [20]; b: effect of different endcap windows on the detection efficiency. For low-energy applications, aluminium should be avoided due to its high attenuation of the incoming radiation.

Simulations were performed to evaluate the detection efficiency with carbon fibre and beryllium windows. As in the previous paragraph, a point-like source was placed on top of the endcap and single γ-ray energies were generated from a few keV to 5 MeV. As expected, in the low energy range, up to around 100 keV, the detector with a beryllium endcap has better efficiency. At 20 keV, for example, there is a factor 3 gain in efficiency both for the beryllium and the carbon fibre window compared to the reference detector. This set of simulations was performed with the idea of presenting the manufacturer with a different approach to their common product. However, given that the capsules are singularly kept under a vacuum, it would be complicated to have a window of a different material.

3.2.3 Addback efficiency

In clover detectors, the total full energy peak efficiency is given by the sum of two correlated effects: the full γ energy deposited in the single crystal and the full γ energy resulting from the partial absorption in two or more crystals. When a γ-ray hits the detector, indeed, it can be fully absorbed or scattered. If scattered, there will be a partial absorption of the energy, that will contribute to the Compton continuum. The partially absorbed γ-ray, however, can then enter an adjacent crystal and interact again, by being fully absorbed or scattered again. The energy of this scattered γ-ray can be reconstructed and added to the

total full energy peak efficiency (FEP), thus increasing the counts in the full energy peak and decreasing the Compton continuum. Especially valid for high-energy radiation, that will most likely interact with one or more crystals, this method, called "Addback efficiency", enhances the capabilities of the cluster [21, 22]. In experiments, addback mode is performed with coincidence measurements: the individual signals deposited in adjacent detectors are saved in list mode and the addback efficiency is given by the time-correlated sum of these events. In ARBY simulations, addback was evaluated by summing the energy of the events occurring in the same crystal. The list mode output provided by ARBY is a five-column file containing the event number, timing information, the detector in which the signal was collected (labelled from 0 to 6) and the relative energy (plus a column of zeros). In this file, when a signal interacts with more than one crystal, the related event number is not changed. Therefore, a γ-ray interacts with detectors 1 and 2, there will be two following rows with the same event number. By taking advantage of this characteristic of the output file, a Python script that grouped the events with the same value and summed their energies was implemented:

```
[...]
 filename = os.fsdecode(file)
 if filename.endswith(".txt"):
     df = pd.read_csv(filename, sep='\t', header=None,
        skiprows=(1))
     #row 1 describes the simulation setup
     df.columns = ["event", "time", "detector","energy",
         "val"]
     df = df.groupby('event').agg({'time': 'first','
        detector':'first','energy':'sum', 'val':'first
        '}).reset_index()
     [...]
```

The code, by summing the energy of the scattered events, simulates a coincidence measurement of events occurring in more than one crystal. The simulations were performed with single γ-ray energies generated from a point-like source placed at 10 cm from the array. The output of each simulation was treated with the code and fed into the software that produces the detector response function. The obtained spectra were analysed and the FEP was calculated for each simulated peak, both in standard and addback mode. Results are shown in Figure 3.11. The addback factor, calculated as the ratio of the addback FEP to the standard FEP, indicates that for energies $<$300 keV the addback and standard mode do not differ, since the energy is entirely deposited in the crystal. Then, as the γ-ray starts to undergo compton scattering, the addback contribution increases, with a 25% rise in efficiency at 1 MeV.

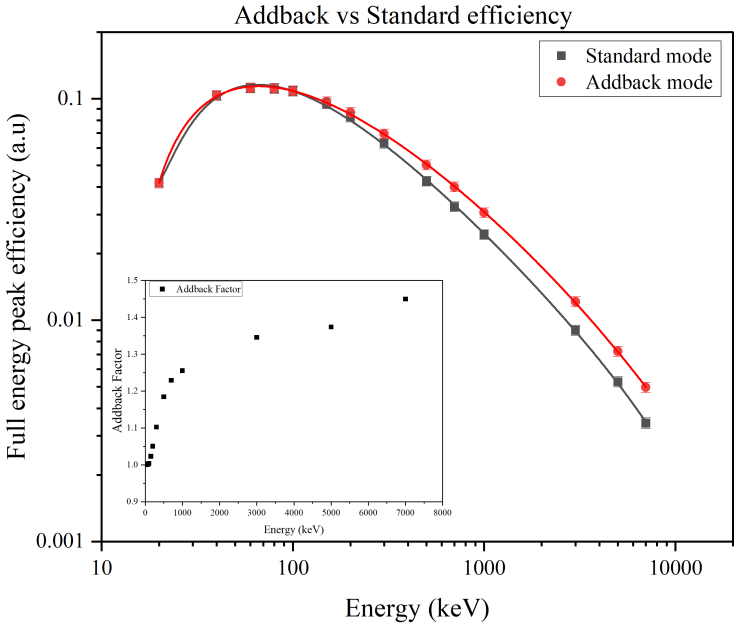

Figure 3.11: Comparison between standard mode (signal treated separately) and Addback mode. The increase in efficiency is negligible at low energies but increases steadily with the increase of the γ-ray energies. Simulations were performed with a point-like source placed 10cm from the array. As a measure of the enhanced FEP The addback factor, the ratio of the addback FEP to the standard FEP, is also plotted.

In elemental analysis with negative muons, this method will open to a more straightforward use of the high energy part of the X-ray spectrum, which with the current setup is mostly unused. With increased efficiency, the K_α and K_β peaks of high Z atoms could be used for elemental analysis, not only for major components but also for trace elements. When minor components are present, for example, arsenic, antimony or lead in a copper alloy, their most intense peaks are generally out of the good efficiency range of the current setup. By working in addback mode with a Euroball array, indeed, the summing of the output of the detector could provide an increase in the sensitivity of the method. Furthermore, the possibility of detecting high-energy X and γ-rays will be a useful tool for isotopic analysis: for example, with the cluster, the 6 MeV lead K_α X-rays could be detected.

3.2.4 Final configuration

The idea of all this modelling reported in these few paragraphs was to gain knowledge about the performance of the array and to be prepared for a discussion with the manufacturer. The results show that a good compromise between good efficiency in a wide energy range and a lower rate on the detector surface is given by a crystal with increased length and reduced radius. Modifying the latter, in addition, would allow to fit more crystals in about the same

size as the reference array. The Euroball array has a total bottom diameter of about 21 cm. If the detector radius is decreased by just 1 cm, it would be possible to fit from 10 to 12 detectors more, thus coping with the efficiency and solid angle loss of a smaller crystal. An increased number of detectors will surely enhance the detection efficiency, even at high energies, where the add-back mode could provide good efficiency by reconstructing high-energy scattered events.

Segmentation

The final crystal configuration, however, is not just a modified crystal. Before presenting the results to the manufacturer, the segmentation of the crystal was added to the modelling. Segmentation, indeed, could represent a solution to the request for good resolution in the low-energy range and good efficiency in the high energy, a request that would not be completely satisfied with a single crystal configuration. Therefore, the final configuration consisted of a 3-segment crystal, with a 0.8 cm front segment and two back segments of 4.49 cm each, for a total length of 9.77 cm and a bottom diameter of 5 cm, as shown in Figure 3.12. The thin front segment will cover the very low-energy range (10 KeV $<$ E $<$ 150 KeV), with a requested resolution of 0.5 keV at 122 keV and a reduced surface area to decrease the rate and prevent form crosstalk. The two back segments, instead, will cover the medium to high energy range ($>$ 150 KeV), with efficiency enhanced with addback acquisition mode. To improve the detection, a beryllium of carbon fibre window is placed on the crystal endcap.

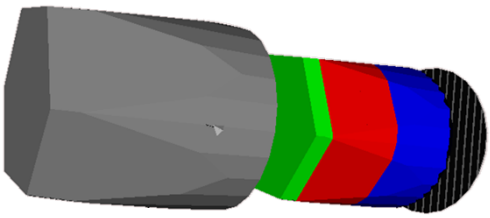

Figure 3.12: Final configuration: an encapsulated segmented crystal.

3.2.5 Proposal and discussion with the manufacturer

The final configuration was proposed to the manufacturer, which for confidentiality reasons would not be mentioned, in a series of meetings during early 2023. At first, the discussion regarded the feasibility of a segmented crystal, which was accepted but with some pondering. Firstly, since each crystal is singularly kept under vacuum, a configuration with an endcap made either with beryllium or carbon fibre would have required R&D, thus increasing costs. What could be done is to use the detectors without the aluminium container that seals the array. Secondly, the maximum length that they can provide for a crystal is 10

cm: as for the endcaps, more will require R&D and will be time-consuming, adding extra costs. Finally, the manufacturer was not confident that a 0.8 cm front slice would have been be enough to get a 0.5 keV resolution at 122 keV. Therefore, they replied with a counter-proposal, that consisted of a telescope configuration. The counter-proposal is confidential, therefore it is not possible to give too many details. However, the basic principle is that to answer a certain type of request, a hybrid solution could be a telescope configuration. In telescope detectors, several coaxial or planar detectors are stacked together to achieve wide energy range measurements with high efficiency and background correction, with minimized dead layers between each area. The scenario proposed involves the use of a thin crystal in front of a Euroball-type crystal. In this way, the front crystal will provide the required resolution and efficiency for the low-energy part of the spectrum, while the Euroball crystal will provide the required efficiency for the high-energy part of the spectrum. With a smaller crystal on top, the manufacturer can guarantee a good resolution, which instead they won't be able to do for a segmented crystal. This configuration, as the Euroball, would be implemented as an array. The structure, in conclusion, will be similar to a Euroball with an additional detector on top. The main drawback of this approach is the presence of extra dead layers that would be in place for mounting the front crystal. Therefore, there could be some loss in resolving power in the medium energy range, whose radiation could be absorbed by the dead layers. A solution could be provided by using other materials than aluminium, like carbon fibre. This, anyway, would require some R&D. Finally, both detectors will have the same cryostat. In conclusion to the discussion, both parties agreed on two possible scenarios for a future array:

- A segmented, 100 mm long with reduced radius Euroball-type detector, resulting from this PhD work;
- An encapsulated telescope configuration with a smaller detector on top of a bigger crystal, proposed by the manufacturer.

Both configurations will require research and development from the manufacturer since they will be unique approaches to the construction of an array. As mentioned, information is confidential, so the cost won't be discussed here. However, it is clear that the costs of developing a prototype or for R&D are quite high. Thus, the investment for a Euroball-type array will be highly demanding, both in terms of research and development and in founding. Considering that is not mandatory to buy the entire array, but also piece by piece, the investment could be diluted in several years. This, yet, are consideration that is up to the ISIS facility and the Muon group, which will have the final word on the investment. The project and the work done in the PhD aimed at providing them with all the necessary sources to make the best decision for the improvement of the μ-XES technique.

Bibliography

[1] Jemima Cresswell, Werner Gast, and Forschungszentrum Jülich. *AGATA, Technical Proposal for an Advanced Gamma Tracking Array for the European Gamma Spectroscopy Community*. 1991.

[2] P. A. Söderström et al. "Installation and commissioning of EURICA - Euroball-RIKEN Cluster Array". In: *Nuclear Instruments and Methods in Physics Research, Section B: Beam Interactions with Materials and Atoms* 317 (PART B Dec. 2013), pp. 649–652. DOI: 10.1016/j.nimb.2013.03.018.

[3] P Reiter et al. "The MINIBALL array ". In: *Nuclear Physics A* 701 (2002), pp. 209–212.

[4] N. Warr et al. "The miniball spectrometer". In: *European Physical Journal A* 49 (3 2013), pp. 1–32. DOI: 10.1140/epja/i2013-13040-9.

[5] H.J. Wollersheim et al. "Rare ISotopes INvestigation at GSI (RISING) using gamma-ray spectroscopy at relativistic energies". In: *Nuclear Instruments and Methods in Physics Research Section A: Accelerators, Spectrometers, Detectors and Associated Equipment* 537.3 (2005), pp. 637–657. ISSN: 0168-9002. DOI: https://doi.org/10.1016/j.nima.2004.08.072.

[6] RISING Photo sampler. *https://web-docs.gsi.de/wolle/EBatGSI/PHOTOS/photos−stoppedbeam.html*. 2004.

[7] J. Eberth et al. "Development of composite Ge detectors for EUROBALL". In: *Nuclear Physics A* 520 (1990). Nuclear Structure in the Nineties, pp. c669–c676. DOI: https://doi.org/10.1016/0375-9474(90)91183-R.

[8] F A Beck. "EUROBALL: Large Gamma Ray Spectrometers through European Collaborations". In: *Frog. Part. Nucl. Phys* 28 (1992), pp. 443–461.

[9] J Simpson. "Euroball: Present status and outlook". In: *Acta Physica Hungarica New Series Heavy Ion Physics* 6 (1 1997), pp. 253–264. ISSN: 1588-2675. DOI: 10.1007/BF03158502.

[10] F A Beck. "Performances of a new type of Ge detector: the clover detector". In: ().

[11] M Saha Sarkar et al. "Characteristics of a Compton suppressed Clover detector up to 5 MeV". In: *Nuclear Instruments and Methods in Physics Research A* 491 (2002), pp. 113–121.

[12] Sayani Biswas et al. "The non-destructive investigation of a late antique knob bow fibula (Bügelknopffibel) from Kaiseraugst/CH using Muon Induced X-ray Emission (MIXE)". In: *Heritage Science* 11 (1 Dec. 2023). DOI: 10.1186/s40494-023-00880-0.

[13] M Pavan et al. "Control of bulk and surface radioactivity in bolometric searches for double-beta decay". In: *The European Physical Journal A* 36 (2 2008), pp. 159–166. ISSN: 1434-601X. DOI: 10.1140/epja/i2007-10577-0.

[14] C Alduino et al. "The projected background for the CUORE experiment". In: *The European Physical Journal C* 77 (8 2017), p. 543. ISSN: 1434-6052. DOI: 10.1140/epjc/s10052-017-5080-6.

[15] C. Alduino et al. "Measurement of the two-neutrino double-beta decay half-life of 130 Te with the CUORE-0 experiment". In: *European Physical Journal C* 77 (1 Jan. 2017). ISSN: 14346052. DOI: 10.1140/epjc/s10052-016-4498-6.

[16] D. Q. Adams et al. "Search for Majorana neutrinos exploiting millikelvin cryogenics with CUORE". In: *Nature* 604 (7904 Apr. 2022), pp. 53–58. ISSN: 14764687. DOI: 10.1038/s41586-022-04497-4.

[17] T Matsuzaki et al. *The RIKEN-RAL pulsed Muon Facility*. 2001, pp. 365–383.

[18] Glenn F Knoll. *Radiation detection and measurement; 4th ed.* New York, NY: Wiley, 2010.

[19] V Bécares and J Blázquez. "Detector Dead Time Determination and Optimal Counting Rate for a Detector Near a Spallation Source or a Subcritical Multiplying System". In: *Science and Technology of Nuclear Installations* 2012 (2012). Ed. by Alberto Talamo, p. 240693. ISSN: 1687-6075. DOI: 10.1155/2012/240693.

[20] J Hubbell and Stephen Seltzer. *Tables of X-Ray Mass Attenuation Coefficients and Mass Energy-Absorption Coefficients 1 keV to 20 MeV for Elements Z = 1 to 92 and 48 Additional Substances of Dosimetric Interest*. 1995.

[21] R. Kshetri. "Modeling of clover detector in addback mode". In: *Journal of Instrumentation* 7 (7 July 2012). DOI: 10.1088/1748-0221/7/07/P07008.

[22] P.K Joshi et al. "Study of the characteristics of a clover detector". In: *Nuclear Instruments and Methods in Physics Research Section A: Accelerators, Spectrometers, Detectors and Associated Equipment* 399.1 (1997), pp. 51–56. ISSN: 0168-9002. DOI: https://doi.org/10.1016/S0168-9002(97)00871-1.

Chapter 4

The GEANT4/ARBY simulation software

The GEANT4/ARBY tool, introduced in the previous Chapter, has been used in many different research projects at the University of Milano Bicocca. In this Chapter, its use for the simulation of the interaction of a negative muon beam will be described.

4.1 Software for technique development

Monte Carlo simulation software are invaluable tools for the progress and development of many projects in the scientific community. Especially in particle physics, where the complexity and scale of experiments are increasing, having simulation software that precisely implements all the phenomena and hardware involved in an investigation is of key importance. GEANT4, FLUKA and MCNP are among the most used tools to handle the transportation of particles and all the related physical processes [1–3]. The first is developed via international collaboration and provides users with all the instruments necessary to run applications that describe the geometry (experimental setup and detectors), the particles and the physical processes of a given experiment. As with other software, the GEANT4 code is open source and can be handled by users and developers to best suit their requirements. At the Milano Bicocca section of the National Institute of Nuclear Physics (INFN), the weak interaction group utilises GEANT4 through a user-friendly software called ARBY, already described in Chapter 3. ARBY, with its ease of application and possibility of small modification, represent an invaluable tool for the development of the Muonic atom X-ray Emission Spectroscopy. Having simulation software that precisely implements not only the instrument setup but also the physical process can provide another source of improvement for the method, especially in terms of data analysis. Moreover, with ARBY, it is possible to replicate calibration and efficiency measurement, thus reducing the handling of radioactive sources and reducing the time for setting up. In this work, other than GEANT4/ARBY,

SRIM-TRIM and MuDirac have been used and will be described in the next paragraph. This Chapter, in particular, will be devoted to the implementation of the ARBY tool.

Dirac equation solver: MuDirac

As mentioned in Chapter 1, Dirac equation solvers provide a rapid solution to the calculation of muon transition energies. MuDirac, in particular, is an open-source software developed by the ISIS computational group that calculates the muonic transition energies for any given atom [4]. The software was developed with the idea of helping users with the muon elemental analysis. It is able to compute most muonic transition energies and probabilities, taking into account the effect of finite size, vacuum polarizability and electronic shielding. In addition, the software provides a simulated spectrum with the calculated transitions. MuDirac works from the terminal and the calculation parameters are stored in an input file. The user can select the transitions to calculate for a given atom, the model used to describe the nucleus, the electronic configuration etc. (for a detailed description and the code see the GitHub page [5]).

Particle transportation with SRIM-TRIM

The Stopping and Range of Ions in Matter (SRIM) is a collection of software which calculates many features of the transportation of ions in matter [6]. In particular, with SRIM, with the TRIM application (Transport of Ions In Matter), it is possible to calculate the stopping powers and range of any given ion at any energy in any elemental target, with the possibility of multi-layer configurations. The program works from a desktop interface in which input parameters are stored for the simulation. Muons are not listed in the particle list, so for simulations, a hydrogen ion with a mass of one-ninth of its original value is used (this approach works because the energy loss of the muon in matter is similar to the one of a small proton). The software provides a very useful tool for simulating the penetration depth of muons into matter.

4.2 GEANT4/ARBY validation

4.2.1 Muon interaction process

The GEANT4 class currently responsible for the muon cascade process is the G4Em Capture Cascade and is reported in Appendix A[7]. This class was created a few years ago and as stated in the code it “calculates the energy of a K mesoatom level using the energy of the hydrogen atom by taking into account the finite size of the nucleus”. The class includes a list of 28 atoms and their *1s* energy. Since its creation, very few updates have been made, mostly because a lot of effort is required for the development of a class, especially if there is little interest in the topic. From preliminary simulations of negative muons analysis, some

issues in the calculations were found, so to further characterize the software, an extensive set of simulations was performed. Simulations covered a large part of the periodic table, 21 elements ranging from lithium to bismuth (launched with GEANT4 version: 10.04.p03). Since the interest was mainly devoted to the detection of all the emitted X-rays, a very simple geometry was used. A small rod of the selected element was placed in a cylinder made of germanium, to simulate a 100% efficient detector (Fig. 4.1). Then, the interaction with a 30 MeV/c muon beam was simulated (with an average of 10 million events simulated). The simulation output (.root or .txt file) was processed in a dedicated software that reproduce the detector response, with the final product in the form of an energy spectrum.

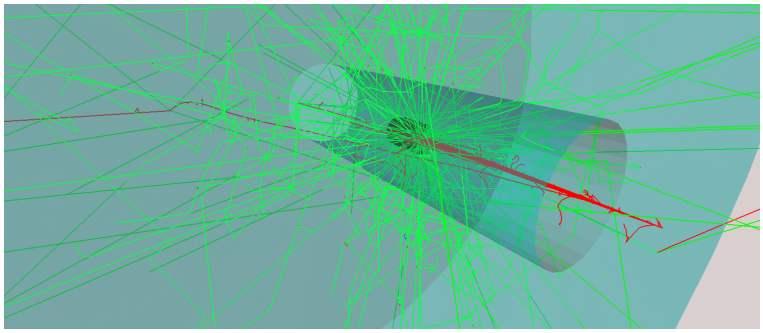

Figure 4.1: Basic setup of the simulations: the negative muon beam (in red) is generated from a point-like source and hits a target placed inside the germanium active area (blue). With this configuration, most of all the generated radiations are collected by the crystal

Results of the K, L and M lines for some of the simulated elements (that cover the low and high Z region) are reported in Table 4.1. For the lower energy emissions, corresponding to the L and M lines, the agreement with the literature is good, with energy differences generally lower than 2 keV (except for gold and silver, where the delta is higher). It has to be stated that even in literature there is some deviation in the listed values, so an energy delta within 2 keV is acceptable. The main differences are in the high energy region of each atom, corresponding to the K_α and K_β lines. For these lines, the delta is always above 10 keV, increasing with Z but without a well-defined pattern (this deviation was observed in all the simulated atoms). If not missing, some K_β transitions are present with a very low peak intensity. In addition, some peculiar characteristics of the spectra are missing: copper, for example, is characterized by the presence of a double peak at 330 and 336 keV and 1507 and 1514 keV. These double peaks, as shown in Figure 4.2, are missing in the GEANT4 simulated spectra. So, even if most of the low energy peaks are well reproduced, problems are present also in this region of the spectra. It is evident, anyway, that from this first set of simulations, the main problem of the cascade resides in the calculation of the k-shell transitions.

The issue described above was also identified during the simulation work for the FAMU experiment by the INFN group of Trieste. FAMU is an international collaboration whose

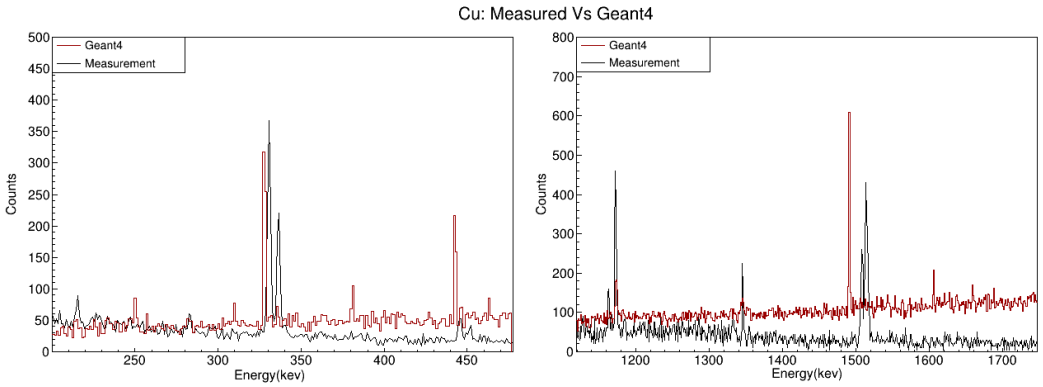

Figure 4.2: Comparison between a real measurement (in black) and a GEANT4 simulation (in red). Copper is easily distinguished by a double peak around 330 keV and 1500 keV. The GEANT4 simulation, in this case, is not able to reproduce the experimental data, since just one out of the expected peak is present

goal is to measure the proton Zemach radius with the measurement of the hyperfine splitting of the muonic hydrogen ground state [8]. To tackle the problem, the group implemented the GEANT4 class by increasing the listed number of atoms from 28 to 57 and by adding a small correction to the calculation of the K shell transitions. For the FAMU experiment, however, the interest was mainly in low Z atoms, so the implementation wasn't evaluated for the atoms with Z higher than oxygen. Thus, to test the modified class, an extensive set of simulations was performed. To distinguish the results from the previous ones, ARBY/GEANT4 is called ARBY/Mux. Results of the K, L and M lines are reported in Table 4.2. As for the ARBY/GEANT4, the L and M lines are in agreement with the literature with the exception of silver and gold, all within a 2 keV delta. Regarding the K transition, the correction produced a good agreement with the literature for the low Z atoms like aluminium and silicon, with a very small difference from the literature data. For high Z atoms, instead, the situation is not improved. With the modified class K_α are completely missing, while K_β are present but with a delta energy that increases with Z. Figure 4.3 reports the simulated spectra from each of the two ARBY versions to better visualize the differences in the high-energy transitions. Figure 4.3a shows that with ARBY/Mux, the peaks are shifted to higher energies to match the expected values, whereas for the low energy peak, there is no difference between ARBY/GEANT and ARBY/Mux. If Z increases, as shown in Figure 4.3b, peaks are shifted, but the signature double peak of copper is still missing. So, even with the updated class, GEANT4 is still not able to reproduce properly the K shell transition.

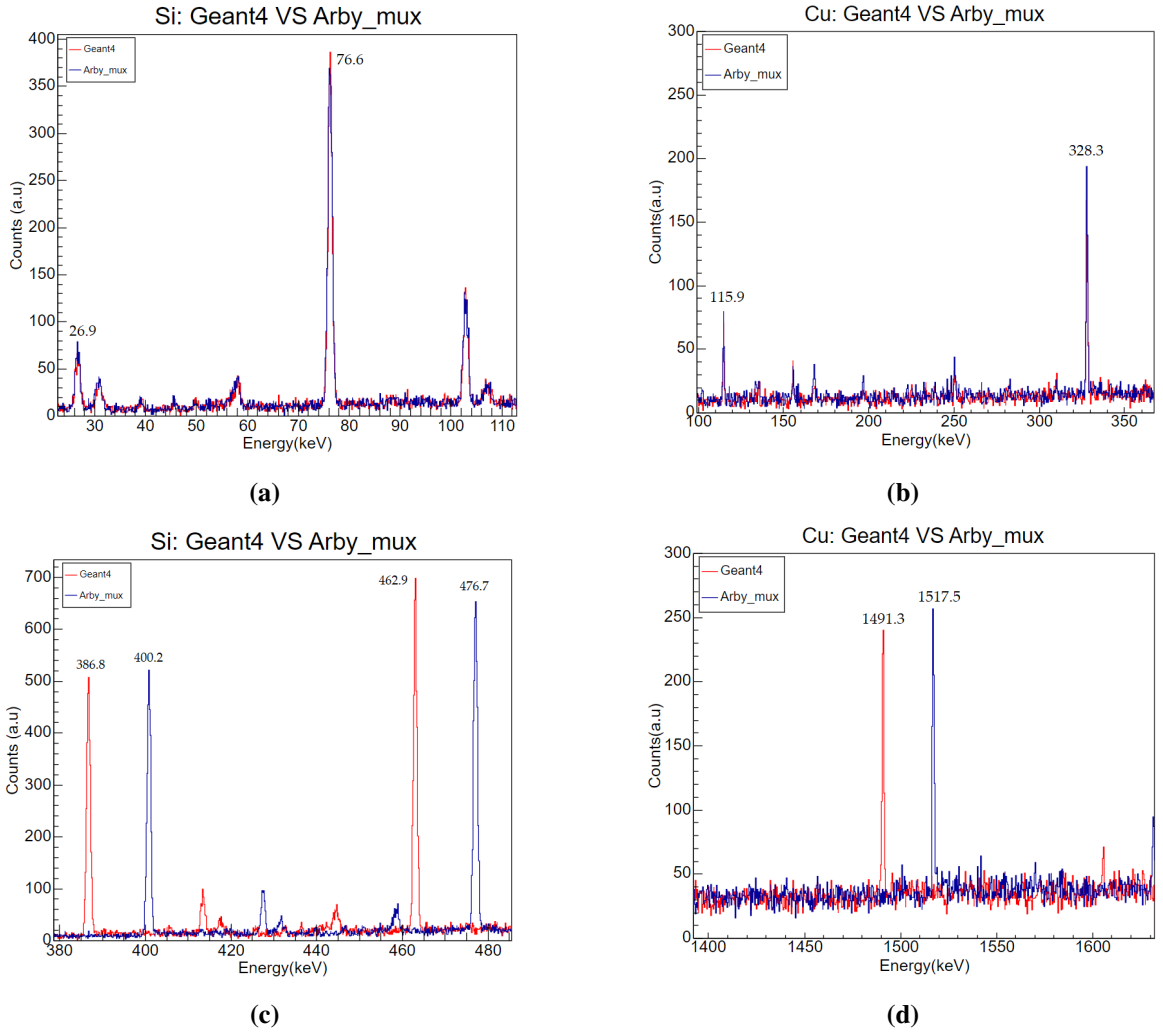

Figure 4.3: L transitions energy range: for (a) silicon and (b) copper, the two Arby versions give the same output. K transitions energy range: (a) Silicon; (b) Copper. As stated in the text, for low Z atoms like silicon, the K_α and K_β transition are well reproduced, whereas for elements with higher atomic numbers just one transition is simulated or the second one is present but with very low intensity, just above noise level.

Implementing GEANT4 with MuDirac

A solution to improve the reliability of the simulation could be provided by a data-driven library. The implementation of a new database in GEANT4 has already been employed in some processes, like for the Low Energy Electromagnetic package, responsible for the simulation of atomic relaxation [9]. Recently, the generation of the X-ray and Auger emission from the process has been implemented by a data-driven database (called ANSTO, both for ionisation cross sections and transition probabilities) to be used along with the default one

[10]. The implementation of a database, moreover, requires less manpower than the editing or the development of an entire class. The idea proposed here is to use a third-party software, MuDirac, to create the database. MuDirac calculates the transition energies of the cascade and produces an output in which the transition energy is associated with the transition rate (in s^{-1}). In addition, the software provides a simulated spectrum with the calculated transitions. MuDirac works from the terminal and the calculation parameters are stored in an input file. The user can select the transitions to calculate for a given atom, the model used to describe the nucleus, the electronic configuration etc. To create the database, calculations for the most abundant isotopes - from hydrogen to bismuth - were performed. For each simulation, the starting level for the cascade calculation was selected as $n = 6$. It is well known that the radiative emission after negative muon capture becomes dominant at the end of the cascade when the approaches the lower muonic orbitals, so there was no interest in increasing the starting level. Anyway, this setting can be modified based on interests. The output of the MuDirac calculation selected for the database was the ".dat" file containing the simulated spectrum data, a of two columns file with energy and intensity. To make the database available in GEANT4/ARBY, the ARBY setup file was edited with an environment variable pointing to the folder containing all the calculated outputs. When a simulation is launched, if a Mudirac file of the given specimen is found, the energy corresponding to the transition is extracted and used by GEANT4. If the file is missing, a warning is generated, and the program continues the simulation with the standard cascade generation. A preliminary test with this edit ARBY version, called "ARBYMuDirac" where performed to evaluate the feasibility of the approach (dedicated GEANT4 version: 11.1.1). With this approach is of key importance to have a MuDirac output as complete as possible. By using the database, indeed, the information coming from the cascade calculation made by GEANT4 is lost: with the MuDirac, indeed, a single deexcitation is generated instead of the entire cascade. The process of capture is maintained, and γ-rays are generated. The results of the simulations are reported in Table 4.3: here, the K transition columns have agreement between simulations and literature, with a delta lower than 2 keV. In addition, with the MuDirac database, some low-energy peaks are adjusted in position. This happens not only for the lines in the table but also for some other peaks in the spectrum. For instance, copper K and L lines are reported in Figure 4.4. Copper is easily distinguished by a double peak at 330 and 336 keV, other than the one at 1.5 Mev. This double peak, as shown in Figure 4.4a is not present in the ARBYMux version, while it appears in the MuDirac version of ARBY. This means that, by setting a precise parameter of the Mudirac calculation, it is possible to have an overall correction along the spectrum, especially in critical points like the one used for element identification.

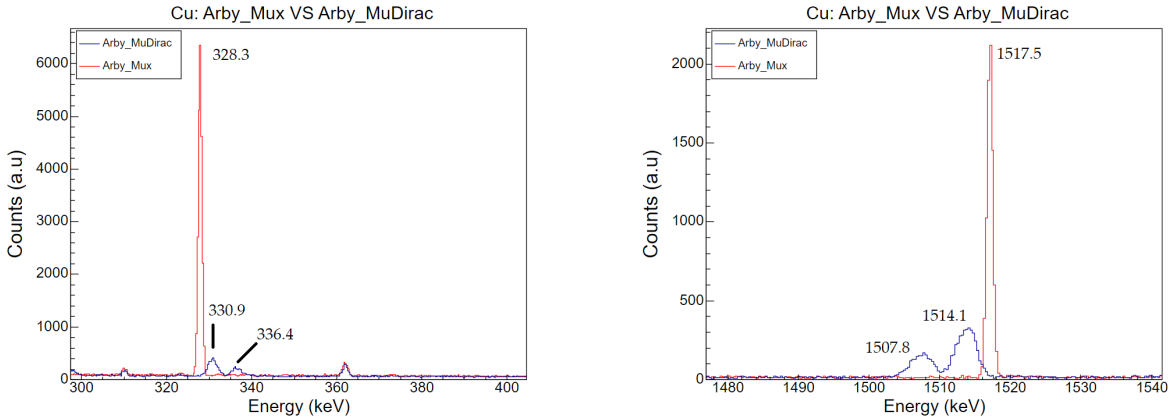

(a) **(b)**

Figure 4.4: Comparison between ARBY/Mux and ARBY/MuDirac for copper. In the Arby version with the database (blue), the two signature copper K peaks are modelled, differently from the previous version (red).

Simulation of a negative muon X-ray spectra

To finally evaluate the capabilities of the ARBY/MuDirac version, simulations were compared to a standard measurement performed at ISIS. The instrument setup of a negative muon experiment was modelled in ARBY with a sample consisting of a thin foil of a given material, placed 10 cm from the beam exit. Testing was done for a set of elements, and here results for silicon are reported. As shown in Figure 4.5a, intensities of the simulated spectra (red) are not well reproduced. Even though the patterns are similar between the two spectra, in the simulated spectrum, silicon K transition intensities are much higher than the M transitions, a relationship inverted in the measured spectra. This is because MuDirac assumes that all states can be starting points of a transition, without considering their differences in probability of being populated [4]. Therefore, since the intensity is related to the population of the starting decay level, the computed intensities are not properly correct. For now, they are just based on the probability of a transition to take place. In addition, the simulations do not consider the efficiency of the detection system. MuDirac developers are working towards a solution to the issue and a MuDirac 2.0 version is expected soon. For the moment, to try and tackle the problem, a solution could be provided by scaling the calculated intensities using a measured spectrum. A normalization factor for each peak was obtained by dividing the normalised peak area of the measured spectrum by the normalised peak area of the simulated spectrum. The MuDirac intensities, particularly, were scaled with a constraint: the maximum value, instead of being the 400 keV peak, was set to be the 76 keV peak, which is the most intense peak in the measured spectrum. Results of the scaled data are reported in Figure 4.5b: with this approach, peaks are better modelled, especially in the high energy range. The results of the work are promising and show that a better

agreement with the literature data is reached when using the ARBY/MuDirac version. Still, the software presents some drawbacks, especially in cases of calculated intensities that are not well reproduced. However, MuDirac is an open-source software and is in continuous development, and new and implemented software is also in development. This means that the database can be kept updated as the software improves. Finally, the solution proposed in this work, as done with other databases, could be directly implemented into GEANT4. This would require adding an alternative class to the G4EmCaptureCascade class, as well as other extra classes to handle the database.

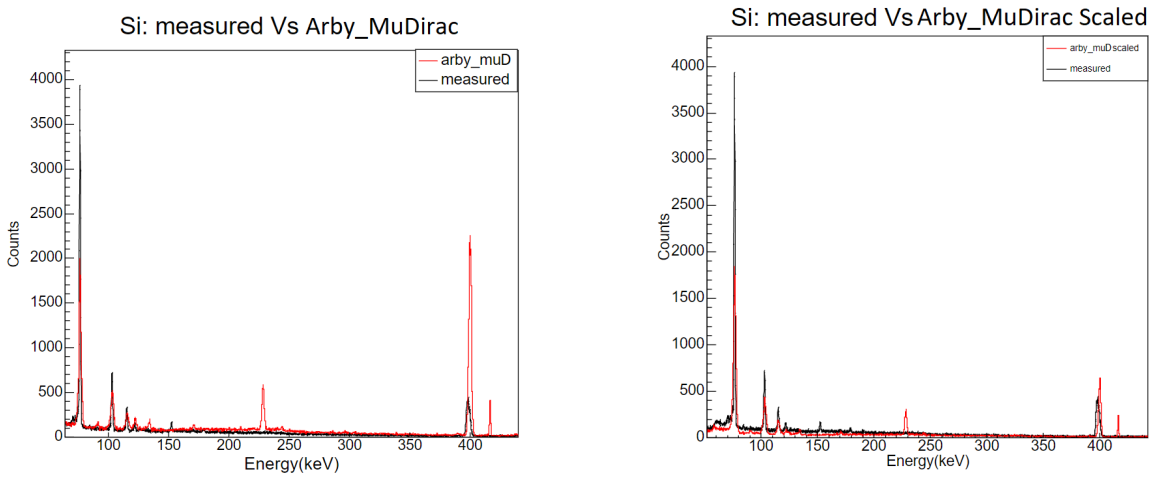

(a) **(b)**

Figure 4.5: Comparison between real measured data of Silicon (black) and the simulations with ARBY/MuDirac (a) and ARBY/MuDirac (b) with scaled peak intensities. Differences are evident in the 76 keV peak at the beginning of the spectra and the 400 keV peak. In the real measurement, the first is more intense than the second, the opposite of the results of the simulation. After scaling, the intensities are reproduced better. The extra peaks present in the simulated spectrum could be due to the other material present in the modelled environment (230 keV) or to error in the simulation process (at 416 keV, for example, the peak is too sharp and narrow to be considered part of the cascade).

Table 4.1: Corresponding peak values for the principal transitions in literature and from GEANT4 simulations (unit: keV). Literature data were taken from [11, 12]

GEANT4 VS Literature

Transition	K_α ($2p_{3/2\ -\ 1/2}$- $1s_{1/2}$)			K_β ($3p_{3/2\ -\ 1/2}$ -$1s_{1/2}$)			L_α ($3d_{5/2\ -\ 3/2}$-$2p_{1/2}$)			M_α ($4f_{7/2\ -\ 1/2}$- $3d_{5/2}$)		
Element	Lit.	Sim.	Δ	Lit.	Sim.	Δ	Lit.	Sim.	Δ	Lit.	Sim.	Δ
^{13}Al	346.9	335.2	11.7	413.0	400.9	12.1	66.1	66.3	-0.2	21.8	23.6	-1.8
^{14}Si	400.2	386.8	13.4	476.7	462.9	13.8	76.6	76.8	-0.2	26.9	27.2	-0.3
^{26}Fe	1253.7	1234.2	-19.5	1257.2	1276.8	-19.6	265.7	264.1	1.6	92.6	92.8	-0.2
^{29}Cu	1506.6	1491.3	15.3	1512.8	1500.2	12.6	330.3	328.3	2.0	115.9	115.2	0.7
^{47}Ag	3140.6	3151.8	-11.2	3177.7	-	-	869.2	862.4	6.8	304.8	302.2	2.6
^{79}Au	5594.9	5518.4	76.5	5764.9	5732.5	32.4	2341.2	2338.4	2.8	870.0	880.1	-10.1
^{82}Pb	5780.1	5674.4	105.7	5966.3	-	-	2500.3	2499.5	0.8	938.4	936.8	1.6

Table 4.2: Comparison between literature and ARBYMUX simulations. Literature data were taken from [11, 12]

ARBYMux VS Literature

Transition	K_α ($2p_{3/2\ -\ 1/2}$- $1s_{1/2}$)			K_β ($3p_{3/2\ -\ 1/2}$-$1s_{1/2}$)			L_α ($3d_{5/2\ -\ 3/2}$-$2p_{1/2}$)			M_α ($4f_{7/2\ -\ 1/2}$- $3d_{5/2}$)		
Element	Lit.	Sim.	Δ	Lit.	Sim.	Δ	Lit.	Sim.	Δ	Lit.	Sim.	Δ
^{13}Al	346.9	346.7	0.2	413.0	413.7	-0.7	66.1	66.3	-0.2	21.8	23.6	-1.8
^{14}Si	400.2	401.4	-1.3	476.7	476.7	0.0	76.6	76.8	-0.2	26.9	27.2	-0.3
^{26}Fe	1253.7	-	-	1257.2	1260.5	-3.3	265.7	264.1	1.6	92.6	92.8	-0.2
^{29}Cu	1506.6	-	-	1512.8	1517.5	-4.7	330.3	328.3	2.0	115.9	115.2	0.7
^{47}Ag	3140.6	-	-	3177.7	3197.4	-19.7	869.2	862.4	6.8	304.8	302.2	2.6
^{79}Au	5594.9	-	-	5764.9	5696.7	68.2	2341.2	2338.4	2.8	870.0	880.1	-10.1
^{82}Pb	5780.1	-	-	5966.3	5892.3	74.0	2500.3	2499.5	0.8	938.4	936.8	1.6

Table 4.3: Comparison between literature and ARBYMuDirac simulations (unit: keV). Here, delta energy is lower than two keV with the only exception of lead K_β, which is slightly larger. This is due to the fact that literature value is for natural lead, whereas the simulated one is from ^{208}Pb. Literature data were taken from[11, 12]

ARBYMuDirac VS Literature

Transition	K_α ($2p_{3/2\ -\ 1/2}$- $1s_{1/2}$)			K_β ($3p_{3/2\ -\ 1/2}$-$1s_{1/2}$)			L_α ($3d_{5/2\ -\ 3/2}$-$2p_{1/2}$)			M_α ($4f_{7/2\ -\ 1/2}$- $3d_{5/2}$)		
Element	Lit.	Sim.	Δ	Lit.	Sim.	Δ	Lit.	Sim.	Δ	Lit.	Sim.	Δ
^{13}Al	346.9	346.9	0.0	413.0	412.9	-0.1	66.1	66.1	0.0	21.8	23.1	-1.3
^{14}Si	400.2	400.9	-0.8	476.7	477.2	-0.5	76.6	76.4	0.5	26.9	26.8	0.1
^{26}Fe	1253.7	1252.6	1.1	1257.2	1256.8	0.4	265.7	265.8	-0.1	92.6	92.4	0.2
^{29}Cu	1506.6	1507.8	-1.2	1512.8	1514.1	-1.3	330.3	330.9	-0.6	115.9	115.26	0.3
^{47}Ag	3140.6	3139.8	0.8	3177.7	3176.9	1.9	869.2	868.9	0.3	304.8	303.1	1.7
^{79}Au	5594.9	5593.6	1.3	5764.9	5763.0	1.9	2341.2	2339.9	1.3	870.0	869.8	0.2
^{82}Pb	5780.1	5779.3	0.8	5966.3	5963.9	2.4	2500.3	2500.0	0.3	938.4	937.9	0.5

4.3 Validation of γ and X-ray transportation

The reliability of GEANT4/ARBY software is important not only for the muon interaction process but also for the transportation of γ-rays. For a negative muon experiment, indeed, it is useful to have efficiency curves for each detector, that may change depending on the instrument setup. Making an efficiency curve, however, could be time-consuming, especially if the time window of an experiment is brief. Thus, a validated simulation software could provide useful help for the evaluation of detection efficiency: once implemented in the software, measurements could always be simulated, rather than performed with active sources [13, 14]. At the University of Milano Bicocca, ARBY has been already used for the simulation of HPGe detectors in many different experiments [15–18]. The most critical part is the modelling of the detectors in the simulation software. The principal characteristics of a detector are listed in the datasheet, where the dimensions of the crystal and the dead layers are reported. However, this documentation is not always reliable: firstly because it is difficult for manufacturers to assess the actual size of the dead layers; secondly, detectors ageing and temperature cycles cause an increase in the thickness of these layers, with the diffusion of lithium in the substrate and with a following reduction of the active area [19, 20]. Combined, these two issues result in a simulated efficiency that is, in most cases, different from the measured one. Therefore, the modelling of the crystal and its dead layers represents a complicated task. As reported in the following paragraph, to find the best fit between simulation and measurement, parameters had to be changed for most of the detectors described. To make the task more difficult, datasheets do not always provide all the information needed for the construction of detectors, so some parameters have to be supposed. Upon the construction of the detector in the software, a measurement with active sources has to be made. The measurement, in addition, could provide a source of error in the simulation, so it is important to have a precise knowledge of the source characteristics, as well as an accurate measurement of the source-to-detector distance. As the detectors, the source is modelled in ARBY, to fully replicate the real measurement. To further validate ARBY, the HPGe detectors of the 2i01 laboratory of the University of Milano Bicocca have been modelled in the software (main characteristics are reported in table 4.4). For each detector, the work consisted of:

- Acquisition with reference sources at a known distance
- Modelling of the detector in GEANT4/ARBY
- Simulation and data analysis
- Comparison with real measurement

Table 4.4: Principal parameters of Lab2i01 germanium detectors. Data were taken from datasheets.

Detector	Crystal size (mm)	Front dead layer (µm)	Lateral dead layer (µm)	Bottom dead layer (µm)	Front window (mm)
BEGe	40.25X31.3	0.4	600	600	0.6 (Carbon Epoxy)
GEM-S	15.2X20.8	10	700	0.3	0.9 (Carbon Epoxy)
GLP	5X7	0.3	-	600	0.13 (Beryllium)

4.3.1 Methods

For lab 2i01 detectors, the source of the mixed radionuclides was carefully placed in front of the detector endcap, at zero distance (with the 20- 1836 keV energy range covered). This was done to enhance the acquisition and to maximize the acquisition with rather low-emission sources. The sources, provided by Eckert & Ziegler, consisted of a radioactive material incorporated in a plastic layer of 10 mm in diameter and 0.2 mm thick. The plastic layer, moreover, is covered on each side by a 0.15 mm paper label and the assembly is further sealed between 0.125 mm thick plastic foils. Finally, the foils are mounted in an aluminium ring, 54 mm in diameter and 3mm thick. The measured spectra were collected with the MAESTRO software and analysed with the TASSO, a software developed by Oliviero Cremonesi for Gaussian fitting of the peaks [21]. Each measurement was stopped whenever a good statistic was reached in the peaks, namely a $< 1\%$ statistic error.

For each peak, the absolute full-energy peak efficiency was calculated according to the following equation

$$\varepsilon = \frac{N(E)}{A\rho t} \tag{4.1}$$

Where *N(E)* is the net peak area at a given energy, A is the activity of the source at measurement time, ρ is the branching ratio (i.e the emission probability) of the γ-ray and t is the measuring time. The activity of the source was obtained from the initial activity reported on the data sheet of the source. Finally, the efficiency calibration curve was fitted to a polynomial function [22]:

$$\varepsilon(E) = \frac{P_1 + P_2 ln(E) + P_3 ln(E)^2 + P_4 ln(E)^3 + P_5 ln(E)^4}{E} \tag{4.2}$$

where $\varepsilon(E)$ is the full energy peak efficiency, E is the energy of the γ-ray and P_1 - P_5 are the fitted parameters of the function. From the known fitted parameters, efficiency at specific energies can be calculated. In the following paragraph, the results of the lab 2i01 of the University of Milano Bicocca detectors will be reported.

Broad Energy germanium detecor

Broad Energy germanium (BEGe) are very powerful detectors that can cover a wide energy range, from 3 keV up to 3 MeV according to the manufacturer, with an excellent resolution. In 2i01 laboratory of the University, the BEGe 5030 is a high-purity germanium crystal cooled by a cryocooler (specifics are ported in table 4.4. The crystal shape, flat and non-bulletized offers optimum efficiencies for samples counted close to the detector. To evaluate detector efficiency and reproduce the measurement in the simulation software, the γ source described previously was placed on top of the carbon fibre window of the detectors, as shown in Figure 4.6. Another big advantage of the BEGe is that the detector dimensions are virtually the same on a model-by-model basis.

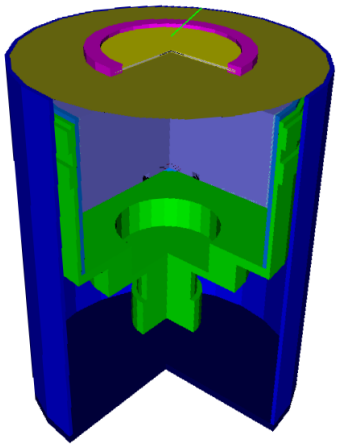

Figure 4.6: Section of the BEGe detector modelled in ARBY: here, the source was placed directly on the carbon epoxy endcap. The active area is contained in the green holder

Results of the simulations show a remarkably good agreement with the measured data, as reported in Figure 4.7. For this detector, the best agreement was reached without changing any parameters of the data sheet file, meaning that the manufacturer's description was correct. To add information to the modelling, single γ energies were simulated and a more populated curve was fitted with the above-mentioned polynomial.

ORTEC coaxial detector (GEM series)

ORTEC GEM radiation detectors are P-type coaxial HPGe designed to address the typical energy range that goes from 40 keV and upwards. The crystal characteristics are reported in table 4.4. This detector is cooled down via liquid nitrogen. Unlikely the BEGe with the values taken from the data sheet, the simulated measurement presented strong discrepancies with the measured values, as shown in Figure 4.8. In particular, the simulation had more

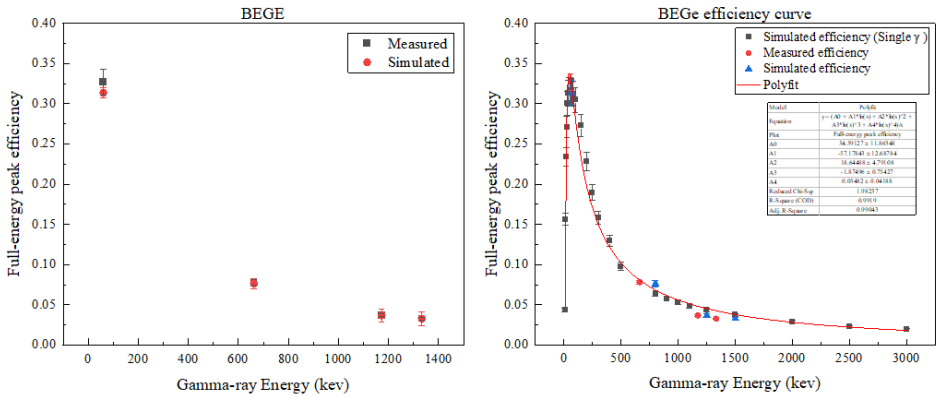

Figure 4.7: Results of the implementation of the BEGe detector in ARBY. In a, the agreement between the simulation and the measurement is shown. In b, to add more points to the calibration curve, simulations of single γ-rays were performed the good. The resulting data were fitted with equation 4.2.

count in the photopeak, meaning an increased overall efficiency, which could be due to too thin dead layers.

To find the best fit, the front and lateral dead layers were modified, as well as the bullet radius. The latter is information that is not usually provided by manufacturers, but it can have an important influence on efficiency. The germanium crystal, indeed, is shaped like a bullet to remove weak-field regions in the corners of the front edge of the crystal that would degrade the detector performance. Here, the best value was found to be 3 mm (Figure 4.9 a). The information about the dead layers, instead, is a difficult assessment for the manufacturer, and in most cases has to be modified. Therefore, to improve the simulations at the low energy range, the front dead layer was modified and combined with an increase of the lateral dead layer, and a good agreement was reached for all the simulated energies, with discrepancies lower than 5%. In other examples found in the literature, it was found that the nominal lateral dead layer value had to be doubled to meet the measured efficiencies (cheek) [22]. With a doubled later dead layer, indeed, a significant improvement in the efficiency was reached, especially with the high energy efficiency. In the end, the best values of the active germanium resulted to be a bullet radius of 3 mm, a lateral dead layer of 1.5 mm and a front dead layer of 7 µm.

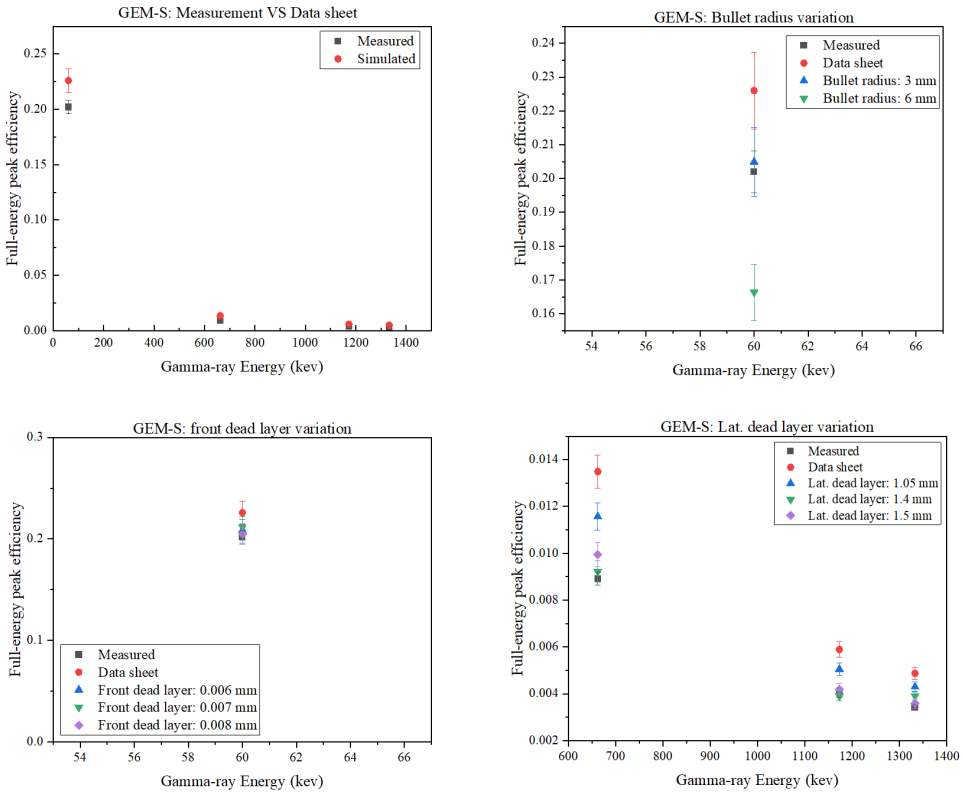

Figure 4.8: For the GEMS, differently from the BEGe, discrepancies between simulation and measurement were more pronounced (a). To find the best fit, the radius of the bullettization, and the front and lateral dead layer were modified (b,c,d).

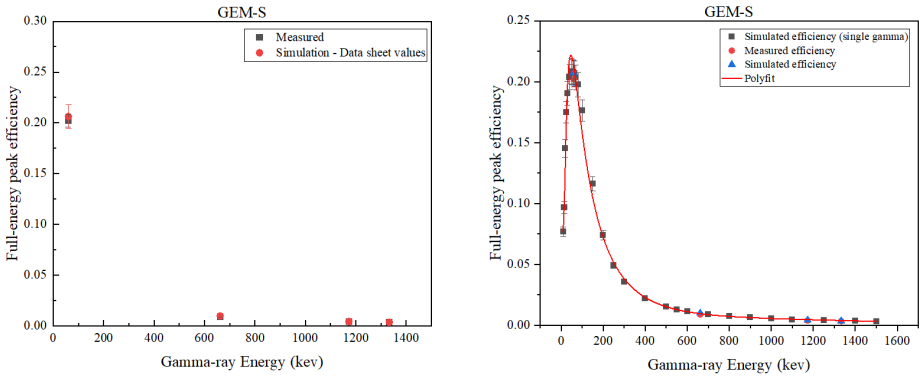

Figure 4.9: Results of the implementation of the GEMS detector in ARBY. In a, the agreement between the simulation and the measurement is shown. In b, as for the BEGe, to add more points to the calibration curve, simulations of single γ-rays were performed the good.

ORTEC Planar detector (GLP series)

The ORTEC GLP is a small-area high-purity P-type germanium detector with excellent energy resolution in the 3 to 300 keV range. The crystal of lab 2i01 is 10x7 mm with a 0.3 µm front dead layer and a 0.06 mm back dead layer. Given the limited energy range, measurements were performed with just one active source and the peaks from americium, caesium and cadmium were used for the efficiency curve. As before, the detector was implemented in ARBY and simulations were performed. It has to be stated that this detector has been refurbished, so the datasheet parameters could be different from the real values. Indeed, the first set of simulations resulted in a big discrepancy with the measured values, especially for the americium and caesium peaks. With a higher peak efficiency in the simulated peaks, considerations about the size of the dead layers were made. Before changing the parameters, however, there was the opportunity to perform an X-ray tomography of the detector. Hence, the pop-top end of the device was removed and brought to SmartNDT, a small company outside Milan. A slice of the tomography is reported in Figure 4.10.

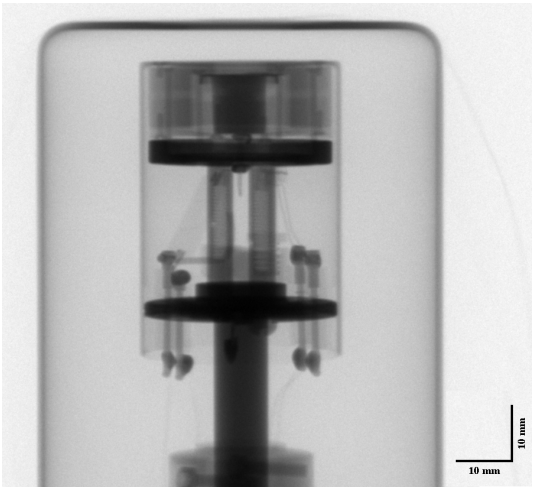

Figure 4.10: X-ray projection of the GLP detector. The Ge crystal is the cylinder just above the endcap: this projection was fundamental to have more precise information about the crystal size. The image was processed with the ImageJ software, which allows the user to perform a pixel-to-mm calibration and obtain size information about the investigated sample [23].

The slice was used to get information about the size of the crystal, which resulted to be 10.4 ± 0.1 mm in height and 9.4 ± 0.2 mm in diameter. This means that the datasheet values, as mentioned, were not correct. Thus, the overall volume of the crystal is increased and the simulation with the new crystal parameters resulted in a bigger discrepancy than the first set of simulations, as shown in Figure 4.11a. Therefore, in this case, dead layers play a prominent role.

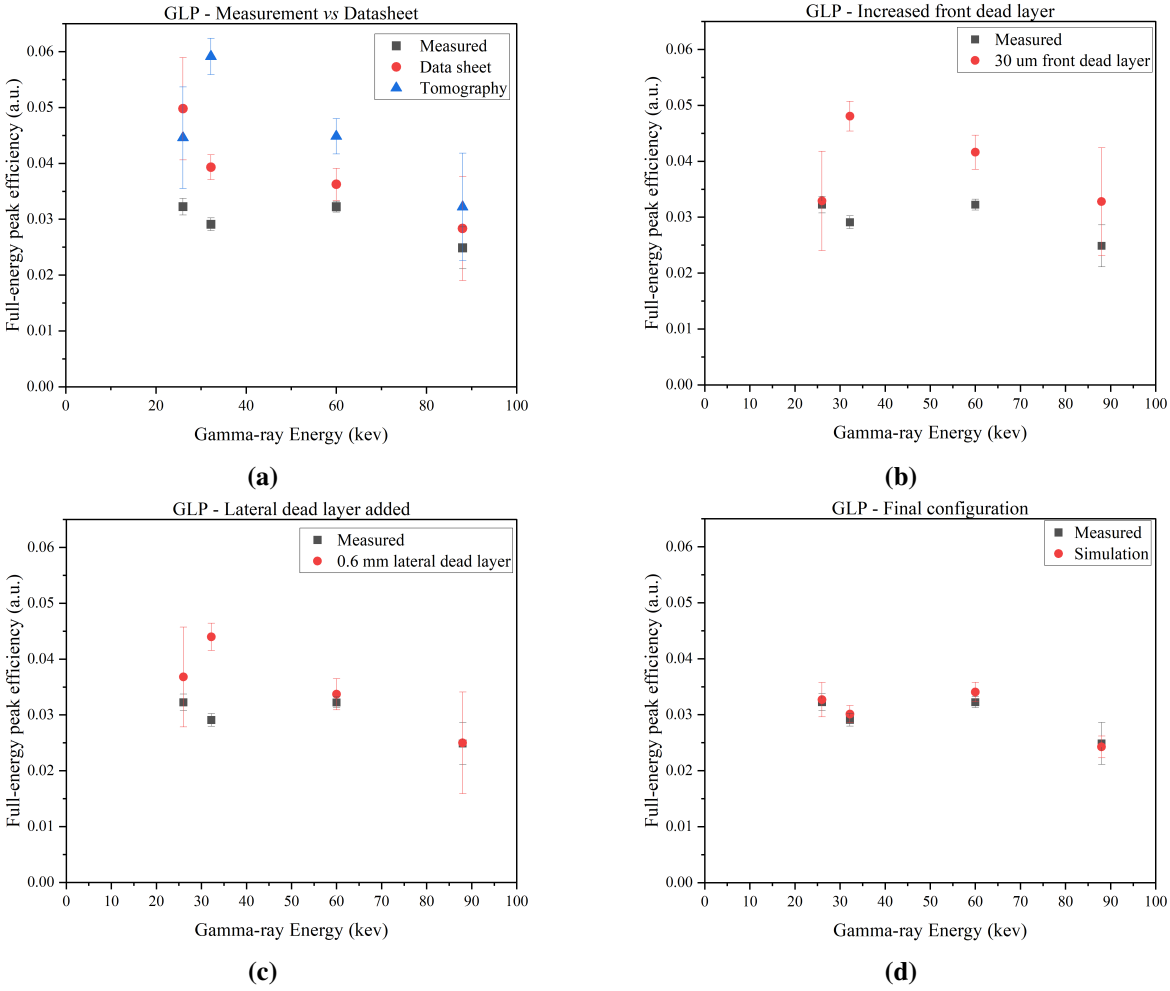

Figure 4.11: For the GLP detectors, the simulated results presented high discrepancies compared with the measurements (a). An increase in the front and lateral dead layer (b,c) produced a better agreement and the final results are reported in d, where the front dead layer was set to 30 µm, while the lateral and bottom one to 600 µm.

To improve the simulation output the front dead layer was increased first. A good agreement was reached with a 30 µm layer, especially for the 26 keV americium peak (Fig. 4.11b), but a big discrepancy was still present for the caesium peak. This was solved by increasing the number of events. Since the increase of the front and bottom dead layer (and contextually the decrease of the active volume) did not provide the expected results, a later dead layer of the size of the bottom dead layer was introduced (600 µm), providing a better agreement for the americium and cadmium peak, as shown in Figure 4.11c. The final result is reported in Figure 4.11d, where events were increased and a good agreement was reached. In this final configuration, the front dead layer was set to 30 µm, while the lateral and bottom dead layers to 600 µm each. The implementation of the GLP in ARBY had some complica-

tions that were partly solved by the radiography, which provided a better characterization of the real size of the crystal. The radiography, however, did not provide any information about the dead layers, which were adjusted starting from the values reported on the datasheet. In conclusion, even if the information provided by the datasheet were not complete enough, with the adjustment of the parameters, a good agreement was reached.

Bibliography

[1] Alfredo Ferrari et al. “FLUKA: A multi-particle transport code (Program version 2005)”. In: (July 2005). DOI: 10.2172/877507.

[2] C.J Werner. *MCNP User Manual . Code Versione 6.2*. 2017.

[3] S. Agostinelli et al. “Geant4—a simulation toolkit”. In: *Nucl. Instrum. Methods Phys. Res. A* 506.3 (2003), pp. 250–303.

[4] Simone Sturniolo and Adrian Hillier. “Mudirac: A Dirac equation solver for elemental analysis with muonic X-rays”. In: *X-Ray Spectrometry* (June 2020), pp. 1–17. ISSN: 10974539. DOI: 10.1002/xrs.3212.

[5] Simone Sturniolo. *https://github.com/muon-spectroscopy-computational-project/mudirac*. 2020.

[6] James F. Ziegler, M. D. Ziegler, and J. P. Biersack. “SRIM – The stopping and range of ions in matter (2010)”. In: *Nuclear Instruments and Methods in Physics Research Section B: Beam Interactions with Materials and Atoms* 268 (11-12 June 2010), pp. 1818–1823. DOI: 10.1016/J.NIMB.2010.02.091.

[7] Vladimir Ivanchenko. *https://geant4.kek.jp/lxr/source/processes/hadronic /stopping/src/G4EmCaptureCascade.cc*. 2012.

[8] C Pizzolotto et al. “The FAMU experiment: muonic hydrogen high precision spectroscopy studies”. In: *The European Physical Journal A* 56 (7 2020), p. 185. ISSN: 1434-601X. DOI: 10.1140/epja/s10050-020-00195-9.

[9] S Guatelli et al. “Geant4 Atomic Relaxation”. In: *Nuclear Science, IEEE Transactions on* 54 (July 2007), pp. 585–593. DOI: 10.1109/TNS.2007.896214.

[10] Samer Bakr et al. “Geant4 X-ray fluorescence with updated libraries”. In: *Nuclear Instruments and Methods in Physics Research Section B: Beam Interactions with Materials and Atoms* 507 (2021), pp. 11–19. ISSN: 0168-583X. DOI: https://doi.org/10.1016/j.nimb.2021.09.009.

[11] R. Engfer et al. “Charge-distribution parameters, isotope shifts, isomer shifts, and magnetic hyperfine constanst from muonic atoms”. In: *Atomic Data and Nuclear Data Tables* 14 (1974), pp. 509–597.

[12] D. R. Zinatulina. "Electronic Catalogue of Mesoroentgen Spectra". In: *Physics of Atomic Nuclei* 82 (3 2019). DOI: 10.1134/S1063778819030165.

[13] François Bochud et al. "Simple Monte-Carlo method to calibrate well-type HPGe detectors". In: *Nuclear Instruments and Methods in Physics Research, Section A: Accelerators, Spectrometers, Detectors and Associated Equipment* 569 (3 Dec. 2006), pp. 790–795. DOI: 10.1016/j.nima.2006.09.040.

[14] José Ródenas et al. "Application of the Monte Carlo method to the analysis of measurement geometries for the calibration of a HP Ge detector in an environmental radioactivity laboratory". In: *Nuclear Instruments and Methods in Physics Research, Section B: Beam Interactions with Materials and Atoms* 263 (1 SPEC. ISS. 2007), pp. 144–148. DOI: 10.1016/j.nimb.2007.04.210.

[15] C Alduino et al. "The projected background for the CUORE experiment". In: *The European Physical Journal C* 77 (8 2017), p. 543. ISSN: 1434-6052. DOI: 10.1140/epjc/s10052-017-5080-6.

[16] C. Alduino et al. "Measurement of the two-neutrino double-beta decay half-life of 130 Te with the CUORE-0 experiment". In: *European Physical Journal C* 77 (1 Jan. 2017). ISSN: 14346052. DOI: 10.1140/epjc/s10052-016-4498-6.

[17] D. Q. Adams et al. "Search for Majorana neutrinos exploiting millikelvin cryogenics with CUORE". In: *Nature* 604 (7904 Apr. 2022), pp. 53–58. ISSN: 14764687. DOI: 10.1038/s41586-022-04497-4.

[18] C. Alduino et al. "Measurement of the two-neutrino double-beta decay half-life of 130 Te with the CUORE-0 experiment". In: *European Physical Journal C* 77 (1 Jan. 2017). ISSN: 14346052. DOI: 10.1140/epjc/s10052-016-4498-6.

[19] A Pascual et al. *Analysis of the influence of germanium dead layer on detector calibration simulation for environmental radioactive samples using the Monte Carlo method*. 2003.

[20] Ahmed Azbouche, Mohamed Belamri, and Théophile Tchakoua. "Study of the germanium dead layer influence on HP(Ge) detector efficiency by Monte Carlo simulation". In: *Radiation Detection Technology and Methods* 2 (2 Nov. 2018). DOI: 10.1007/s41605-018-0074-y.

[21] M. Clemenza et al. "Measurement of airborne 131I, 134Cs and 137Cs due to the Fukushima reactor incident in Milan (Italy)". In: *Journal of Environmental Radioactivity* 114 (Dec. 2012), pp. 113–118. DOI: 10.1016/j.jenvrad.2011.12.012.

[22] I. A. Alnour et al. "New approach for calibration the efficiency of HpGe detectors". In: vol. 1584. American Institute of Physics Inc., 2014, pp. 38–44. DOI: 10.1063/1.4866101.

[23] Johannes Schindelin et al. “Fiji: an open-source platform for biological-image analysis”. In: *Nature Methods* 9 (7 2012), pp. 676–682. DOI: 10.1038/nmeth.2019. URL: https://doi.org/10.1038/nmeth.2019.

Chapter 5

Simulations tools for data interpretation

As described in the introduction of this work, one of the main features of negative muon spectroscopy is the capability of evaluating the elemental composition as a function of depth. Known as ”depth profiling”, this method is already performed in heritage science with techniques like RBS, XPS, and Tof-SIMS and provides important information for the characterization of materials, especially paintings [1, 2]. With metal objects, however, where patinas and coating can be in the order of the micron scale, the limited penetration depth (and the necessity of sample preparation) of these methods represents an important issue. μ - XES, though, could provide a real breakthrough in the depth profiling of metallic artefacts: thanks to the high penetration depth of the muon beam and the high energy of the emitted radiation, it is possible to probe beneath the surface of a material to get detailed information about the bulk. Nonetheless, by varying the incident momentum of the muon beam, it is possible to perform a scan of the material, thus providing complete information about the variation of the composition as a function of depth. This characteristic makes μ - XES a unique method among the Heritage science community. Still, the technique is relatively new and a lot of effort is required for the interpretation of the collected data. This work, indeed, proposes the use of Monte Carlo simulation to improve the understanding of data, especially when using muons for the characterization of thin layers. In particular, the focus of this chapter is the assessment of the thin layer of gold used by Renaissance craftsmen to cover copper-based alloys.

5.1 Depth profiling with SRIM-TRIM and GEANT4-ARBY

Simulations software represents an invaluable tool for the improvement of data interpretation. In these software, the user can reproduce the experimental setup and simulate the interaction of a probe of particles with a well-defined sample: by tuning the parameter of the simulation, a result that fits the experimental data can be obtained. Monte Carlo sim-

ulations, in particular, are already used in XRF, where a comparative approach is used to compare the measured and the simulated spectra [3–6]. A similar method could be applied to negative muon data analysis, but, as stated in the previous chapter, the GEANT4 tool is not reliable enough to produce an X-ray spectrum that can be used for comparison. However, SRIM-TRIM and GEANT4 simulations provide an alternative tool that can be used for data analysis. SRIM (Stopping and Range of Ions in Matter) and TRIM (Transport of Ions in Matter) are a collection of software packages for the simulation of the interaction of energetic ions with matter [7]. With SRIM it is possible to simulate the stopping power of ions in material, providing information about the energy loss and the ion ranges. For instance, in negative muon data analysis, SRIM is used to calculate the a parameter in the following relation:

$$R = ap^{3.5} \tag{5.1}$$

where a is defined as the range of the muon in a material at a defined momentum p. TRIM, instead, is a SRIM extension that simulates the trajectory of the ion in a material, providing information about the ion's path by including contributions from many physical processes. TRIM, as GEANT4/ARBY, stores the information about the number of muons stopped in the material. With a layered sample, both software provide the number of muons stopped in each layer, a number that can be used for comparison with the experimental data. In particular, given that each muon stopped in a layer will most likely generate a radiative emission that will contribute to the peak intensity, the simulated number of stopped muons can be directly compared to the variation of a peak intensity along the depth. Peak intensities, indeed, will vary during a momentum scan and the same process can be replicated in simulation software. Upon normalization, the two outputs can be compared and used for assessing the thickness of the layers present in a given sample. In TRIM, the user interface allows the insertion of mono or multi-layered samples by selecting from a database of known materials or by creating each layer from scratch. Here, the interaction of a muon beam with the material is done by using a hydrogen ion with one-ninth of its mass. Even if the muon particle is not implemented in the software, this stratagem allows to have results comparable to the experimental ones. The result of the interaction is a percentage of stopped muons in each layer. TRIM, indeed, has already been used for performing negative muon simulations, as reported in [8, 9]. Figure 5.1, shows the output of a TRIM simulation of a multi-layered sample, with the stopping profile of the beam at different momentum.

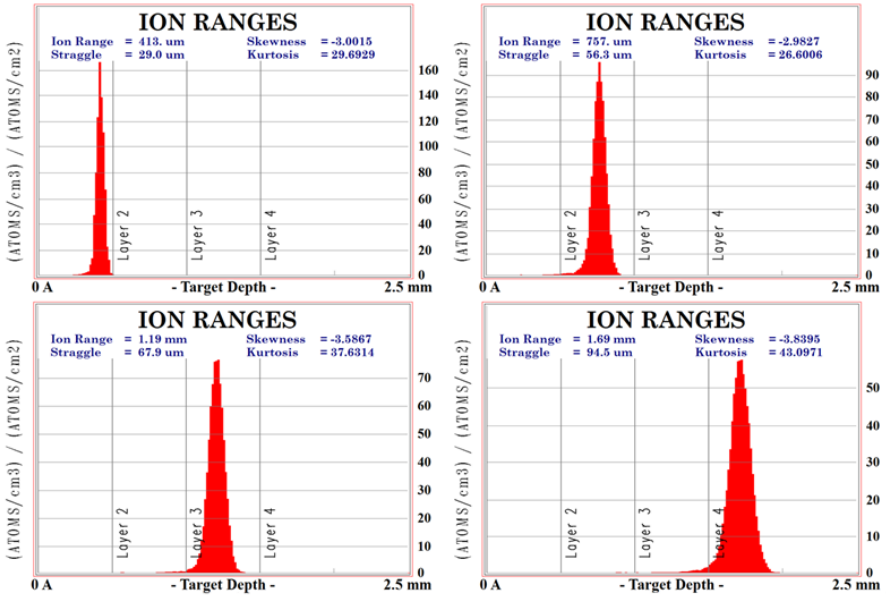

Figure 5.1: An example of TRIM simulation of a multilayered sample. The beam momentum was increased to selectively penetrate in each layer, providing a stopping profile and a number of muons stopped in each layer

TRIM provides a quick and easy tool for simulating the interaction of muons with matter. However, some drawbacks need to be addressed. When performing a TRIM simulation, it is better to work with thin layers to have better results. For example, the 10 cm distance that divides the Mylar window at the beam exit and the sample position at RIKEN port4, has to be squeezed down to a 0.1 mm layer, with an increased density of air of a factor of 10^3. This enables the simulation to work quicker and better than using a 10 cm layer. With a large air gap, the beam diverges and it is not possible to well reproduce experimental measurements. In addition, in TRIM the user can implement only single layers and not the entire sample geometry, precluding the use of the tool for complicated samples and uneven surfaces.
On this issue, the GEANT4/ARBY tool can provide a new and improved solution to the characterization of more complex samples. As TRIM, ARBY can provide information regarding the number of stopped muons in each layer. But differently from TRIM, with ARBY the user can employ all the tools provided by GEANT4 to model a negative muon experiment: from the instrument setup to the sample, all geometries can be modelled. Here, the user is required to store all the geometrical information in a configuration file that is then used to launch the simulation, as reported in Chapter 3. Furthermore, one could also use laser scanning to implement the exact material geometry in the software, but this is not yet implemented in ARBY [10]. ARBY provides a more complete environment compared to TRIM (starting from the muon particle), without the necessity of squeezing layers. Finally, an ARBY simulation provides two types of results: an X-ray spectrum, not used for the rea-

sons mentioned above, and the number of stopped muons in each layer. This information is stored in a sub-folder (called "StopVol") contained in the root output file and accessible via the ROOT software. Since its development at Milano Bicocca, ARBY has never been used for depth profiling with negative muons. Thus, in this work, the simulations have been carried out both via SRIM-TRIM and Geant4/ARBY to validate the capabilities of the latter. Figure 5.2 reports an example of the application of the two software with a mockup sample. Here, the normalised number of stopped muons is plotted against the increasing momentum. The sample, composed of four layers of aluminium, copper, silver and gold (each layer of 20 µm thickness) provides a comparison between the two different outputs generated by the software. Both GEANT4/ARBY and Trim provide a well-defined depth profile of the sample. In particular, in TRIM the interpenetration of the beam in the adjacent layer seems to be more pronounced than in ARBY, where the FWHMs of the curves are thinner. This is because in TRIM a more pronounced effect of scattering of the muons produces an increase of the momentum spread compared to ARBY. It has to be stated that both simulations take into account the so-called "momentum bite" (or momentum spread, which at ISIS is generally of 4%), by generating a Gaussian beam profile. Thus, this difference in the plotted profiles can be attributed to diversities in the simulation process.

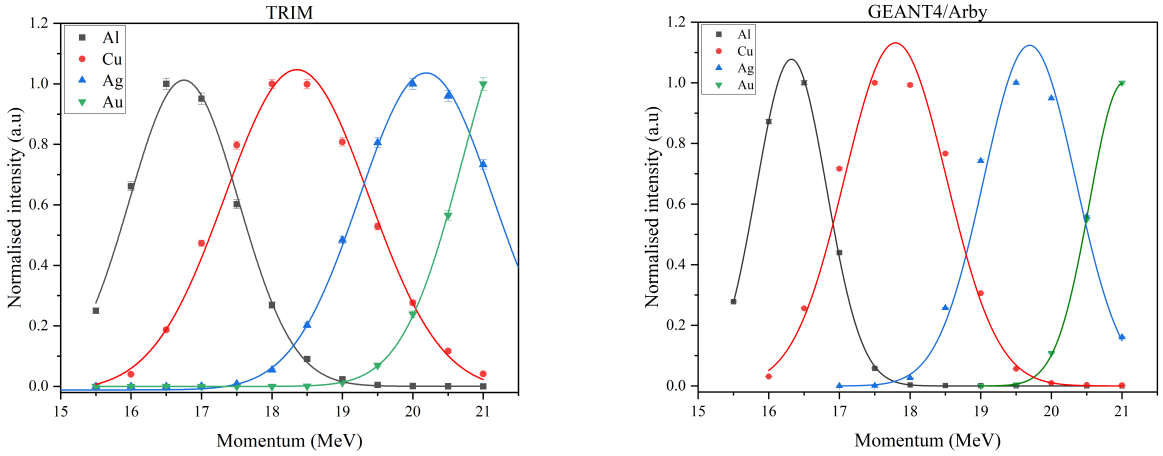

(a) **(b)**

Figure 5.2: Example of a depth profile of a mockup sample with TRIM (a) and GEANT4/ARBY (b). With a 4% momentum spread, the interpenetration of the beam in the layers in TRIM is more evident than in ARBY (b).

5.2 Characterization of gilded layers

5.2.1 The gilding process through the ages

The experiments reported in this work are devoted to the characterization of gilded copper alloys. Gold, not only gives an improved decorative effect but also improves the resistance to corrosion and ageing, thanks to its durability. Gilding, in particular, is the application of gold to the surface of a material. The first evidence of metal gilding dates back to the third millennium B.C., when metal objects were mechanically covered by gold foils (by folding, riveting or hammering). The evolution of this method was represented by gold leaf, a thin layer of gold attached to the substrate with adhesives, as already described by Pliny in his *Naturalis Historia* [11]. If the substrate was silver, gilding was performed by diffusion bonding: gold was burnished onto the hot silver surface, thus producing a strong metallurgical bond between the two metals. This method, however, was not suitable for copper alloys, since the oxidation of the surface prevented an efficient bonding. The solution came with amalgam gilding (also known as fire gilding or mercury gilding) introduced in China in the third century B.C. [12, 13]. Amalgam is an alloy of mercury and gold, mixed by adding small pieces of gold with mercury with a 1:8 ratio, as described by *Benvenuto Cellini* in his famous treats about goldsmithing and sculpture [14]. The mixture is heated up in a crucible, and when completely molten is rapidly cooled in water. The result is a paste about the consistency of butter, with an overall composition of 80-90% mercury and 10-20% gold. The paste is applied on the surface of the copper-based alloy and to let mercury evaporate, the surface is heated up to a temperature higher than the mercury boiling point. At this stage, the gilded layer has a porous structure caused by the evaporation of mercury. The last step is to burnish gold with a burnishing tool; as a result, a smooth, durable and shiny layer of gold with a thickness that ranges from a few to tens of microns is obtained [15]. This method was widely used around Europe until the 19^{th} Century when electroplating was introduced during the Industrial Revolution. Electroplating involves the use of water-based solutions, called ”galvanic baths” containing metal ions that will be deposited on a surface as metals. An anode and a cathode, which is the substrate where the deposition occurs, are immersed in a galvanic bath and an electric field is established between the two. This electric field forces the positively charged metal ions to migrate to the cathode, where they release their charge and deposit themselves as a metal layer. With this method, thin and durable metallic coatings can be produced for a variety of applications, from aerospace to jewellery [16].

5.2.2 Laboratory made samples

The characterization of gilded material started with a set of laboratory-made samples. These samples were prepared by electrodeposition at the Lotti Srl in Florence, a small factory that produces accessories for luxury bags and footwear. In particular, 3 brass foils of 7x5x0.1 cm were covered in gold, with increased thickness (Fig. 5.3. In addition to gold and brass,

the foils present an intermediate nickel layer. In a galvanic deposition, nickel is mostly used to prevent the degradation of the deposition. An intermediate layer of nickel, which is more durable and resistant to oxidation than copper, acts as a protective layer, avoiding the diffusion of copper in the precious metal coating. Thus, a "nickel flash", was done for each of the three foils. After the nickel flash, the foils were coated using a gold-iron bath working at 2 A/dm^2. The working parameters of the bath allow to have control over the deposition, even if for the micron scale, a good control is not guaranteed. For jewellery applications, indeed, coatings are in the range of the nanometer scale (generally less than a micron), so the production of a microns-thick gold layer requires some extra effort. For instance, the deposition of around three microns of gold required 1920 seconds.

(a) **(b)**

Figure 5.3: a) The measured sample is in the form of a 5x5 cm foil covered in gold, which was modelled in the ARBY software (b).

Once the foils were ready, they were sampled near the edge and embedded in resin to be analysed with SEM. The SEM scans were carried out at the Chemistry department of the University of Florence, which has a strong collaboration with the galvanic industries of the Florence basin. Figure 5.4 reports backscattered images of the three samples, whose characteristics are the following:

- Sample A. Average thickness: gold, 3.3± 0.2 µm;
- Sample B. Average thickness: gold, 4.6± 0.6 µm;
- Sample C; Average thickness: gold, 7.3± 0.8 µm;

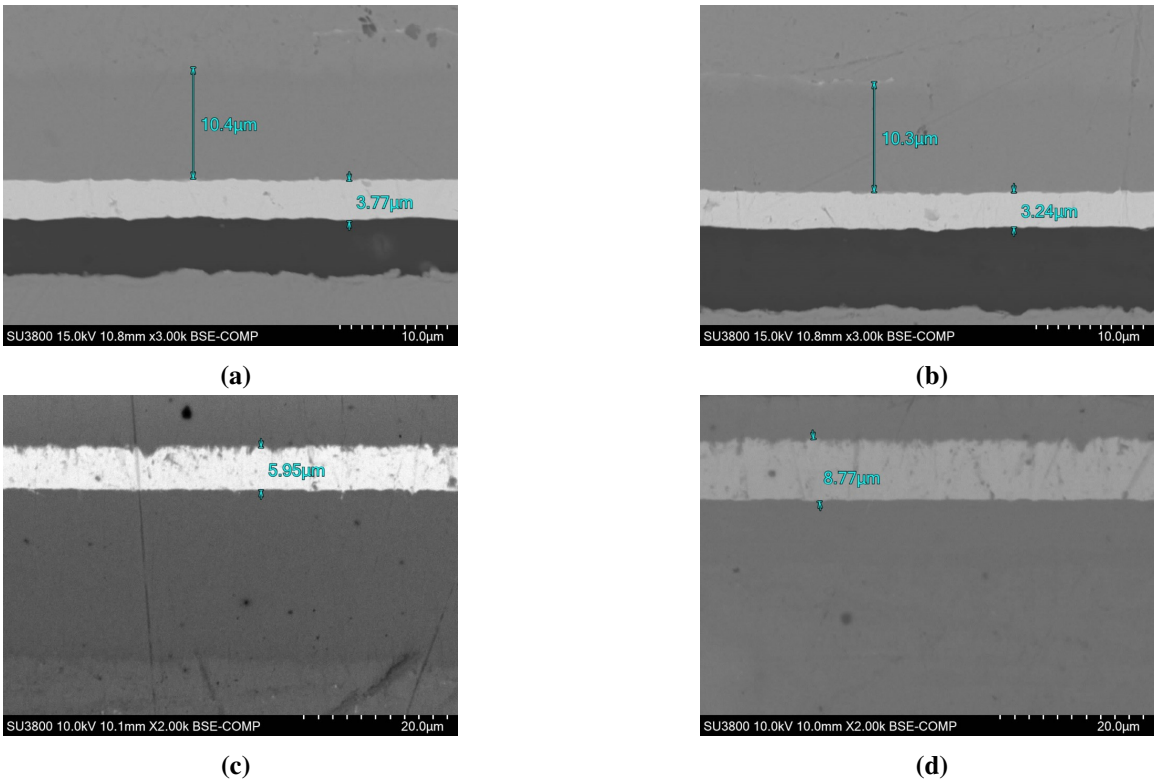

Figure 5.4: BSE images of the three foils, composed of a three-layered structure of brass, nickel and gold. The nickel flash is done in a less controlled bath, so the thickness is not as uniform as gold. For sample A (a,b) the average thickness of this layer is 8.7 ± 0.8 µm. (c): sample B; (d) sample C.

As mentioned, the control of the deposition process was not good enough to create a uniform layer of gold. However, the variation in thickness is generally lower than the muon's spatial resolution, which for gold is around one micron. Finally, the composition of the gold coating is reported in Figure 5.5. From the process, a 98.8 ± 0.2 % layer of gold was deposited on the nickel substrate.

Setting up the experiment

The three foils were measured at PORT4 during the 2023 September/October Cycle of the ISIS Neutron and Muon Source. The setup for the experiment consisted of three germanium detectors placed at 11 (Ge1), 10 (Ge3) and 8 (Ge4) cm from the sample position, as shown in Figure 5.6. The distance was varied to prevent the overloading of the detector electronics. The high energy upstream detector was missing from the setup due to the refurbishment of the vacuum system. Prior to the experiment, energy calibration was performed, following the process described in Chapter 2. The samples were wrapped in aluminium, which serves both as a sample holder and as an indication of the beam penetration depth. With aluminium on top, the sample becomes a four-layer foil, in which aluminium is used as a reference layer

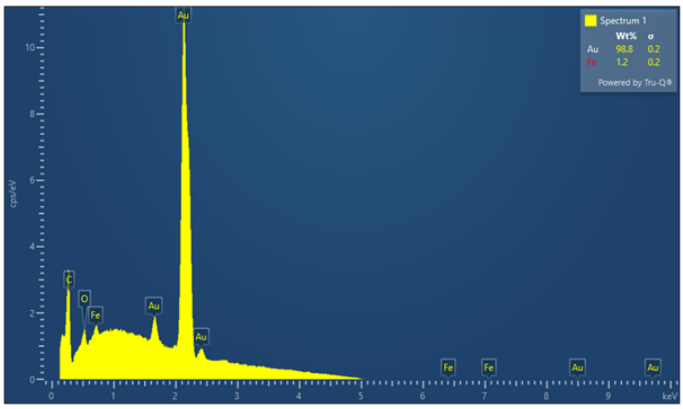

Figure 5.5: EDS scan of the gold layer. For the deposition, a gold-iron bath was used, which left a small percentage of iron that is below the μ - XES detection limit.

to evaluate the penetration of the beam. For each sample, a momentum scan was performed, starting from 15.5 MeV/c until 20 MeV/c. Momentum tuning for each step varied between 0.25 and 0.5 MeV/c. Momentum steps were decided based on results of preliminary results.

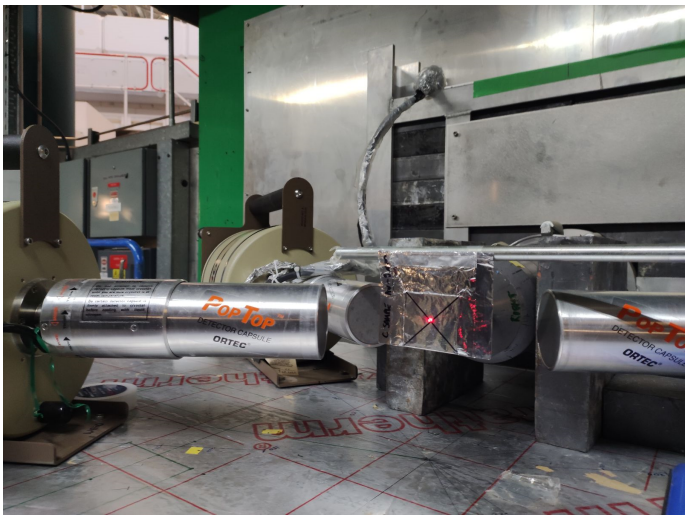

Figure 5.6: Experimental setup. The laser spot serves as a reference system to place the sample at the right height.

Data analysis

The spectra obtained from the measurements were analysed with the Origin software [17]. The first step in the data analysis consisted of peak identification. Peak energies were compared to standards and literature to find the elements responsible for each transition. Databases like Engfer, Zinatulina and MuDirac were employed during the identification

[18–20]. For each element, the most intense peak is used for depth profiling. Gold, for example, presents a quite intense peak at 130 keV, while copper and nickel are at 115 keV and 108 keV respectively. These peaks were used to reproduce a depth profile of the variation of the composition as a function of depth, as reported in Figure 5.7. For this analysis, the output of the Ge3 upstream detector was used. This detector presents a high efficiency and high resolution in the low to medium energy range (0-300 keV), which allows a good identification of the peaks. Furthermore, by using an upstream detector, problems of absorption of the X-ray from the copper matrix are avoided. A preliminary identification of peaks and their intensity variation was carried out also during the experiment, to help with the tune of the momentum scan. To finally produce a depth profile (Fig. 5.7, each peak was fitted with a Gaussian function and its area was normalised and plotted against the momentum. The three foils, as expected, have the same depth profile, with minor differences that are due to the different thicknesses of the layers. The full-width half maximum of the curves, as a first approach, helps in identifying differences. For gold, samples A and B have similar values: the first is 1.40 and the second is 1.42. Instead, sample C has a FWHM of 1.75. As expected, C has the larger layer of gold, while from these results, A and B appear closer than expected. Therefore, simulations were performed to assess the size of the gold layers.

Comparison with simulations

To assess the thickness of the gold layers, simulations were performed with TRIM and ARBY. Simulations consisted of the interaction of a negative muon beam with a six-layer type of sample. The first material to interact with muons is the Mylar window placed before the beam exit. This window is 5 μm thick and it is placed at 10 cm from the sample position. Given the low density of Mylar (1.38 g/cm^3) and the very thin size, this layer does not contribute to the absorption of the muon beam (< 0.5 % in the momentum range used for the experiment). The second material that interacts with the beam is the 10 cm air gap that divides the Mylar window from the sample. This gap is wide enough to stop low-energy muons, as shown in Figure 5.7, where the contribution from nitrogen, the main constituent of air is clearly visible. Finally, the last four materials to interact with the beam are, in order: aluminium, gold, nickel and brass. This alternation of layers was reproduced both in TRIM and ARBY. Here, TRIM was accessed through Mantid, a toolkit developed for data analysis that was used to run the simulation [21].

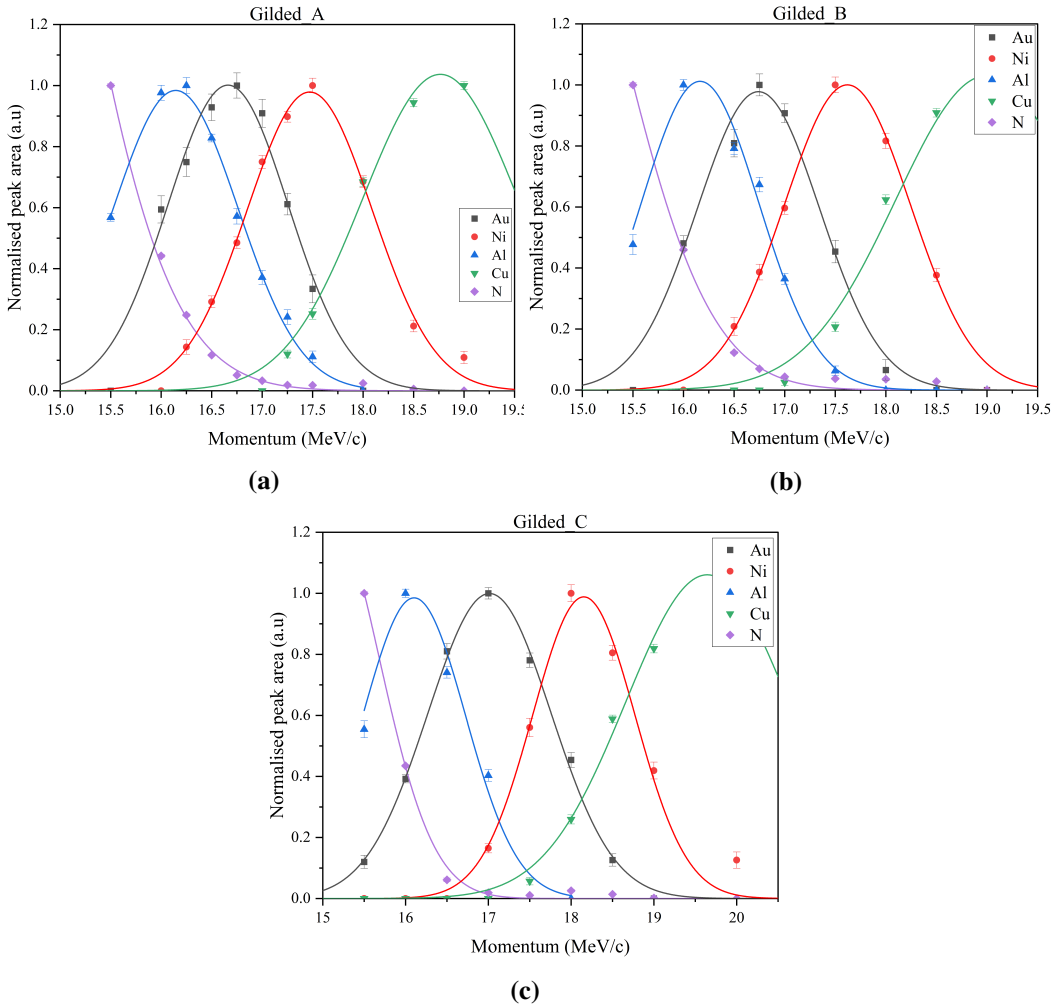

Figure 5.7: Depth profiles of the three standard samples. Each dataset was fitted with a Gaussian curve. A preliminary indication of the different sizes of the gold layer was given by the different values of the FWHM. For sample A, the FWHM value is 1.40 ± 0.07, for sample B is 1.46 ± 0.09 and for sample C is 1.75 ± 0.09. From this one can asses that the first sample as a thinner layer compared to the others.

Gilded A

Preliminary simulations performed before the experiment showed that the thickness limit for the detection of a gold layer was around 2 µm. Therefore, Sample A, with an average gold thickness of 3.3 µm could have represented a quite complicated sample. However, as shown in Figure 5.7a, with a fine-tuning of the momentum, a nice gold signal was detected. Starting from these preliminary considerations, simulations were performed. The work aimed to characterize the gold layer, but the presence of a well-defined nickel layer, as well as the

aluminium holder, extended the characterization to all layers. For this sample, simulations were performed with a different size of the gold layer, as shown in Figure 5.8. To have a parameter for the comparison between simulation and experiments, a normalization to one was performed and the reduced χ-square was calculated. Here, along with a visual comparison of the profiles, the χ-square helps in finding the best agreement between the simulation and the real data. For all samples, the characterization was mostly performed with the GEANT4/ARBY tool and the final result was compared with TRIM. The results reported in Figure 5.8 were performed with the nominal momentum spread of 4%. For this set of simulations, the best agreement was reached with a thickness of 3.5 ± 0.5 μm, but the result was not completely satisfactory.

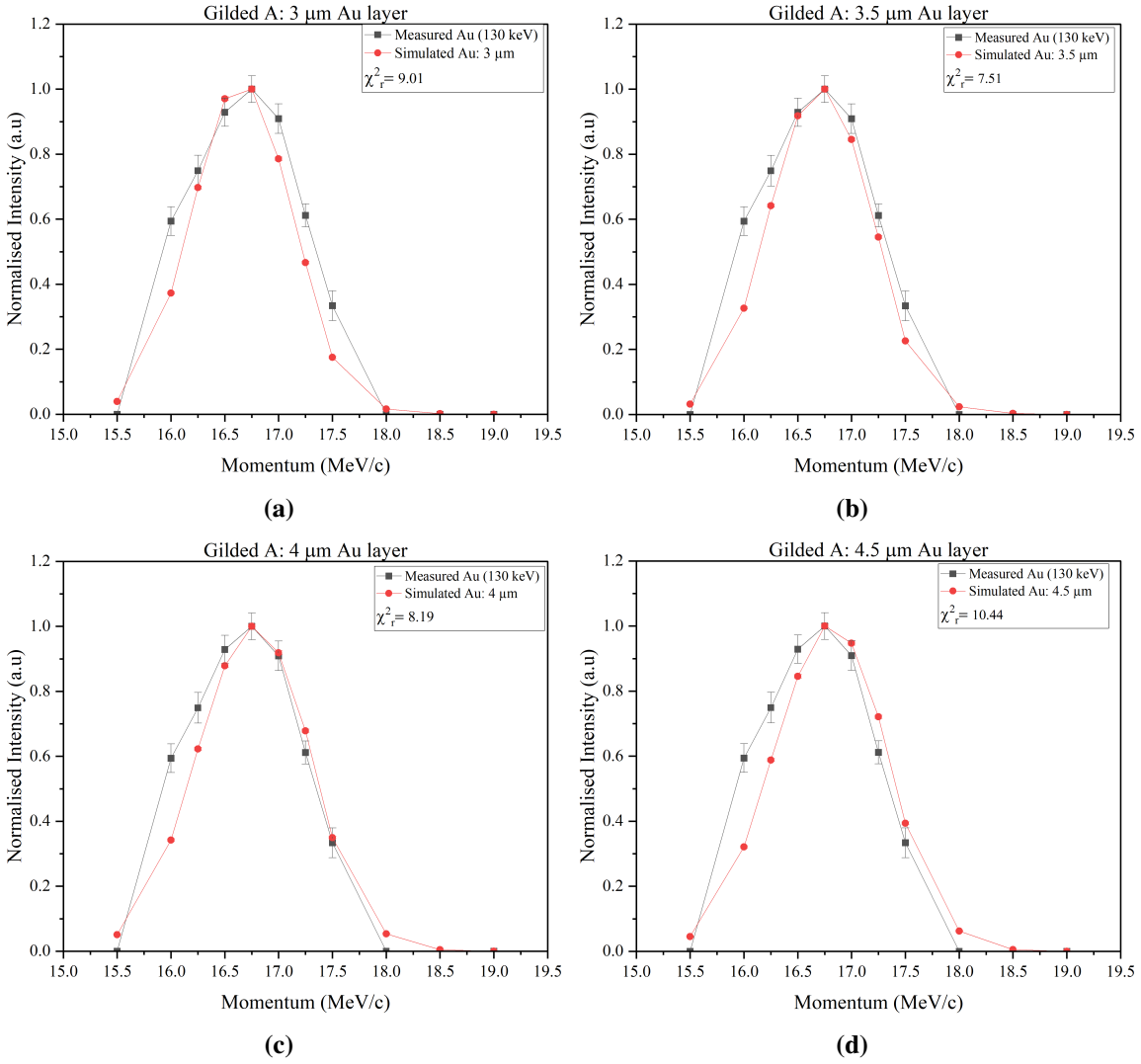

Figure 5.8: Gilded A: old layer simulations with an 0.5 µm increase. Each simulation provides a good model of the real measurement: the only main discrepancy is represented by the point at 16 MeV/c, where the measured gold signal is always higher than the simulated one. This could be due to the fact that the layer is not completely even and has areas thicker than others.

Therefore, another set of simulations was performed with an increased momentum spread of 5%, and the results provided an improved agreement between the simulation and the measurement, as shown in Figure 5.9a, where a reduced χ^2 of 2.16 was reached. By increasing the momentum spread, the beam profile, described by a Gaussian is wider, resulting in a wider profile of the simulated curve. Finally, simulations were performed with TRIM. Here, Figure 5.9b reports the final results of the gold layer. As for ARBY, the best fit was reached at 3.5 µm, but the simulated depth profile presents bigger discrepancies at the first momentum run and at the high momentum runs. As shown, the simulated depth profile

is wider than the measured one, even if, for this set of simulations the momentum spread was set to 4%. In addition, this set of simulations was performed at an increased source-to-detector distance (10.5 cm), which was found to be more suitable to fit the experimental data.

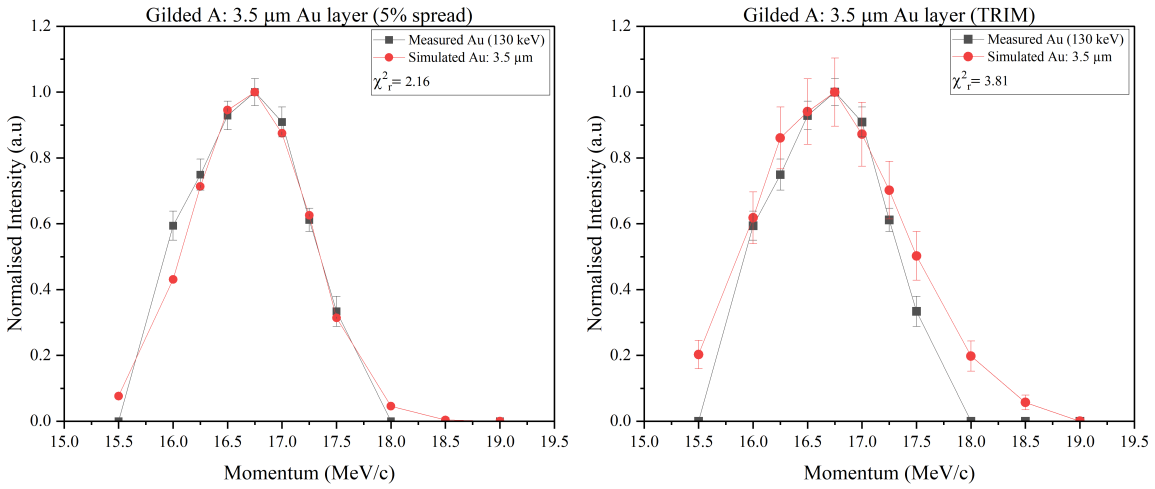

(a) **(b)**

Figure 5.9: Final characterization of the gold layer. a) with ARBY, the best fit was reached at 3.5 ± 0.5 µm, with a reduced χ^2 of 2.16. b) with TRIM, with the same condition, the best fit was reached at 3.5 ± 0.5 µm, with a reduced χ^2 of 3.81 .

Finally, with the gold layer defined, the other layers were characterized, as shown in Figure 5.10. Here, the air profile (Fig. 5.10a) is basically the same, while the aluminium profile shows more discrepancies (Fig. 5.10b). The aluminium profile has represented a complicated issue in all three samples, even if its size was known. The discrepancies suggest that in the ARBY simulation, the layer seems to be thinner and its signal decreases more quickly than in the real measurement. Given that the size and the geometry were checked before each simulation, this feature could be due to the fact the sample positioning was not precisely perpendicular to the beam. Considering the size of the uncollimated beam spot, a variation of the source to detector distance could explain a broader signal of the aluminium layer. The nickel, on the other hand (Fig. 5.10c), was defined as an 8 ± 0.5 µm, layer, in agreement with the SEM results. The simulated depth profile is reported in Figure 5.10d.

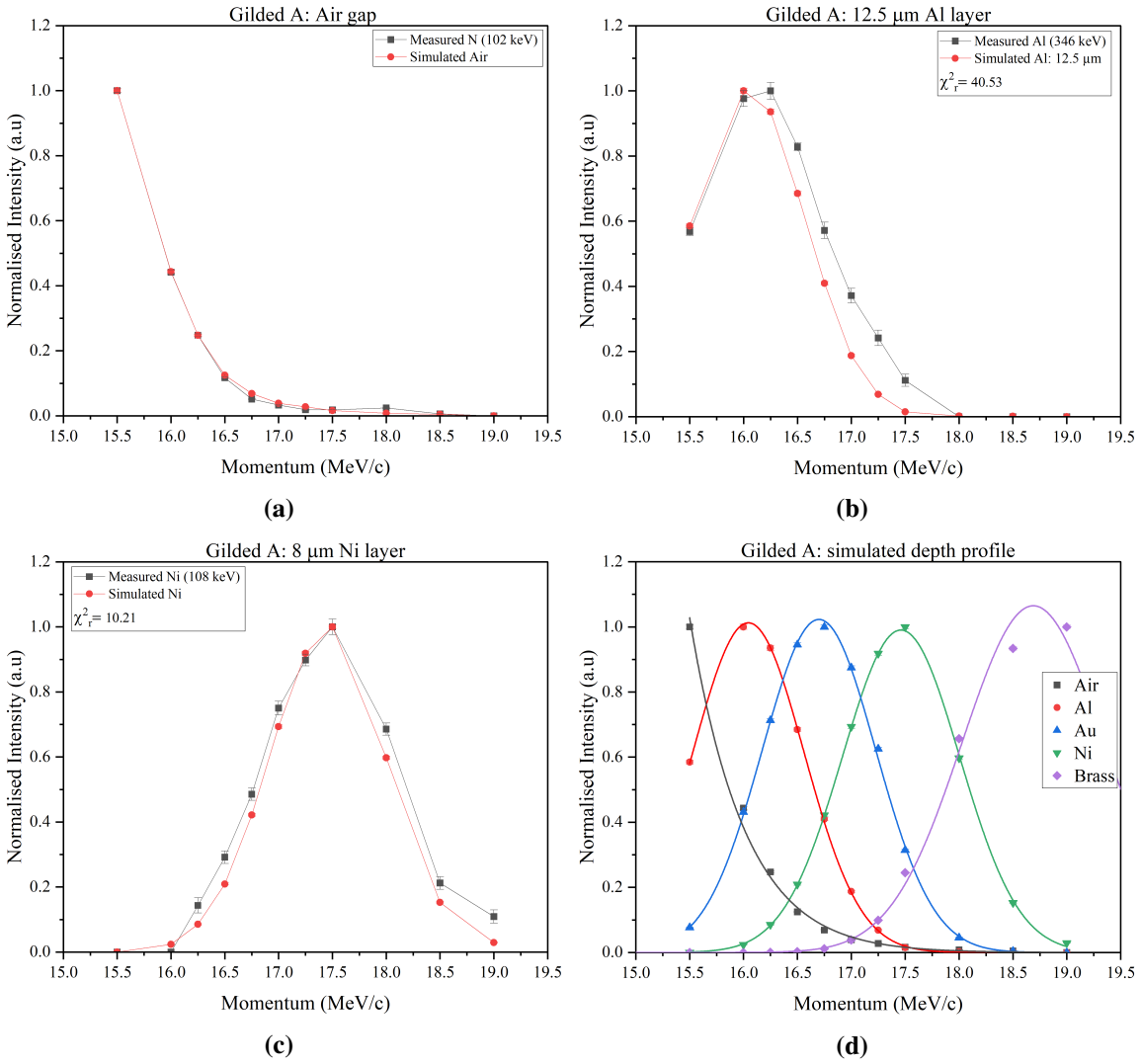

Figure 5.10: Characterization of the other layers present in the sample. The air profile (a) is well reproduced: here, the nitrogen signal was compared with the air signal of the simulation; aluminium (b), was more difficult to model and the discrepancies between the simulations and the data are higher. For nickel (c), instead, the best fit was reached with an 8 ± 0.5 µm. Finally (d), the simulated depth profile.

Gilded B

As sample A, the characterization of the gilded layer started with a set of simulations performed with the nominal momentum spread and an increase in the layer size of 0.5 µm. Figure 5.11 reports the results of these preliminary calculations, with the best results obtained for 4 and 4.5 µm (Fig. 5.11a,b). Here, the measured average thickness was 4.6 ± 0.5 µm, and an increase in the size of the layer produced higher discrepancies (Fig. 5.11c,d).

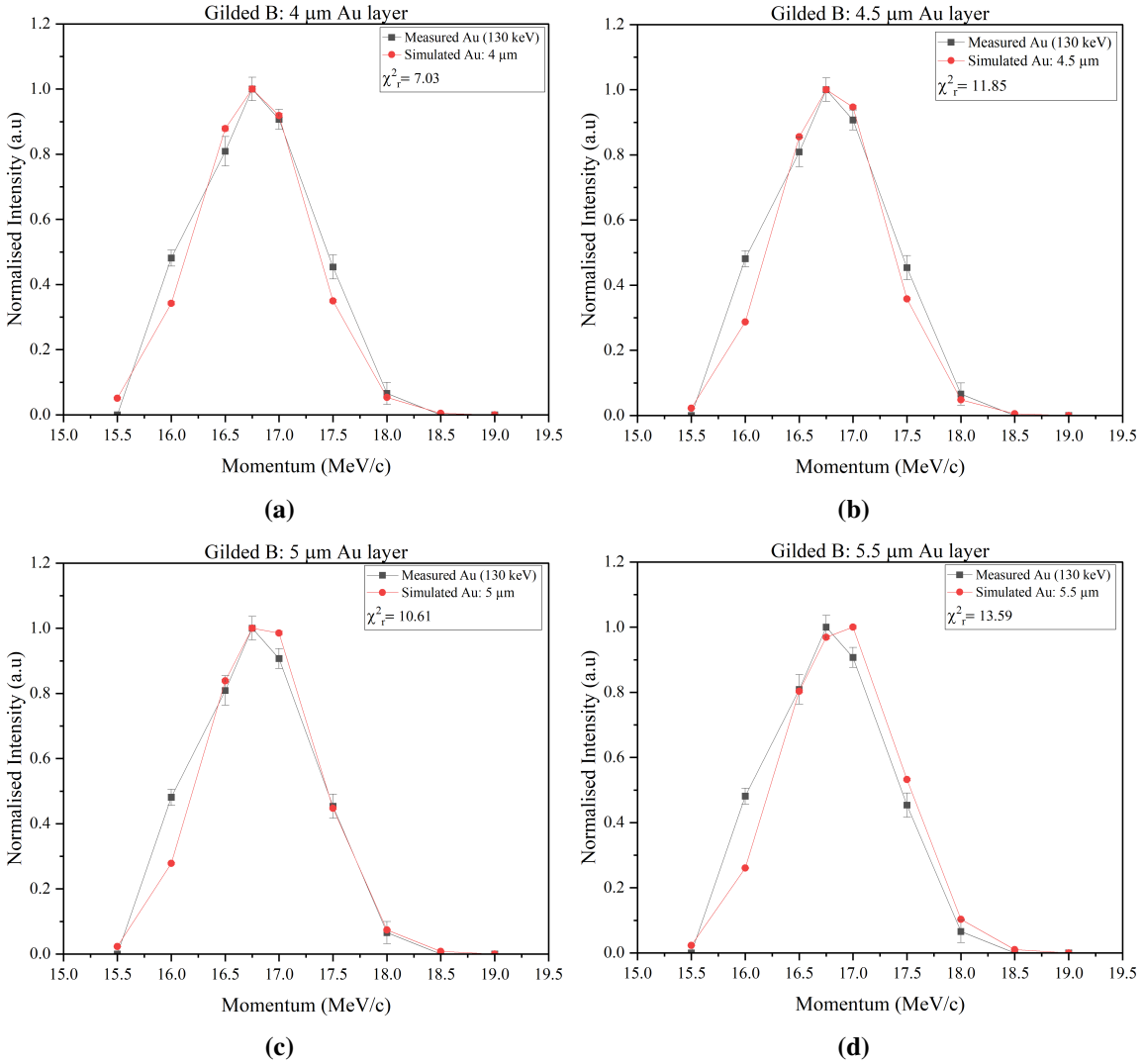

Figure 5.11: Gilded B: gold layer simulations with an 0.5 µm increase. As in sample A, the only main discrepancy is represented by the point at 16 MeV/c, where the measured gold signal is always higher than the simulated one. This could be due to the fact that the layer is not completely even and has areas thicker than others.

With the two best results from the first set of simulations, the momentum spread was increased to 5% and a better agreement between simulation and measurement was reached. With ARBY simulations, the best fit was reached at 4.5 ± 0.5 µm with a reduced χ^2 of 3.14. As in the previous sample, TRIM simulations were performed and the best fit was reached at 4.5 ± 0.5 µm with a reduced χ^2 of 15.05. Here, the discrepancies are more pronounced than in sample A, even if the simulation conditions were not changed. As stated before, TRIM seems to provide worse results than ARBY when dealing with a few microns layer. In addition, with TRIM it was more complicated to reproduce the other layers and to have

a better agreement, the distance of the sample had to be increased by 0.5 cm.

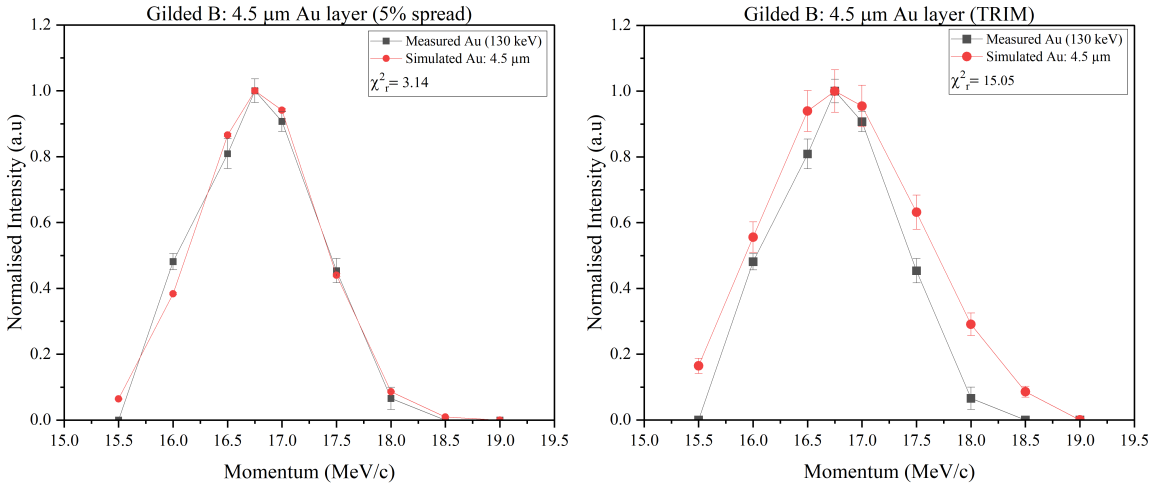

Figure 5.12: Final characterization of the gold layer. a) with ARBY, the best fit was reached at 4.5 ± 0.5 µm, with a reduced χ^2 of 3.14. b) with TRIM, with the same condition, the reduced χ^2 of 15.05

With a defined gold layer, the other materials were characterized. As sample A, the air gap was well reproduced (Fig. 5.13a) and the same problems with the aluminium layer were assessed (Fig. 5.13b), but with fewer discrepancies than sample A. Nickel (Fig. 5.13c), as sample A was well described by an ± 0.5 µm. Finally, the simulated depth profile is reported in Figure 5.13d.

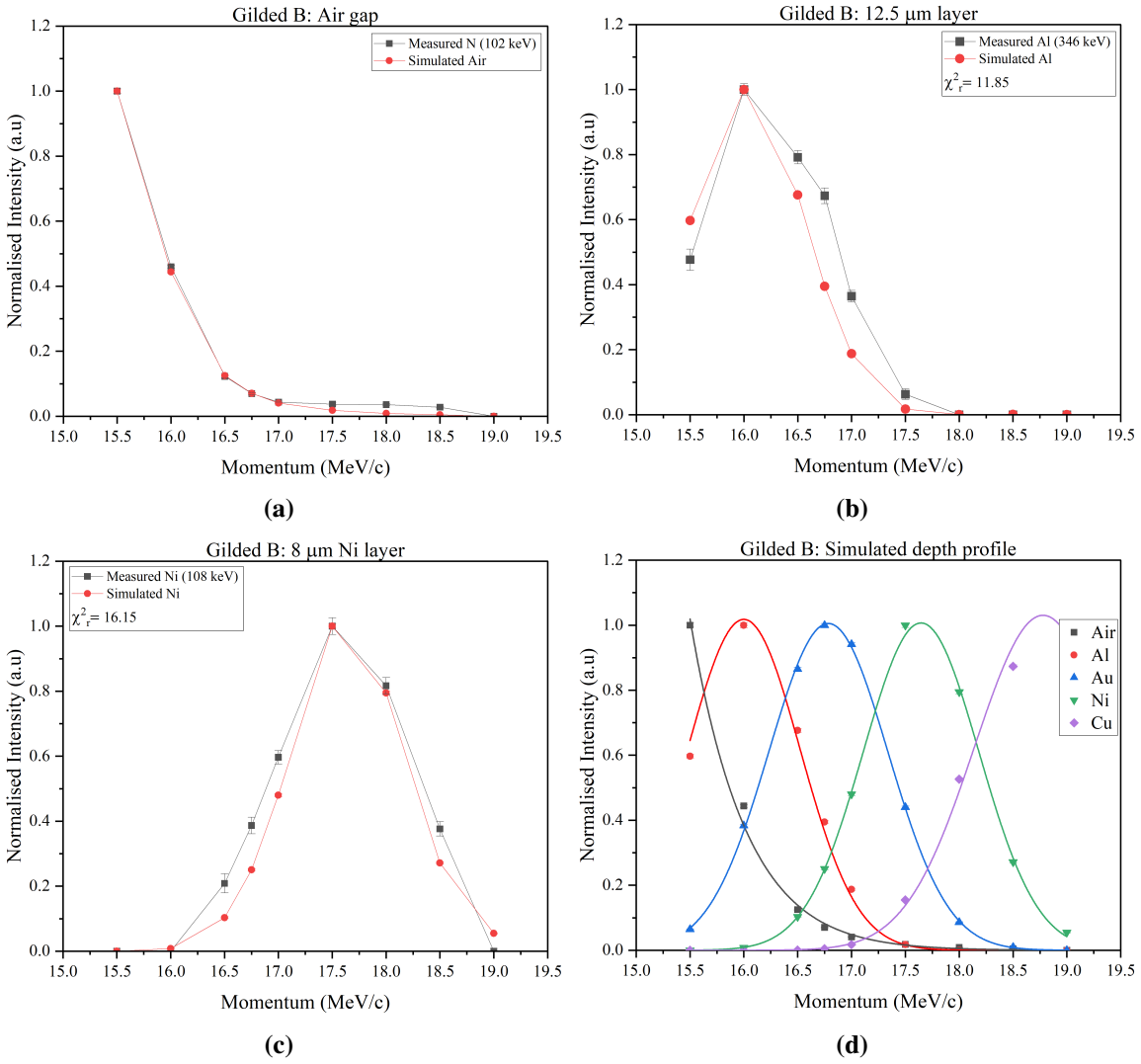

Figure 5.13: Characterization of the other layers present in the sample. The air profile (a) is well reproduced: here, the nitrogen signal was compared with the air signal of the simulation; aluminium (b), was more difficult to model and the discrepancies between the simulations and the data are higher. For nickel (c), instead, the best fit was reached with an 8 ± 0.5 µm. Finally (d), the simulated depth profile.

Gilded C

Sample C had the thicker gold layer of the three, with an average thickness of 7.3 ± 0.8 µm. This sample was the first measured, with fewer points and 0.5 MeV/c momentum steps. To have a preliminary indication of the size of the layer, simulations were performed with a 1 µm step, from 6 to 9 µm (and nominal momentum spread), as reported in Figure 5.14. Here, differently from the previous results, the discrepancies between simulation and

measurements are higher, and the best fit was reached at 7 µm.

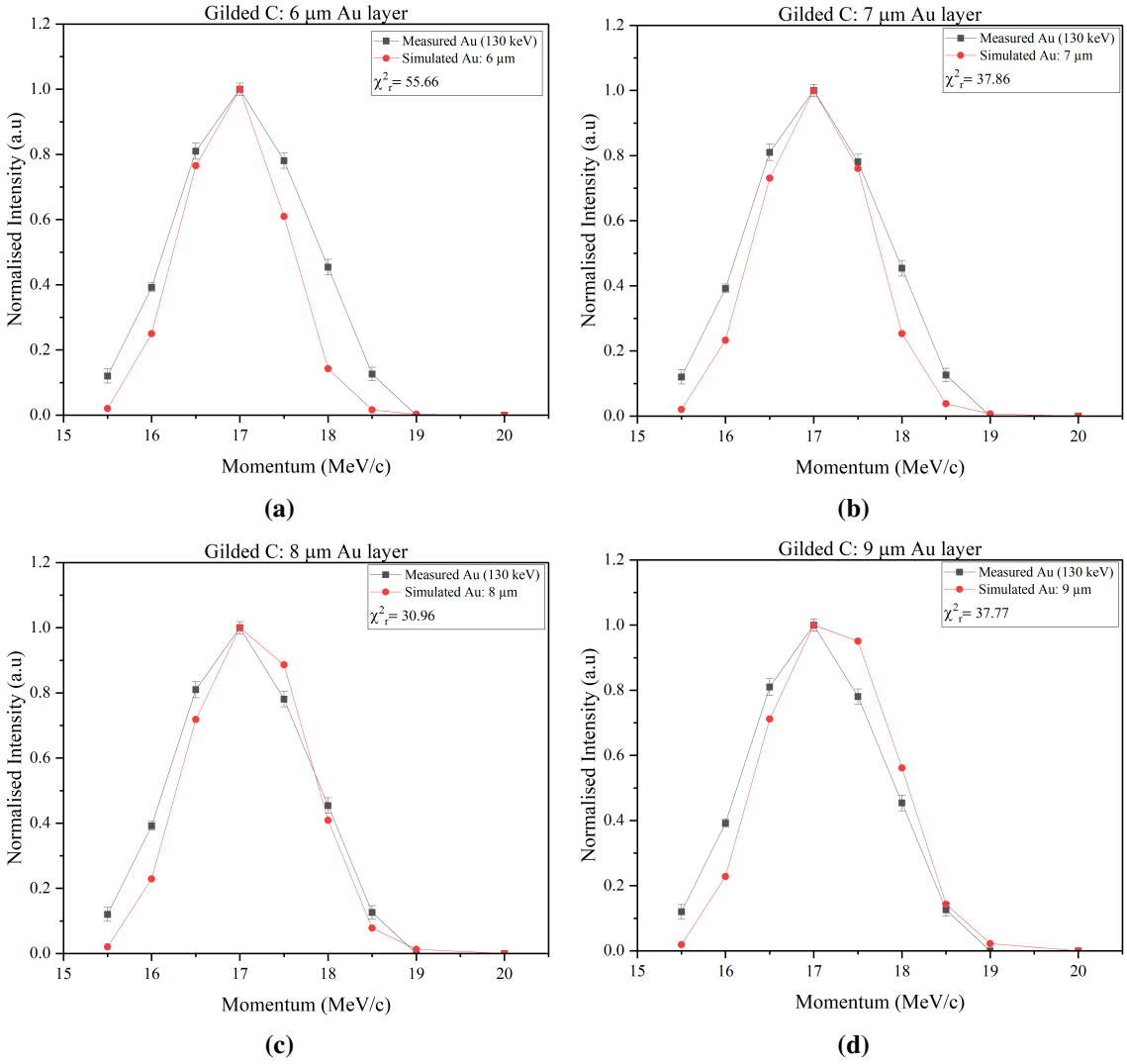

Figure 5.14: Gilded C: gold layer simulations with an 1 µm increase. In a and b, the simulated profiles are thinner than the measured one, while when increasing thickness (c,d), the simulation exceeds the measured profile.

The results of the gold layer with a 4% momentum spread affected also the other layers, especially aluminium, which was not well reproduced (not shown). Therefore, another set of simulations was performed, this time with a 5% momentum spread. In addition, to cope with the difficulty of reproducing the aluminium layer, simulations were performed with the sample placed a little bit closer to the beam exit, to address errors in positioning. This set of simulations, as reported in Figure 5.15, provided improved results. The reduced χ^2 testifies

to a better agreement, with the best fit reached with a 7.5 ± 0.5 µm gold layer, both at 9.75 and 10 cm.

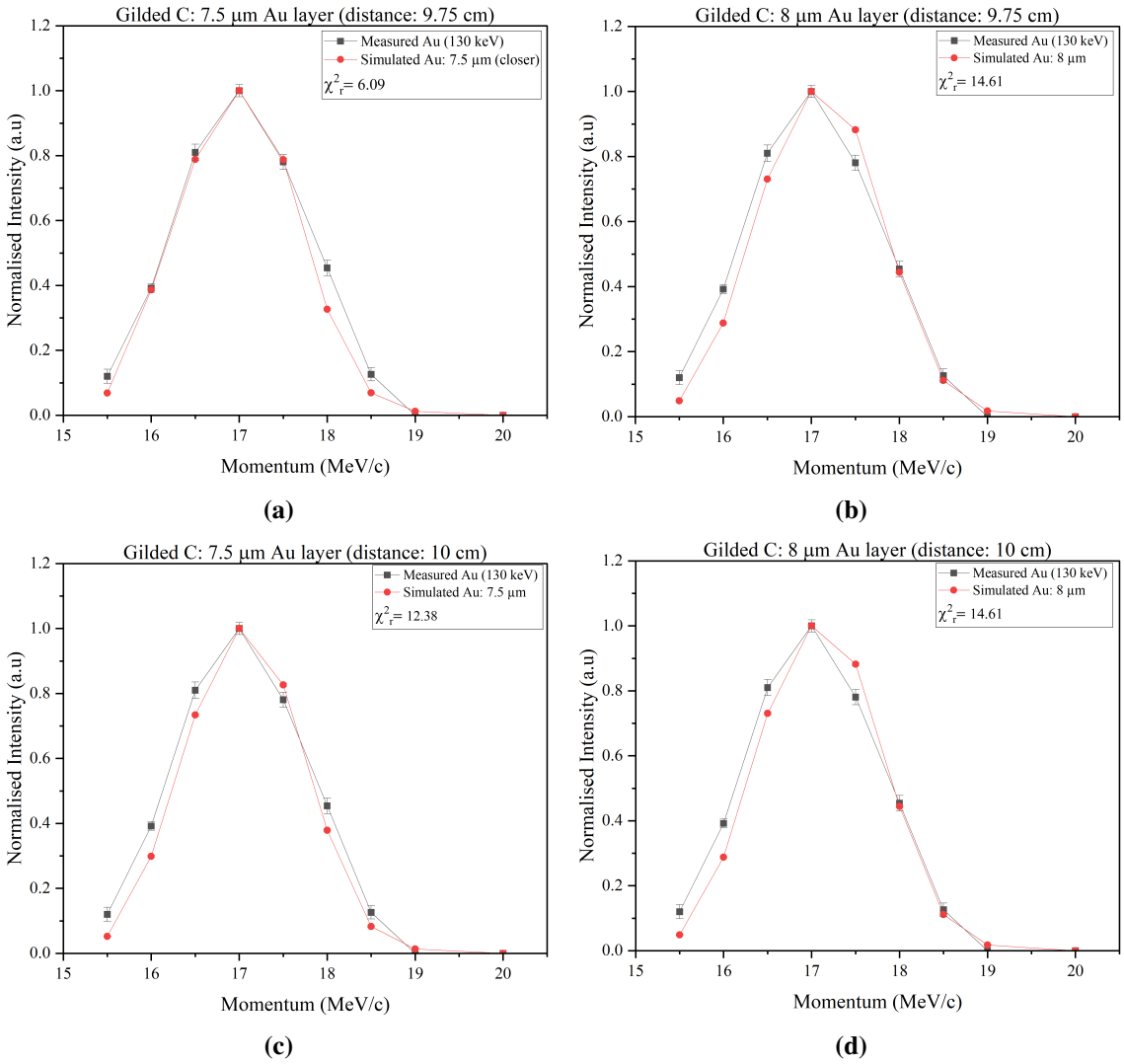

Figure 5.15: Gilded C: simulations with 5% momentum spread. The best fit is reached in a, with a reduced χ^2 of 6.09 for a 7.5 µm gold layer.

However, the best fit for the gold layer corresponded to worse results in the other layers of the sample. As shown in Figure 5.17b, at a 9.75 cm distance, the discrepancy between the simulated values of aluminium from the measured values is quite high. This discrepancy decreases when moving the sample away from the source. Therefore, the simulated gold layer with the best result was found to be the one with a 7.5 µm thickness placed at 10 cm. For nickel, instead, the best fit was reached with an 8.5 ± 0.5 µm. Finally, different from the previous samples, the TRIM characterisation of the gold layer provided a better agreement

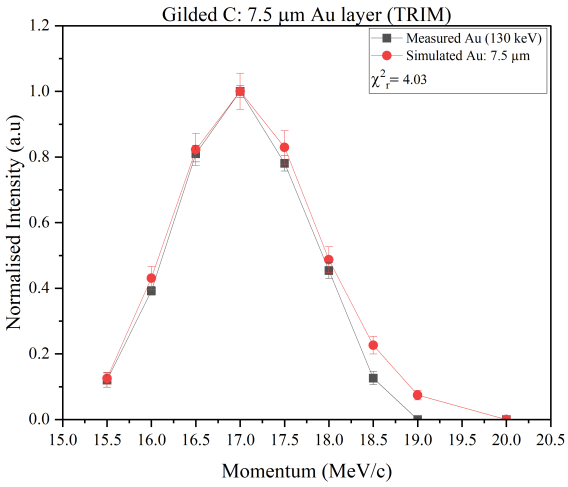

Figure 5.16: Gilded C: TRIM simulations. The best fit is reached in a, with a reduced χ^2 of 4.03 for a 7.5 µm gold layer.

with the measured data than ARBY, as shown in Figure 5.16. Here, simulations were still performed at 10.5 cm from the source and a 4% momentum spread.

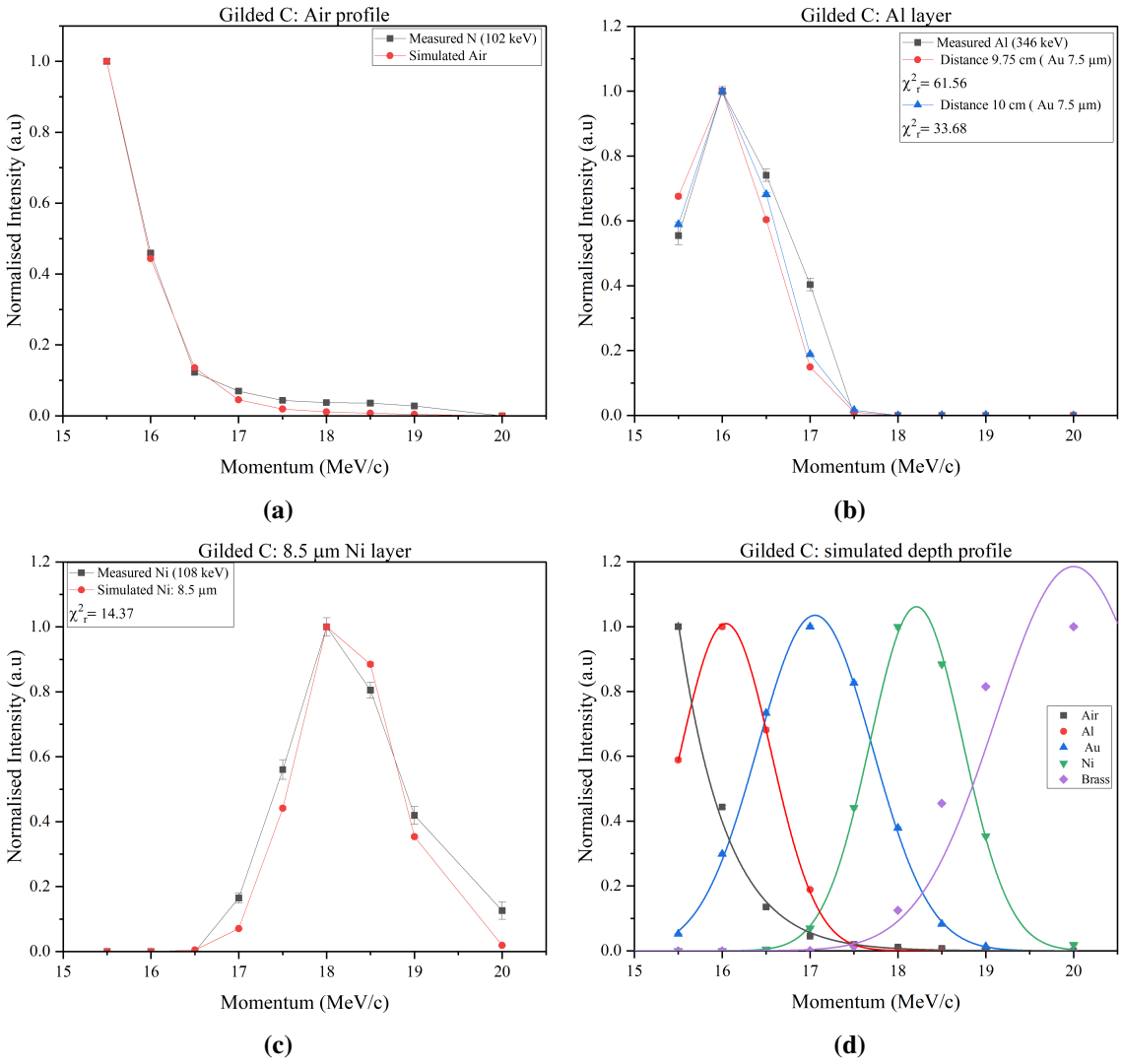

Figure 5.17: Characterization of the other layers present in the sample. The air profile (a) is well reproduced: here, the nitrogen signal was compared with the air signal of the simulation; aluminium (b), was more difficult to model and the discrepancies between the simulations with samples close to the source are higher than 10 cm distance. For nickel (c), instead, the best fit was reached with an 8.5 ± 0.5 µm. Finally (d), the simulated depth profile.

Final considerations

The focus of the experiment was the characterization of three known layers of gold to validate the use of simulation software for the assessment of thin layers. The results provided a remarkably good agreement between the simulated and measured thicknesses, as reported in table 5.1. Moreover, thanks to the composition of the samples, it was possible to characterize the size of the nickel layer. This is an important result for the technique, that testifies

to the capability of investigating the different layers that could be present in a sample. Yet, some more improvements are necessary to improve the method's reliability. Starting from the experimental procedure, it has been addressed that the sample positioning could influence the simulation process. Therefore, especially with layered materials it is important to carefully place the sample in front of the beam exit and perpendicular to the beam direction. In the case of the gilded foils, the sample was hanging from an aluminium bar, as shown in Figure 5.6. The setup has been used for many experiments, but for this specific case, where the modelling in simulation software was an important part of the experiment, it represented a source of error. In addition, taking into account all the aspects that could have influenced the measurement, the sample position could have been moved by air flowing in the sample area. Port4, indeed, is close to an entrance gate in TS1, which, when opened, could cause the movement of the sample. Moreover, the detector needed refilling every 24 hours, so the instrument area had to be open. Therefore, one could think of an improved sample holder to try to remove the external source of errors. For negative muon analysis, however, it is difficult to think of a holder, because it has to be taken into account that any material that enters the beam will produce a signal. Here, aluminium becomes part of the sample and it is easily simulated. A different holder would have to be either outside the beam spot or made with a material that does not influence the measurement. For sure, it would be good to think of a way to make the holder more stable, to keep it perpendicular to the beam during the experiment. Then, it has to be considered that for this specific type of sample, in the two samples, there is a significant difference between ARBY and TRIM simulation, while sample C provided better results. For thin layers of gold, such as A and B, the TRIM software was less efficient than ARBY, while as the gold size increased, the TRIM simulation improved. For the three samples, ARBY provided consistent results, with similar issues in each simulation (for example the aluminium profile) that can be due to incorrect distances or the positioning of the sample. TRIM, on the other hand, was more influenced by the parameters of the simulations and the presence of many thin layers. What emerges from this characterization, in the end, is that besides diversities in the simulation process, by improving the simulation parameters, both software can provide a reliable source for better data interpretation.

Table 5.1: Gilded samples: comparison between SEM and simulated μ-XES results (both for TRIM and ARBY)

Sample	SEM Au thickness (μm)	μ-XES Au thickness (μm)
A	3.3 ± 0.2	3.5 ± 0.5
B	4.6 ± 0.6	4.5 ± 0.5
C	7.3 ± 0.8	7.5 ± 0.5

5.2.3 Replicas of ancient gilding

The results reported in the previous paragraph provide a good starting point for the application of the method on real samples. In this paragraph, the analysis performed on two handmade pieces of copper alloys covered in gold will be discussed. The two pieces were made as a replica of the material used in the south baptistery gate of Florence and gilded with the amalgam technique (composition is reported in table 5.2. They were made by the *Opificio delle Pietre Dure*, a restoration centre in Florence, to study the characteristics of a gilded surface prior to the restoration.

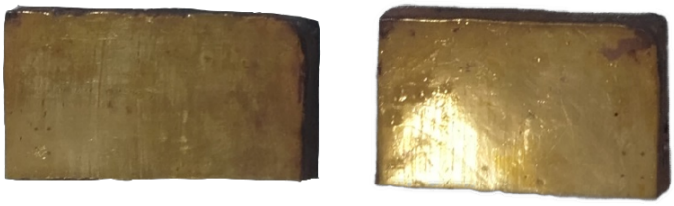

Figure 5.18: Left: SM3, a gilded brass; Right: EM2, a gilded bronze. Sample dimensions: 45x25x5 mm.

The gilding was done following the Cellini recipe [14]. However, the control of the process was difficult, the surface was heated up too much and the gilded layer, as reported in Figure 5.19 presents some cracking and bubbles due to the evaporation of mercury. What is interesting for this sample, is that the SEM scan gives the opportunity to perform a momentum scan and compare, as before, the results to the one of the simulation. The experimental setup consisted of 4 HPGe detectors placed at 15 cm and with a 30° angle from the sample position, that is 10 cm in front of the beam exit. For the experiment, the beam was not collimated. A momentum scan was performed from 15.5MeV/c up to 24 MeV/c for an average measuring time of 4 hours (RB1910123).

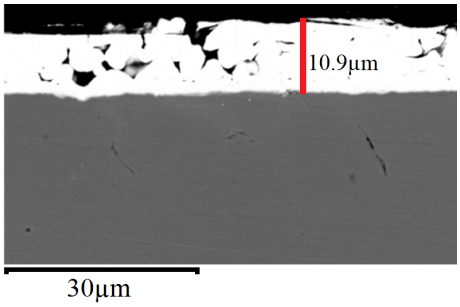

Figure 5.19: SEM image of the gilding: bubbles and cracks testify poor control of the fire gilding process. It has to be stated that air bubbles are not defects but are typical of this type of gilding procedure, but they are generally flattened out by burnishing. Here, the gold layer is about 11 µm.

Table 5.2: SEM-EDS average composition of the samples (wt%).

	Cu	Sn	Zn	Sb	Pb
EM2	93.1 ± 0.9	2.8 ± 0.2	2.8 ± 0.2	0.8± 0.1	0.5 ± 0.1
SM3	74.1±0.8	20.1 ± 0.6	3.9 ± 0.2	1.1 ± 0.1	0.8 ± 0.1

Data analysis

As for the gilded foils described above, data analysis consisted of peak identification and fitting. Results confirmed the presence of the elements reported in Table 5.2 except for lead and antimony, which are in a concentration lower than the detection limits for the two elements. A typical X-ray spectrum (at different momentum) is reported in Figure 5.20, in the range where zinc (123 keV), gold (130 keV) and oxygen (133 keV) peaks occur. Here, it is possible to appreciate how μ -XES can perform depth characterization studies. Significant is the peak at 123 keV, which corresponds to zinc, an element present in the alloy, that is zero at 16 MeV/c and then increases with momentum. This means that as the beam momentum increases, the muon beam goes through the material, giving back information about its component that can be used to assess a layered structure or a compositional variation along the depth.

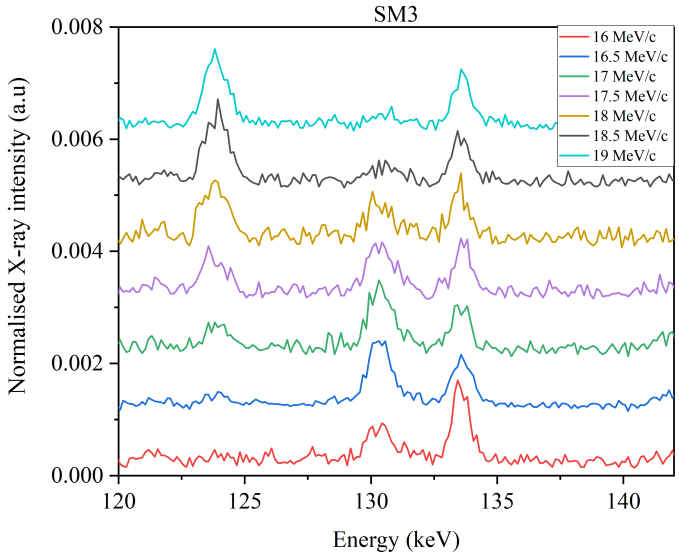

Figure 5.20: X-ray spectra of the brass sample at different momentum. The peak at 133.4 keV (oxygen) is present in every run due to the fact that the beam spot size is bigger than the sample.

In the two samples, each layer was characterized by an element in major concentration: nitrogen (air), aluminium, gold and copper. Therefore, for each element, a peak was se-

lected and fitted with a Gaussian function for every run. The area under the peaks was then normalised and plotted against the momentum variation to obtain a depth profile, as shown in Figure 5.21.

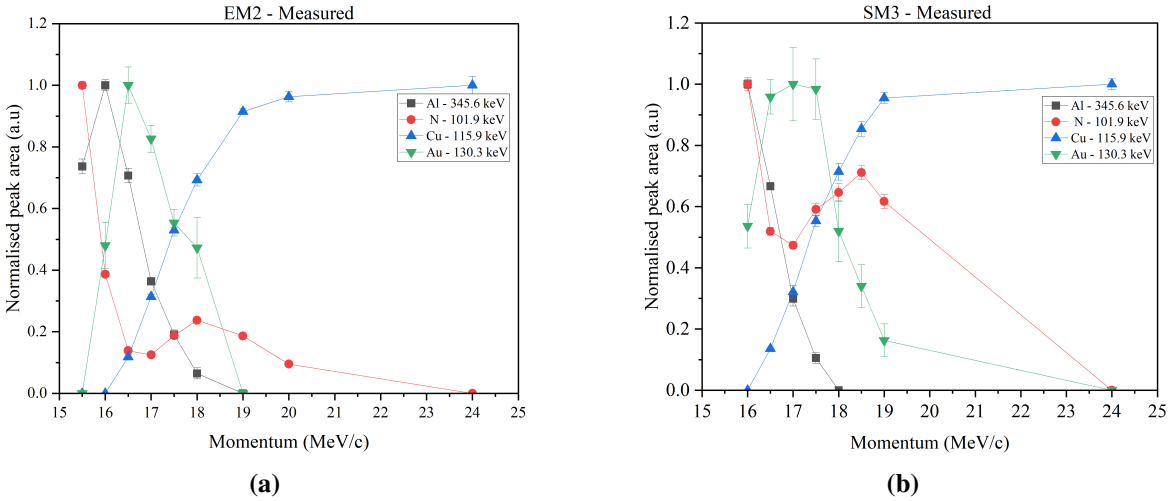

Figure 5.21: Depth profile of sample EM2 (a) and SM3 (b). Both samples are characterized by the increase in the nitrogen signal at the gold-copper interface, suggesting the presence of a nitrogen-based thin layer.

The two plots present similar characteristics and an unusual profile of air (red line). At the gold-copper interface, indeed, it is possible to see an increase in the nitrogen peak intensity. Instead of constantly decreasing to zero, as one would expect, the information coming from air increases, with a peak around 18 MeV/c and then starts to decrease again. This could be due to the fact that the beam spot was bigger than the sample, so at higher energies, it is possible to have a signal coming from the muons stopped in the air near the sample. However, since the signal of air is lower at the highest momentum runs, there could be another explanation. This particular profile could be due to the remaining treatment/polishing of the copper surface with nitric acid (HNO_3) before the application of gold, which was confirmed also by the craftsman. Since the aim of the work was to characterize the gold layer, this issue was not fully investigated but represents an interesting problem. Finally, the two gold profiles were plotted together, as shown in Figure 5.22. The two profiles present some differences, which could be due to the different characteristics of the layers. In particular, the difference could be due to a different thickness or to the unevenness of the layer due to the presence of cracks and bubbles of air.

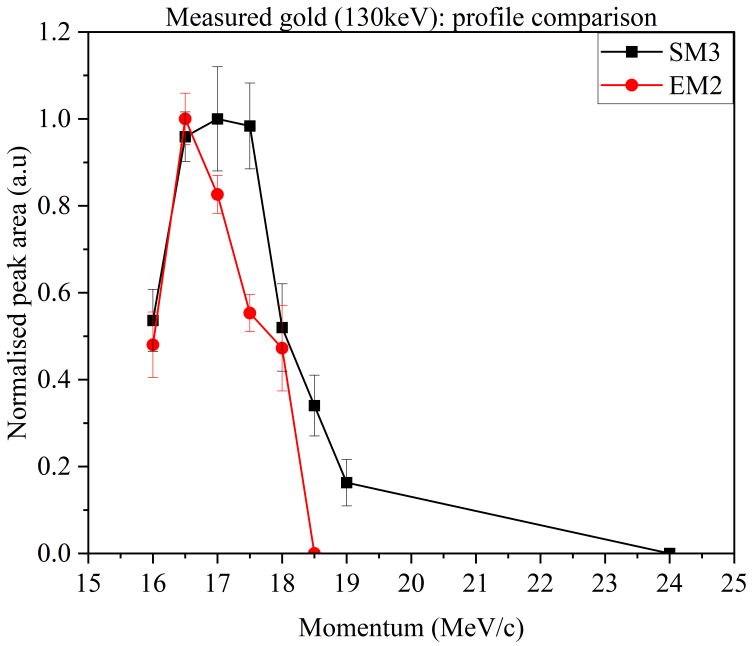

Figure 5.22: Comparison of the gold profiles of EM2 (red) and SM3 (black). The result show a clear difference in the two layers, due to a uneven surface or to the presence of defects.

Comparison with simulations

Differently from the previous section, to evaluate the differences in the two profiles and replicate the experiment, the TRIM tool was used at first. Simulations were performed with the beam window, the air gap and the aluminium foil with fixed thicknesses (0.001, 0.1 and 0.05 mm each) while the gold layer was modified for each simulation. The copper layer thickness was set at 0.5 mm. The work consisted of a set of simulations at different beam energies to replicate the momentum scan with a momentum spread of 4%. As a result of the TRIM simulation, a percentage of muon stopped in each layer is given. This value (that was normalized), was compared with the normalized X-rays intensity of the analysed spectra to evaluate the layer thickness. Figure 5.23 shows the different results obtained from the tuning of the simulation parameters. The process involved many different tests to find the best fit: here, only the more significant will be reported. For the EM2 sample, preliminary simulation with a 10 µm layer of gold produced results with a large deviation from the experimental values. In addition, even by reducing the size of the layer, by using a standard density of gold, the results were still far from a good fit (Figure 5.23 a,b). Therefore, assuming that here the gold layer was thinner than in the other sample, size was decreased as well as density. This was done to try to replicate the presence of air bubbles in the layer, that cannot be modelled in the simulation (for TRIM especially). The manufacturing process used to make the sample, indeed, could have left bubbles of air in the layer that could be responsible for the shape of the profile. Density, in detail, was reduced by 5, 10, 15 and 20%

from the standard value of 19.32 g/cm^3. This, indeed, produced results that fitted better the experimental data(Fig. 5.23 c and d). Finally, for EM2 the best fit was reached with a gold thickness of 5 µm and the density of the material decreased by 20% from the nominal value of gold (19.32 g/cm3). Here, a reduced χ^2 of 2.60 for both SRIM-TRIM and ARBY was obtained, as shown in Figure 5.25.

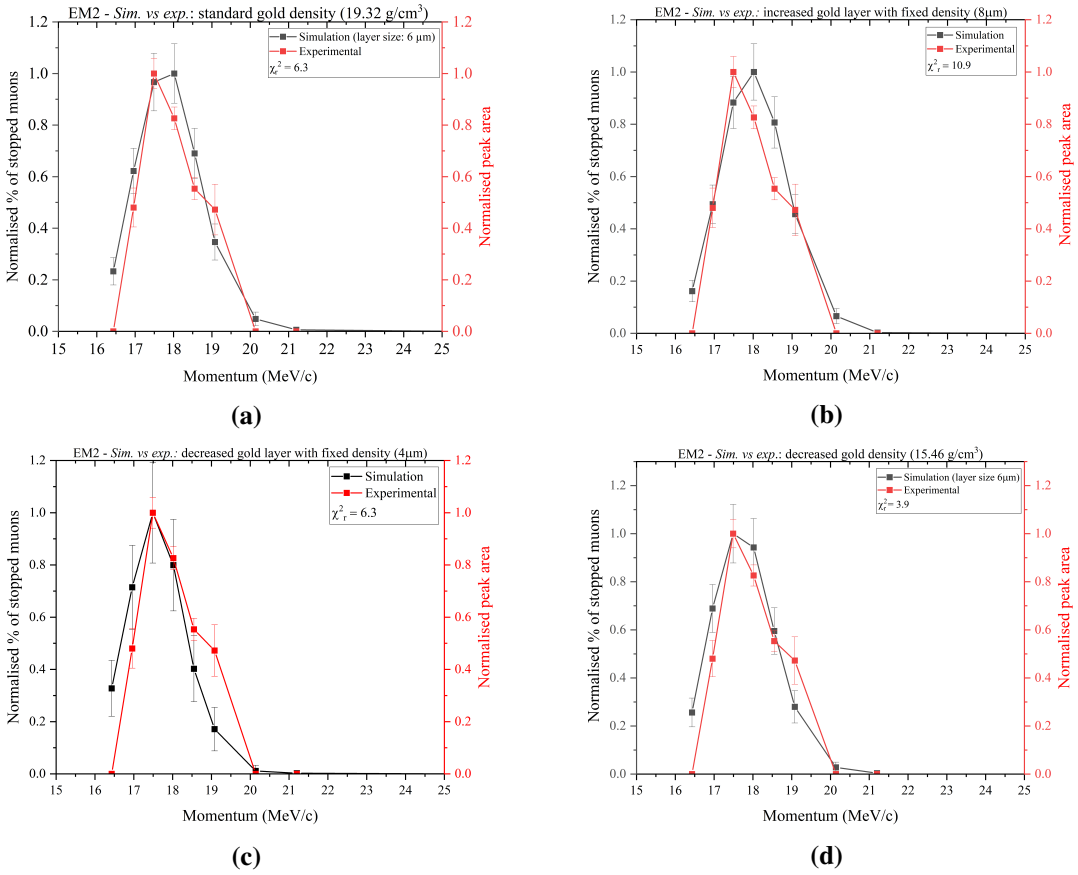

Figure 5.23: EM2 sample. The gold density was decreased down to 25% of the original value to consider the effect induced by the presence of air in the layer; a) with standard gold density and a 6 µm layer, the simulated data have a worse fit than the ones with lower density (b,c). The best fit is reached in (d), where along density, the thickness of the layer is reduced to 5 µm.

For sample SM3, instead, a decrease in size and density produced outputs with a big deviation from the experimental data, as shown in Figure 5.24. Here, only size was changed, in a range from 8 to 12 µm. The best fit was reached with a thickness of 11 µm and standard gold density. A reduced χ^2 of 1.23 for SRIM-TRIM and 2.40 for ARBY was obtained (Fig. 5.25 b).

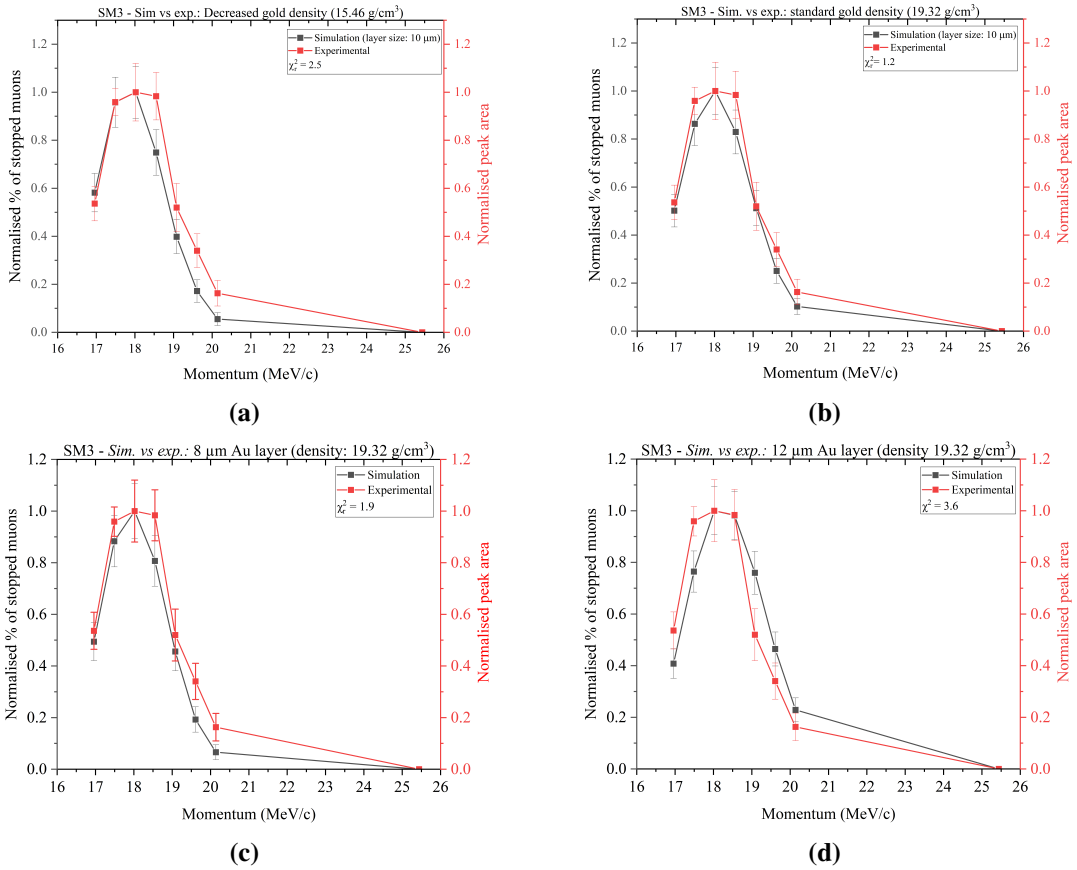

Figure 5.24: SM2 sample. Small variation in the layer width results in a fluctuation of the agreement of the datasets. In (a) and (b) the layer is too small or too big, whereas in (c) the results have a better agreement. The best fit is reached in (d), with an 11 µm layer of gold.

The results obtained from sample SM3 confirm the information provided by the SEM scan reported above. In addition, there is a good agreement between TRIM and ARBY's results. For EM2, the process was more difficult, since the simulated gold profile with a thickness of around 10 µm and standard gold density produced output with a big deviation from the real values. The results obtained provided a good fit, but the particular profile of gold could be also due to an uneven distribution of gold in the layer. Anyway, both results provided a good comparison between the two simulation software, testifying to the goodness of the ARBY tool.

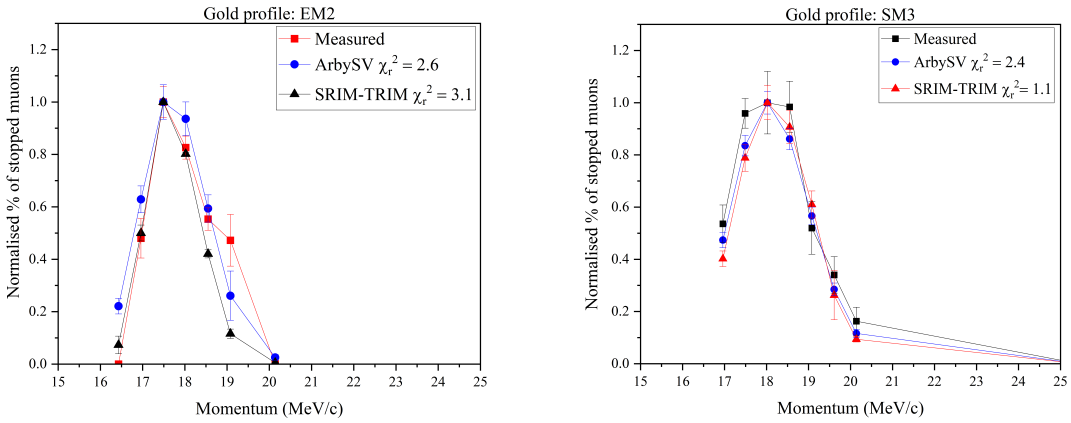

Figure 5.25: Gold depth profile from measured and simulated data analysis; (a) EM2 sample; (b) SM3 sample. Even if the sample looks similar, muon data suggest a different size of the gold layer.

5.2.4 The *formella* of the Florence baptistery gate

After working with standard and test samples, the method was applied to the analysis of a piece of the south baptistery gates of Florence. The *Porta del Battistero*, adorned with stories of St. John the Baptist, is one of the oldest Middle Ages bronze gates in existence in Europe, designed by Andrea Pisano and crafted in cast and chiselled bronze, partly gilded, by Lorenzo D'Avanzo and co-workers between 1329 and 1336. The door is divided into 28 quatrefoil panels, each depicting a single episode or figure, while the frame is decorated with rosettes and lion heads. In 2021, the baptistery gates were undergoing the last part of their restoration before being finally displayed to the public at the Museo dell'Opera del Duomo in Firenze. On this occasion, a piece of the south gate travelled to the UK to be analysed by means of neutrons and negative muons. The aim of the measurements was to gain information about the gate manufacturing method by identifying: the number and position of the casting channels; the composition and homogeneity of the brass alloy in the different areas; the general quality of the casting through the identification of the presence and size of bubbles, flaws and defects; the composition and thickness of the mercury amalgam gilding. The last, in particular, was investigated with negative muons. The object of the analysis, in particular, was the *formella* shown in Figure 5.26. a part of the decorative pattern depicting the story of the Annunciation to Zachary. The *formella* is a casted brass gilded with the fire gilding technique described above. As in the previous samples, gilding was made with the fire gilding technique. For this sample, the analysis aimed at the characterization of the thickness of the gold alloy. Here, differently from the previous samples, where the information about the gold layer was known *a priori*, it was unknown. So, the analysis had to follow a different process, with a trial and error approach to find the result that fitted best the experimental data.

Figure 5.26: The annunciation to Zachary. An angel figure, on the left, is about to tell Zachary, on the right, about the birth of his child, John Baptist.

Data analysis

The *formella* was measured in 5 different areas:

- Altar (the central box between the two figures
- Zachary body
- Angel body and wing
- Lion cheek (from the frame, not shown in the figure)

For each area, a momentum scan was performed to obtain a depth profile of the elements present in the sample. The setup for this experiment consisted of four HPGe detectors placed at a distance from the sample that varied depending on the measured spot (that ranged from 10 to 15 cm). The momentum used ranged from 16 MeV/c to 24 MeV/c, with an average running time of 3 hours. As before, the data analysis consisted of peak identification and peak fitting to create depth profiles. After the identification, peaks were fitted with a Gaussian function. Again, the data analysis is coupled with the use of TRIM and GEANT4/ARBY Monte Carlo simulations. The sample was modelled in the software

with a similar layered structure and placed in front of a muon source at the same distance as the experimental setup. The results were then compared with the experimental one and the thickness of the gold layer was addressed.

Altar

The momentum scan from the altar shows a quite particular depth profile (Figure 5.27. Here, the data shows only a gradual transition from Au to Cu by the momentum change from 16 to 26 MeV/c. This means that the gold thickness is uneven as expected from the pattern: the presence of gold signal at 24 MeV/c, suggests that the size of the layer is in the range of the tens of microns. On the other end, the fact that the copper signal is present also at low momentum, suggests that the layer of gold, in some parts is thinner, allowing low-energy muons to travel through it. Considering that some gold signal is detected even at 24 MeV/c, the gold layer can extend to the tens of microns in some areas. This could be a consequence of the engraving work on the altar or a consequence of the gold deposition process.

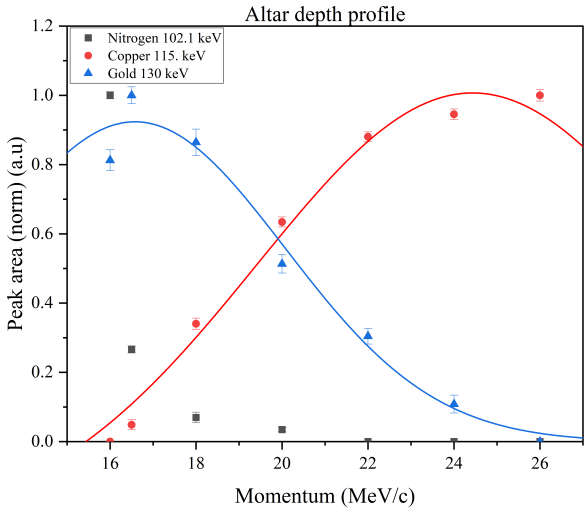

Figure 5.27: Depth profile of the altarpiece in between the two figures. Here, the gold signal is detected even in high momentum runs, meaning that in some areas gold is rather thick. On the other hand, the copper signal is detected at low momentum runs, meaning that in some areas the gold layer is quite thin.

Starting from these considerations, Monte Carlo simulations were performed (for all simulations, a momentum scaling of p = 1.03 was used). However, single-thickness simulations were not able to describe the behaviour of gold in the sample. As shown in Figure 5.28a, with a fixed thickness, the experimental gold profile is not well reproduced. For example, a 20 µm layer was too thin, while a 50 µm was too thick. A good compromise

seemed to be reached around 35 µm, but still with a poor agreement with the experimental measurements (simulations output in Figure 5.28 are from Geant4/ARBY, but the same outputs were given by TRIM). These results are a further confirmation of the unevenness of the layer. So, to deal with this issue, a sample with variable gold thickness was modelled in Geant4/ARBY. In this specific case, simulations with TRIM were not possible since the software was only able to simulate a fixed layer. In ARBY, instead, it is possible to have a layer composed of different thicknesses to replicate an uneven surface. Therefore, the gold layer was divided into 5 or 10 different stripes (of 1 or 0.5 cm, for a total length of 5cm) with variable sizes, from 1 up to 50 µm. In this way, the beam spot, which was uncollimated (40x40mm), could investigate an area that is not even and give a different output than a fixed layer. And the results are quite interesting. With this kind of approach, it was possible to replicate the gold profile with a better agreement than a single thickness, both with a 5 and 10 stripes simulation, as shown in Figure 5.28 (b). In the 5 stripes case (red), the thickness varied from 10 to 50 µm (with a 10 µm step) for an average of 30 µm, while for the 10 stripes case (blue), it varied from 1 to 50 µm for an average of 20 µm. In both situations, the experimental behaviour is well replicated, better than the fixed approach.

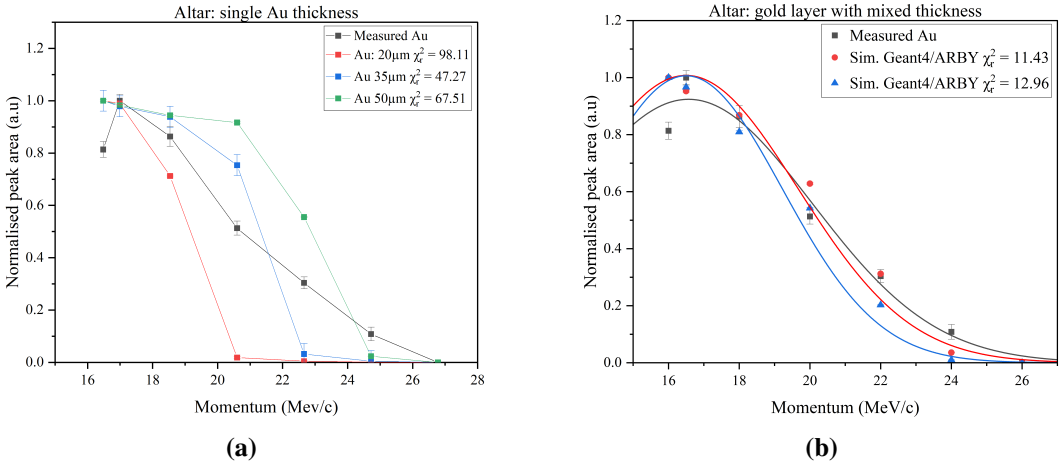

Figure 5.28: a) simulations with fixed thickness of the gold layer. The deviation with the experimental results is quite high, as stated by chi square calculations. With an uneven surface (b), the simulated results improve, with better agreement with the experimental data.

Zacharia

For Zacharia's figure, the momentum scan was performed with fewer points compared to the altar. As for the box and for all the measured areas, peak identification and peak fitting were performed. Differently from before, here the gold-copper transition is sharper and the gold signal quickly decreases to zero at 18 MeV/c. What is interesting about Zacharia's depth profile is the behaviour of oxygen. Here, at 17 MeV/c, there is an increase in the peak intensity: this means that at the gold-copper interface, there could be an oxidized layer,

meaning that the brass surface is corroded. And since the oxygen signal is present also at 20 MeV/c, this means that the oxidation is extended in the surface. 20 MeV/c in this case could be around 40 µm inside the sample).

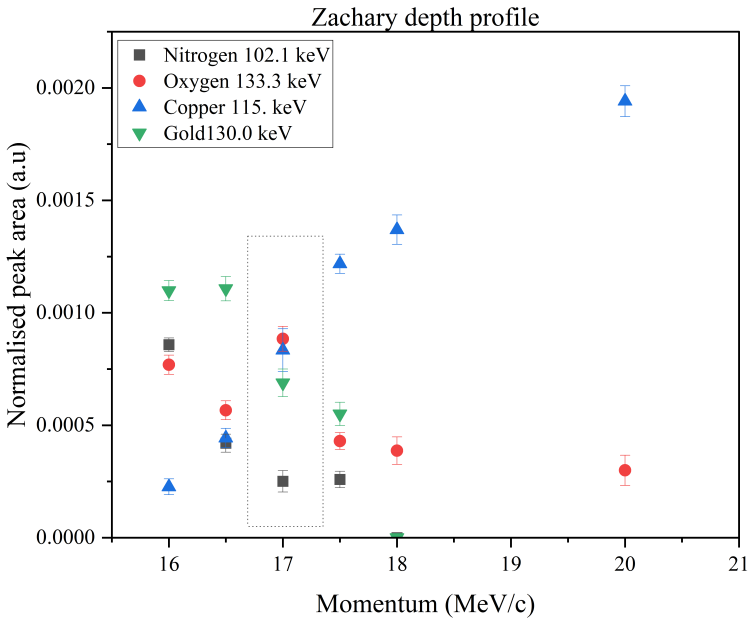

Figure 5.29: Depth profile of Zachary's body. The profile shows and increase of the oxygen signal at the gold/copper, and this signal is also detected at 20 MeV/c. This means that behind the gold surface, the copper layer is characterized by an extensive oxidation.

So, simulations were performed to assess the gold layer thickness and to try to evaluate the oxidation thickness as well. It has to be stated that for all the measured areas, the process involved simulations of a lot of different gold layer sizes, while here is reported only the best fit. For the Zacharia sample, the best fit was reached with a 15 µm gold layer, both with Geant4/ARBY and SRIM-TRIM. The issue about the oxidation layer is a bit more difficult instead. With SRIM-TRIM, layers under 180 nm are not detected and also since the output gives information about the entire layer and not a single component, it is difficult to replicate the experimental behaviour of oxygen (the same with ARBY).

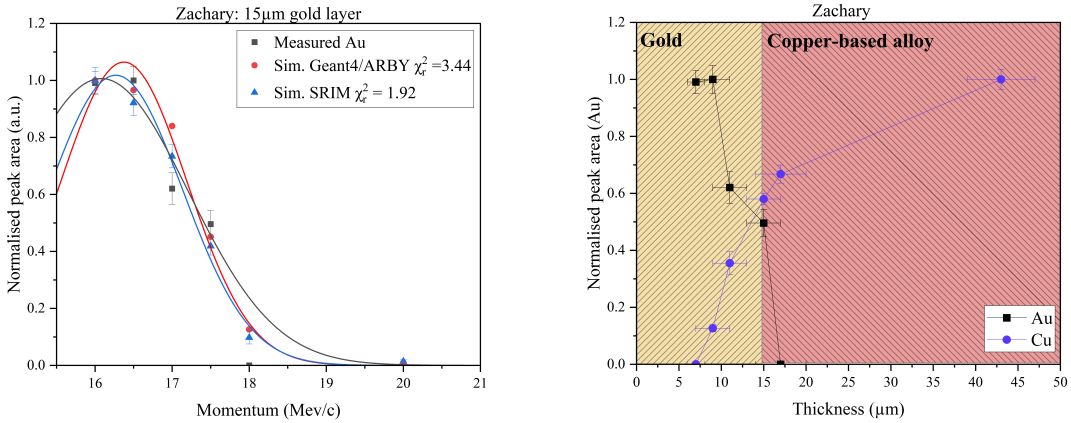

(a) **(b)**

Figure 5.30: a) Comparison between experimental and simulated data, with good results from both simulation software. b: here, depth profile is plotted as a function of thickness.

Angel Body and wing

As for Zacharia's figure, the angel body was scanned with 4 low momentum runs, from 16 to 19 MeV/c. Here, no particular effects are visible but the presence of oxygen at 19 MeV/c indicates that also in this case the copper surface is oxidised. Differently from before, this does not create a peak in the oxygen distribution. Zinc peaks were observed. For the angel wing, instead, no significant gold peak was detected. What is interesting here is that oxygen can be seen at 20 MeV/c and a little also at 40 MeV/c, indicating a very strong oxidation of the surface.

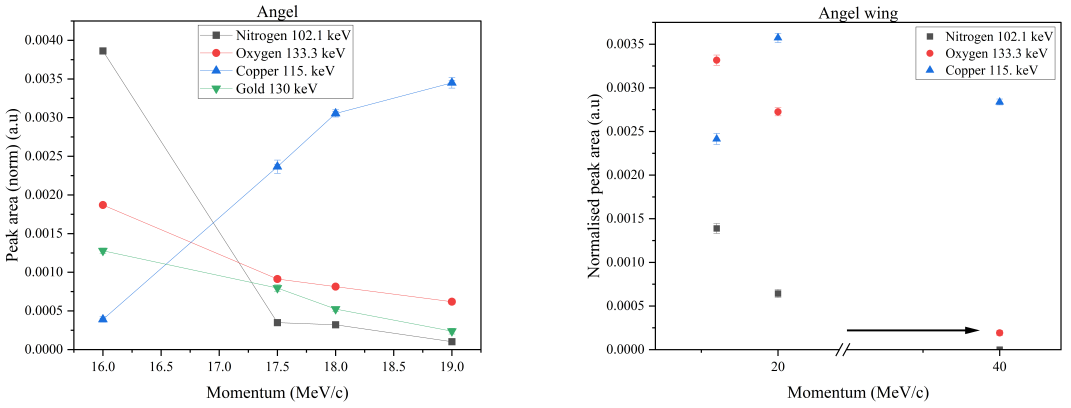

(a) **(b)**

Figure 5.31: a) angel body. As in the other samples, oxygen is detected at high momentum runs, testifying to the presence of oxidation. Oxidation that is more evident in the wing piece, where a low oxygen signal is detected even at 40 MeV/c.

Given that in the angel wing no gold was detected, simulations were performed only for the angel body. As for Zacharia, both SRIM-TRIM and Geant4/ARBY were used. Here, the best fit for the gold layer is obtained with a thickness of 16 µm, a result in agreement with the one obtained for Zacharias figure and in agreement between the two software.

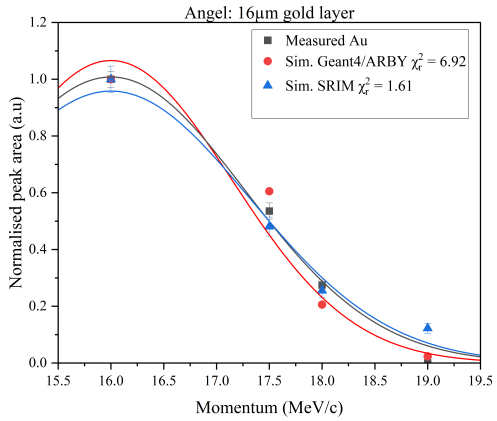

Figure 5.32: Results of the simulation: here, ARBY performed worse than TRIM. This could be to the fact that even if a fixed thickness provided a good results, the surface could be uneven.

Lion cheek

The lion is the only area outside the evangelical representation. However, the depth profile is quite similar to the angel body, with a small increase in the oxygen profile at 18 MeV/c. As before, this means an oxidation of the surface at the gold-brass interface. So, simulations were performed and the best fit was reached with a gold thickness of 15 µm. The result is consistent with Zacharia and Angel's body. As shown in 5.33 (a) there is a small increase at 18.5 MeV/c in the gold intensity that the simulations are not able to reproduce, that could be due to a small increase in thickness in some part of the investigated area.

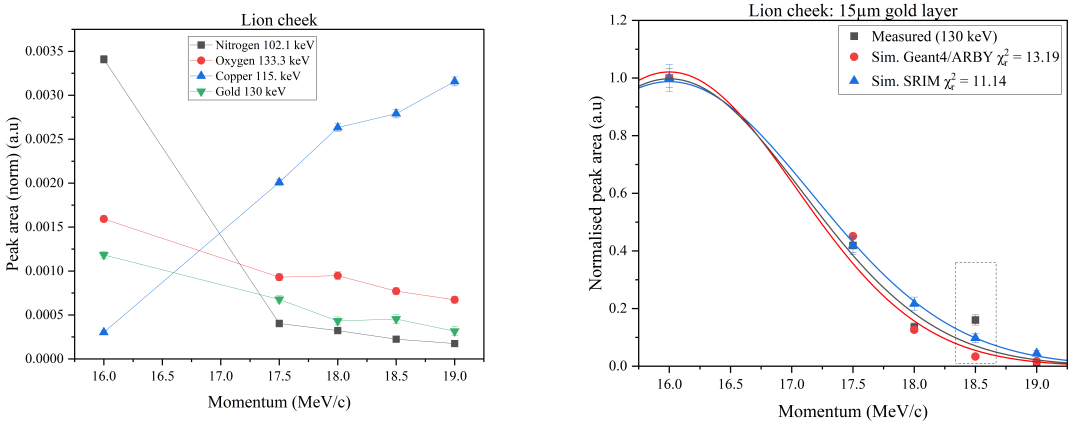

Figure 5.33: a depth profile of the Lion cheek. As the other sample, here oxydation is detected. The gold profile was fitted with a single-layer thickness, but the increase in gold signal at 18.5 MeV/c, suggests that the layer could be uneven.

In this work, two simulation software were used to replicate a negative muon experiment. With both software, good results were achieved, and it was possible to assess the thickness of gold layers. The analysis for three areas (Zacharias, Angel, Lion cheek) showed a similar depth dependence of Au/Cu ratio, while for the altar the gradual transition from Au-to-Cu, indicated an uneven gold thickness. Furthermore, all the investigated areas showed extensive oxidation of the surface, given that the oxygen component was extended deep inside the material. Finally, the Zn L and M peaks have a peak intensity that is 25% of the copper peak, indicating a Cu:Zn concentration of circa 0.75:0.25, consistent with the literature.

Table 5.3: Final results of the modelling of the *formella*

Measured area	Main identified elements	Gold thickness
Altar	N,O,Au,Cu,Zn	Uneven- from 1 to 50 µm
Zachary body	N,O,Au,Cu,Zn	15 ± 0.5 µm
Angel body	N,O,Au,Cu,Zn	16 ± 0.5 µm
Angel wing	N,O,Au,Cu,Zn	Not detected
Lion cheek	N,O,Au,Cu,Zn	15 ± 0.5 µm

Bibliography

[1] Massimo Chiari. "External Beam IBA Measurements for Cultural Heritage". In: *Applied Sciences* 13.5 (2023). DOI: 10.3390/app13053366.

[2] Caroline Bouvier et al. "Time-of-flight secondary ion mass spectrometry imaging in cultural heritage: A focus on old paintings". In: *Journal of Mass Spectrometry* 57.1 (2022), e4803. DOI: https://doi.org/10.1002/jms.4803.

[3] Walter Giurlani et al. "Thickness determination of metal multilayers by ED-XRF multivariate analysis using Monte Carlo simulated standards". In: *Analytica Chimica Acta* 1130 (2020), pp. 72–79. DOI: https://doi.org/10.1016/j.aca.2020.07.047.

[4] J A Helsen and B A R Vrebos. "Monte Carlo simulations of XRF intensities in non-homogeneous matrices". In: *Spectrochimica Acta Part B: Atomic Spectroscopy* 39 (6 1984), pp. 751–759. DOI: https://doi.org/10.1016/0584-8547(84)80083-X.

[5] Carlo E. Bottaini et al. "Use of Monte Carlo Simulation as a Tool for the Nondestructive Energy Dispersive X-ray Fluorescence (ED-XRF) Spectroscopy Analysis of Archaeological Copper-Based Artifacts from the Chalcolithic Site of Perdigões, Southern Portugal". In: *Applied Spectroscopy* 72 (1 2018), pp. 17–27. DOI: 10.1177/0003702817721934.

[6] Antonio Brunetti et al. "Use of Monte Carlo simulations for Cultural Heritage X-ray fluorescence analysis". In: *Spectrochimica Acta - Part B Atomic Spectroscopy* 108 (2015), pp. 15–20. DOI: 10.1016/j.sab.2015.03.014.

[7] James F. Ziegler, M. D. Ziegler, and J. P. Biersack. "SRIM – The stopping and range of ions in matter (2010)". In: *Nuclear Instruments and Methods in Physics Research Section B: Beam Interactions with Materials and Atoms* 268 (11-12 June 2010), pp. 1818–1823. DOI: 10.1016/J.NIMB.2010.02.091.

[8] A. D. Hillier, D. M. Paul, and K. Ishida. "Probing beneath the surface without a scratch - Bulk non-destructive elemental analysis using negative muons". In: *Microchemical Journal* 125 (2016), pp. 203–207. DOI: 10.1016/j.microc.2015.11.031.

[9] A. D. Hillier, K. Ishida, and B. Hampshire. *Depth-Dependent Bulk Elemental Analysis Using Negative Muons*. Ed. by Valentina D'Amico Sebastiano and Venuti. 2022. DOI: 10.1007/978-3-030-60016-7_3.

[10] C M Poole et al. "A CAD interface for GEANT4". In: *Australasian Physical Engineering Sciences in Medicine* 35 (3 2012), pp. 329–334. DOI: 10.1007/s13246-012-0159-8.

[11] Plinio il Vecchio. *Naturalis Historia, 33*.

[12] Kilian Anheuser. "The practice and characterization of historic fire gilding techniques". In: *JOM* 49 (11 1997), pp. 58–62. DOI: 10.1007/s11837-997-0015-6.

[13] Andrew Oddy. "Gilding through the ages". In: *Gold Bulletin* 14 (2 1981), pp. 75–79. DOI: 10.1007/BF03214601.

[14] B. Cellini. *The treatises of Benvenuto Cellini on goldsmithing and sculpture, Chapter XXVI*. 1568.

[15] Alessandra Giumlia-Mair. "Plating and Surface Treatments on Ancient Metalwork". In: *Advances in Archaeomaterials* 1 (1 Dec. 2020), pp. 1–26. DOI: 10.1016/j.aia.2020.10.001.

[16] Walter Giurlani et al. *Electroplating for decorative applications: Recent trends in research and development*. Aug. 2018. DOI: 10.3390/coatings8080260.

[17] *Origin(Pro), Version 2022*.

[18] R. Engfer et al. "Charge-distribution parameters, isotope shifts, isomer shifts, and magnetic hyperfine constanst from muonic atoms". In: *Atomic Data and Nuclear Data Tables* 14 (1974), pp. 509–597.

[19] D. R. Zinatulina. "Electronic Catalogue of Mesoroentgen Spectra". In: *Physics of Atomic Nuclei* 82 (3 2019). DOI: 10.1134/S1063778819030165.

[20] Simone Sturniolo and Adrian Hillier. "Mudirac: A Dirac equation solver for elemental analysis with muonic X-rays". In: *X-Ray Spectrometry* (June 2020), pp. 1–17. ISSN: 10974539. DOI: 10.1002/xrs.3212.

[21] O. Arnold et al. "Mantid—Data analysis and visualization package for neutron scattering and μ SR experiments". In: *Nuclear Instruments and Methods in Physics Research Section A: Accelerators, Spectrometers, Detectors and Associated Equipment* 764 (2014), pp. 156 –166. DOI: https://doi.org/10.1016/j.nima.2014.07.029.

Conclusions

Muonic Atom X-ray Spectroscopy is a unique method in the field of Heritage Science. Coupled with other methods like Neutron-base techniques, it can give new and different insights to the study of historical artefacts. At ISIS, the increased request in beam time from users, requires the technique to be improved. In this work, three major topics for improvement have been discussed. A new detector setup was characterized by means of Monte Carlo simulations and talks were started with the manufacturing company. Discussion led to a final choice between two different configurations: a segmented crystal and a telescope detector. Both setups have their own advantages in terms of resolving power and detection efficiencies. Implementing a Euroball-like detector array will provide a significant improvement to the technique, making Port4 a one-of-a-kind setup for elemental analysis with negative muons. In the immediate future, the setup of Port4 will be updated with the acquisition of germanium detectors. The cluster, instead, represents the ultimate setup, that could be implemented in the framework of a new instrument. From our side, the work towards the implementation of this solution will continue as part of the CHNetMAXI project.
The GEANT4/Arby simulation software was discussed in Chapter 4. The software has been used for simulating a negative muon experiment: the study of the simulation outputs revealed a discrepancy between the literature and the simulated emission, which was investigated for different versions of the software. An improvement was provided by using MuDirac and by implementing it in GEANT4/ARBY. The preliminary results reported in the work show the goodness of the approach, but to make this available in the actual GEANT4 software, more work is expected. The MuDirac output is not yet fully comparable to the real experiment due to issues in the calculation of the intensities of the emitted peaks. An improvement is expected with new versions of the software. From our side, a different approach will be investigated in the future: instead of using the information coming from the simulated spectra, the data to be fed to the software will be the transition and their branching ratios (or transition probabilities). In this way, problems in intensities could be avoided. Finally, two simulation software were used to improve the data analysis and the data interpretation of negative muon experiments. SRIM-TRIM and GEANT4/Arby were used to assess the thickness of gold layers in gilded samples. The work served both as a source of comparison/validation of both software and as a tool for the characterization of ancient artefacts. In particular, the gold layer of the *formella* of the Florence Baptistery

gates and of mockup samples were characterised, with results in agreement with literature and previous analysis. These results have contributed to the characterization of an unknown layer of gold: to make this approach a well-established method for the characterization of thin layers, more materials and standards have to be analysed. In the future, the approach will be applied to the characterization of enamels, a unique type of artefact in the field of Heritage Science.

Appendix A

Capture cascade class

```
 GEANT4 Class file
 File name: G4EmCaptureCascade
 Author: V.Ivanchenko (Vladimir.Ivantchenko@cern.ch)
 Creation date: 22 April 2012 on base of G4MuMinusCaptureCascade

[...]
 55 G4EmCaptureCascade::G4EmCaptureCascade()
 56   : G4HadronicInteraction("emCaptureCascade")
 57 {
 58   theElectron = G4Electron::Electron();
 59   theGamma = G4Gamma::Gamma();
 60   fMuMass = G4MuonMinus::MuonMinus()->GetPDGMass();
 61   fTime = 0.0;
 62
 63   // Calculate the Energy of K Mesoatom Level for this Element
 64   // using the Energy of Hydrogen Atom taken into account
 65   // finite size of the nucleus
 66   static const G4int nlevels = 28;
 67   static const G4int listK[nlevels] = {
 68       1, 2,  4,  6,  8, 11, 14, 17, 18, 21, 24,
 69      26, 29, 32, 38, 40, 41, 44, 49, 53, 55,
 70      60, 65, 70, 75, 81, 85, 92};
 71   static const G4double listKEnergy[nlevels] = {
 72      0.00275, 0.011, 0.043, 0.098, 0.173, 0.326,
 73      0.524, 0.765, 0.853, 1.146, 1.472,
 74      1.708, 2.081, 2.475, 3.323, 3.627,
 75      3.779, 4.237, 5.016, 5.647, 5.966,
 76      6.793, 7.602, 8.421, 9.249, 10.222,
 77     10.923,11.984};
```

```
 78
 79   fKLevelEnergy[0] = 0.0;
 80   fKLevelEnergy[1] = listKEnergy[0];
 81   G4int idx = 1;
 82   for(G4int i=1; i<nlevels; ++i) {
 83     G4int z1 = listK[idx];
 84     G4int z2 = listK[i];
 85     if(z1+1 < z2) {
 86       G4double dz = G4double(z2 - z1);
 87       G4double y1 = listKEnergy[idx]/G4double(z1*z1);
 88       G4double y2 = listKEnergy[i]/G4double(z2*z2);
 89       for(G4int z=z1+1; z<z2; ++z) {
 90         fKLevelEnergy[z] = (y1 + (y2 - y1)*(z - z1)/dz)*z*z;
 91       }
 92     }
 93     fKLevelEnergy[z2] = listKEnergy[i];
 94     idx = i;
 95   }
 96   for(G4int i = 0; i<14; ++i) { fLevelEnergy[i] = 0.0; }
 97 }
 98
 99 //
100
101 G4EmCaptureCascade::~G4EmCaptureCascade()
102 {}
103
104 //
105
106 G4HadFinalState*
107 G4EmCaptureCascade::ApplyYourself(const G4HadProjectile& projectile,
108           G4Nucleus& targetNucleus)
109 {
110   result.Clear();
111   result.SetStatusChange(isAlive);
112   fTime = projectile.GetGlobalTime();
113
114   G4int Z = targetNucleus.GetZ_asInt();
115   G4int A = targetNucleus.GetA_asInt();
116   G4double massA = G4NucleiProperties::GetNuclearMass(A, Z);
117   G4double mass = fMuMass * massA / (fMuMass + massA) ;
118   G4double e = 13.6 * eV * (Z * Z) * mass/ electron_mass_c2;
```

```
119
120   // precise corrections of energy only for K-shell
121   fLevelEnergy[0] = fKLevelEnergy[std::min(Z, 92)];
122   for(G4int i=1; i<14; ++i) {
123     fLevelEnergy[i] = e/(G4double)((i+1)*(i+1));
124   }
125
126   G4int nElec  = Z;
127   G4int nAuger = 1;
128   G4int nLevel = 13;
129   G4double pGamma = (Z*Z*Z*Z);
130
131   // Capture on 14-th level
132   G4double edep = fLevelEnergy[13];
133   AddNewParticle(theElectron,edep);
134   G4double deltaE;
135
136   // Emit new photon or electron
137   // Simplified model for probabilities
138   // N.C.Mukhopadhyay Phy. Rep. 30 (1977) 1.
139   do {
140
141     // case of Auger electrons
142     if((nAuger < nElec) && ((pGamma + 10000.0) *
          G4UniformRand() < 10000.0) ) {
143       ++nAuger;
144       deltaE =  fLevelEnergy[nLevel-1] -  fLevelEnergy[nLevel];
145       --nLevel;
146       AddNewParticle(theElectron, deltaE);
147
148     } else {
149
150       // Case of photon cascade, probabilities from
151       // C.S.Wu and L.Wilets, Ann. Rev. Nuclear Sci. 19 (1969) 527.
152
153       G4double var = (10.0 + G4double(nLevel - 1) ) * G4UniformRand();
154       G4int iLevel = nLevel - 1 ;
155       if(var > 10.0) iLevel -= G4int(var-10.0) + 1;
156       if( iLevel < 0 ) iLevel = 0;
157       deltaE =  fLevelEnergy[iLevel] -  fLevelEnergy[nLevel];
158       nLevel = iLevel;
```

```
159       AddNewParticle(theGamma, deltaE);
160     }
161     edep += deltaE;
162
163     // Loop checking, 06-Aug-2015, Vladimir Ivanchenko
164   } while( nLevel > 0 );
165
166   result.SetLocalEnergyDeposit(edep);
167   return &result;
168 }
169
170 //
171
172 void G4EmCaptureCascade::ModelDescription(std::ostream& outFile) const
173 {
174  outFile << "Simulation of electromagnetic cascade from capture level"
175   << " to K-shell of the mesonic atom\n."
176   << "Probabilities of gamma and Auger transitions from\n"
177   << "  N.C.Mukhopadhyay Phys. Rep. 30 (1977) 1.\n";
```

Scientific activities

Neutron and Muon experiments

- *Development of negative muon data analysis through measurements of standard samples*. Set of Measurement of different kinds of standard: gilded brass and copper alloys.
  Data availability: https://doi.org/10.5286/ISIS.E.RB2300032

- *Use of negative muons as elemental depth scanning analytical method for metal composite materials: an application to archaeometallurgy*. Set of measurements on composite metal artefacts in order to test the capability of the negative muons elemental analysis method to identify the alloy guest elements and perform depth profiling. Performed at the ISIS Neutron and Muon Source, UK.
  Data availability: https://doi.org/10.5286/ISIS.E.RB1910123.

- *Use of Negative Muons for depth profiles characterization of metallic Roman finds*. Set of measurements on the gilded bronzes from Cartoceto di Pergola. Performed at the ISIS Neutron and Muon Source, UK.
  Data availability: https://doi.org/10.5286/ISIS.E.RB2000263

- *Technological study of Nuragic Bronze boat models* Set of measurements on Nuragic artefacts. Performed at the ISIS Neutron and Muon Source, UK.
  Data availability: https://doi.org/10.5286/ISIS.E.RB1820404

Published papers

[1] Anna Depalmas et al. "Neutron-based techniques for archaeometry: characterization of a Sardinian boat model". In: *Archaeological and Anthropological Sciences* 13 (6 2021). DOI: 10.1007/s12520-021-01345-w.

[2] **M. Cataldo** et al. "A Novel Non-Destructive Technique for Cultural Heritage: Depth Profiling and Elemental Analysis Underneath the Surface with Negative Muons". In: *Applied Sciences* 12.9 (2022). DOI: 10.3390/app12094237.

[3] Riccardo Rossini et al. "A new multidisciplinary non-destructive protocol for the analysis of stony meteorites: gamma spectroscopy, neutron and muon techniques supported by Raman microscopy and SEM-EDS". In: *J. Anal. At. Spectrom.* 38 (2 2023), pp. 293–302. DOI: 10.1039/D2JA00263A. URL: http://dx.doi.org/10.1039/D2JA00263A.

[4] **M. Cataldo** et al. "The Implementation of MuDirac in Geant4: A Preliminary Approach to the Improvement of the Simulation of the Muonic Atom Cascade Process". In: *Condensed Matter* 8.4 (2023). ISSN: 2410-3896. DOI: 10.3390/condmat8040101. URL: https://www.mdpi.com/2410-3896/8/4/101.

Conference papers

[1] **M. Cataldo** et al. "Joint negative muon data analysis and Monte Carlo simulation methods for the characterization of thin layers". In: *Il Nuovo Cimento C* 46 (2023). DOI: 10.1393/ncc/i2023-23151-5.

[2] **M. Cataldo** et al. "Non-invasive characterization of Nuragic bronzes through neutron based techniques". In: *2020 IMEKO TC-4 International Conference on Metrology for Archaeology and Cultural Heritage* (2020), pp. 399–403. URL: https://www.imeko.org/publications/tc4-Archaeo-2020/IMEKO-TC4-MetroArchaeo2020-074.pdf.

[3] **M. Cataldo** et al. "Negative muons for the characterization of thin layers in Cultural Heritage artefacts". In: *Journal of Physics: Conference Series* (2023). DOI: 10.1088/1742-6596/2462/1/012003.

Conferences - Oral communications

- **Research in progress meeting** [15 Nov 2019], Historical Metallurgy Society, Mcdonald Institute, Cambridge University, UK. *Title: Non-invasive characterization of nuragic bronzes through neutron diffraction* Cataldo M., Scherillo A., Grazzi F., Brunetti R.

- **Metrology and Archeology for Cultural Heritage**[22-24 Oct 2020], IMEKO TC-4 International conference, Virtual event; *Title: Non-invasive characterization of Nuragic bronzes through neutron based techniques* Cataldo M., Scherillo A., Fedrigo A., Depalmas A., Canu A., Grazzi F., Brunetti R.

- **Joint IAEA–ANSTO Workshop on Nuclear and Isotopic Techniques for Cultural Heritage** [6-9 Dec 2021], Australian Nuclear Science and Technology Organisation

(ANSTO), Lucas Heights NSW Australia, Virtual event. *Title: Muons to the rescue: application of Muonic X ray emission spectroscopy (μXES) for non destructive measurements*, Cataldo M., Clemenza M., Hillier A.D., Ishida K.,Agoro T.

- **IAEA Workshop on Innovative Approaches of Accelerator Science and Technology for Sustainable Heritage Management** [13-16 Jun 2022], IAEA Headquarters, Vienna, Austria. *Title: Thin layers characterization with negative muons: a case study of gilded bronzes* Cataldo M., A. D Hillier A.D., Ishida K., Grazzi F., S.Porcinai S., Clemenza M.

- **The 15th International Conference on Muon Spin Rotation, Relaxation and Resonance** [28 Aug-2 Sep 2022], Science Campus, Parma, Italy. *Title: Negative muons for the characterization of thin layers in Cultural Heritage artefacts* Cataldo M., Hillier A.D., Ishida K., Grazzi F., Porcinai S., Cremonesi O., Clemenza M.

- **108° Congresso Nazionale Società di Fisica Italiana** [12-16 Sep 2022], Milano, Italy.

  Title: Characterization of thin layers with negative muons, Cataldo M., Hillier A.D., Ishida K., Grazzi F., Porcinai S., Cremonesi O., Clemenza M.

- **Workshop on elemental analysis with negative muons** [30 Mar 2023], Virtual event.

  Title: Characterization of gilded sufaces with negative muons, Cataldo M., Hillier A.D., Ishida K., Grazzi F., Porcinai S., Cremonesi O., Clemenza M.

- **NMSUM 2023 - UK Neutron and Muon science user meeting** [19-21 Apr 2023], Warwick University, UK.

  Title: Negative muons for Cutural Heritage science, Cataldo M.

- **TECHNART 2023 International conference on analytical techniques in art and cultural heritage** [7-12 May 2023], Lisbon, Portugal.

  Title: Using negative muons for the characterization of thin layers in Cultural Heritage science, Cataldo M., Hillier A.D., Ishida K., Grazzi F., Porcinai S., Cremonesi O., Clemenza M.

- **HPMX 2023 - High Precision X-ray Measurement conference** [19 -23 Jun 2023], Frascati National Laboratories, Italy.

  Title: Muonic X-rays for cultural heritage: technique overview and developments, Cataldo M., Hillier A.D., Pozzi S., Cremonesi O., Clemenza M.

Schools

- Training course on risk from ionizing radiation and radiation protection, INFN Milano Bicocca Section [13 Mar 2021]
- **J-PARC Neutron and Muon School** [6-9 Dec 2021]. The School provides lectures and practical training for newcomers to neutron and muon beam research from across the fields of physics, chemistry, biology, materials science and more. The lectures cover most of the basic neutron and muon methodologies applied to material research.
- **MuSR2020 Science Day** Virtual event [13-14 Dec 2021].
- **First steps with Geant4** Virtual course [9-13 May 2022]. Organised by CERN Technical Training and the EP Department, SFT Group. The course provides tutorials on Geant4 for users interested to begin or improve their usage of Geant4. Appropriate for creating applications in any domain, with emphasis on topics most relevant to experiments in High Energy or Nuclear Physics.
- **INFN School of Statistics** Paestum (SA), Italy [15-20 May 2022]. The INFN School of Statistics intends to provide an overview of statistical methods and tools used in particle, astroparticle and nuclear physics.
- **XIX INFN Seminar on Software for Nuclear, Subnuclear, and Applied Physics** Alghero (SS), Italy [6-10 Jun 2022]. This event is organized by INFN, University of Sassari and by the SNAKE (Sharing Software Knowledge) non-profit organisation. The lectures also include a full official basic course on the Geant4 Monte Carlo simulation toolkit.
- **VIU PhD Academy Preserving and Safeguarding the Beauty of Cultural Heritage** Venezia (SS), Italy [6-10 Nov 2023]. Fundamentals, Methods and Applications of State-of-the-Art Diagnostic Tools Using Optical, X-Ray and Particle Probes, organized by the Venice International University.